ADVANCED PLASMA NITRIDING OF REACTOR CLADDING MATERIALS

A Dissertation

by

ROBERT BENJAMIN BALERIO

Submitted to the Graduate and Professional School of
Texas A&M University
in partial fulfillment of the requirements for the degree of

DOCTOR OF PHILOSOPHY

Chair of Committee,	Lin Shao
Co-Chair of Committee,	Sean M. McDeavitt
Committee Members,	Craig Marianno
	Karl T. Hartwig
Head of Department,	Michael Nastasi

December 2022

Major Subject: Nuclear Engineering

ABSTRACT

In the commercial nuclear power industry, there is a vested interest in improving the properties of the reactor components. Improving nuclear reactor materials to resist the severe structural changes and degradation not only improves reactor safety and reliability, but also economical returns from decreased outages and upkeep cost. As the first barrier of fission product containment, the performance of fuel cladding in a nuclear reactor is a pivotal design parameter in ensuring reactor safety and reliability. An attractive solution to improve fuel cladding performance by enhancing the surface cladding properties while not affecting the bulk matrix material properties can be achieved through surface engineering techniques. Although surface modification techniques have been shown to improve cladding oxidation and corrosion resistance, debonding of the modified surface from the bulk matrix makes such approaches unsuitable for reactor applications.

In this dissertation, effects of advanced cathodic cage plasma nitriding on reactor cladding materials T91, HT-9, 316L, and Zircaloy-4 was investigated. The microstructual, corrosion and mechanical surface properties were evaluated as well as ion irradiation resistance and nitrogen diffusion kinetics of the nitrogen modified layer. Nitriding improved the mechanical surface properties of all investigated materials with steels and Zircaloy-4 hardness increasing to 14-16 GPa and 20-24 GPa respectively. The corrosion resistance in 3.5 wt% NaCl varied for all nitrided materials dependent on nitriding temperature and time. The corrosion rate of nitride 316L had the least improvement where the reference sample measurement was 1.9 µm/yr and nitrided sample at 454 °C for 45 minutes was 1.2 µm/yr. At higher temperatures and longer nitriding durations, the corrosion resistance was reduced.

Nitriding of T91 and HT-9 significantly enhanced corrosion resistance for nitriding temperatures below 570 °C. The corrosion rate of nitrided Zircaloy-4 decreased by an order of magnitude for all samples above 920 °C.

The effective nitrogen diffusion coefficient, D_0 and activation energy, Q of 316L is 23.01±6.55 cm2/sec and -1.65±0.02 eV/atom, respectively. The calculated D_0 and Q for nitrogen in T91 are 9.91E-4 ± 1.97E-4 cm^2/sec and -0.82 ±0.02 eV/atom respectively. The calculated D_0 and Q for nitrogen in HT9 are 5.16 ± 3.52 cm^2/sec and -1.46 ± 0.04 eV/atom respectively. At temperatures above 863 °C, the calculated D_0 and Q were 706 ± 693 cm^2/sec and -3.00 ± 0.09 eV/atom respectively. The calculated D_0 and Q for temperatures below 863 °C were 3.35E-2 ± 0.6E-2 cm^2/sec and -2.02 ± 0.02 eV/atom respectively.

CONTRIBUTORS AND FUNDING SOURCES

Contributors

This work was supported by a dissertation committee consisting of Professors Lin Shao, Sean M. McDeavitt and Craig Marianno of the Department of Nuclear Engineering and Professor Karl T. Hartwig of the Department of Materials Science & Engineering.

Surface topography and Raman analysis of zirconium alloys depicted in Chapter 5 conducted in part under leadership of Professor Don A. Lucca from Oklahoma State University. Corrosion testing in molten salt depicted in Chapter 4 was conducted under the leadership of Michael P. Short from Massachusetts Institute of Technology.

The FIB preparation and TEM analysis for Chapter 8 were conducted by Dr. Hyosim Kim from the Department of Nuclear Engineering. The analysis and experimental work depicted in Chapter 9 were conducted in part by Dr. Andres Morell-Pacheco of the Department of Nuclear Engineering and were published in (2020) in an article listed in the Journal of Nuclear Materials. The analysis and experimental work depicted in Chapter 10 were conducted in part by Andres Morell-Pacheco of the Department of Nuclear Engineering.

All other work conducted for the dissertation was completed by the student independently.

Funding Sources

This graduate study was supported by US Department of Energy through grant no. DE-NE0008450.

TABLE OF CONTENTS

Page

LIST OF FIGURES

LIST OF TABLES

TABLE Page

1. INTRODUCTION

In harsh environments of nuclear reactors materials experience severe structural changes and degradation which affects not only lifespan but also reactor safety and reliability. Development of advanced materials and fabrication techniques are critical for both present designs with extended life times and advanced designs with even harsher operation conditions. As the first barrier for containment of fission products, nuclear fuel cladding performance is a pivotal parameter in the design of nuclear reactors to ensure reactor safety and reliability. While there are many manners in which fuel cladding can degrade in the harsh reactor environment, such as swelling, embrittlement and creep, the majority of cladding failures are due to surface interactions [67]. Surface engineering techniques are an attractive solution to improve fuel cladding performance by enhancing the surface properties while not affecting the bulk matrix material properties.

1.1 Focus and Relevance

Although surface deposition coating techniques have been shown to improve oxidation and corrosion resistance of fuel cladding materials, challenges with debonding of the deposition layer from the original cladding matrix under exposure to coolants makes such approaches unsuitable for reactor applications. A solution to achieve improved surface properties without the drawback of debonding could be to modify the existing fuel cladding surface. Surface modification using cathodic cage plasma nitriding has the capability of altering the surface of material while having little to no effect on the bulk material. Numerous studies have shown that surface nitriding can be used to increase hardness, wear resistance, oxidation resistance, and corrosion resistance though there has not been a systematic investigation pertaining to nitrid-

ing effects on reactor fuel cladding materials, particularly when neutron damage and fuel cladding interactions must be considered.

Plasma nitriding of 316L was included in this study not only due to interest as nuclear cladding but also to evaluate the functionality of the advanced cathodic cage plasma nitriding device as nitriding of 316 stainless steel has been research using many techniques. In contrast to numerous studies of nitriding 316, to the author's knowledge plasma nitriding of Zircaloy-4, HT-9 and T91 has not been reported. This research has relevance as it addresses a gap in literature of plasma nitriding on reactor materials of interest. In conjunction with evaluating the effects of plasma nitriding, inaugural standardized potentiodymanic polarization corrosion measurements in 3.5 wt.% NaCl of unnitrided Zircaloy-4, HT-9 and T91 have been performed.

1.2 Objectives

The objective of this dissertation is to investigate the effects of advanced cathodic cage plasma nitriding on reactor cladding materials, with a primary focus on T91, HT-9, 316L, and Zircaloy-4. The surface properties that have been analyzed consists of microstructual and mechanical properties as well as corrosion and ion irradiation resistance. For outer cladding surfaces interacting with coolant, samples have been corrosion tested in NaCl and liquid molten salt to evaluate their corrosion resistance and compatibility with fast reactor applications. For inner cladding surfaces interacting with fuel, solid-to-solid diffusion couple experiment was conducted to study interface reactions of nitrided samples with uranium, to test whether a nitrided layer can improve resistance of fuel-cladding interactions.

2. BACKGROUND

In this chapter, background information relevant to the experiments performed will be covered. First nuclear materials issues will be reviewed, followed by an overview of nitriding methods. As mechanical and corrosion testing was used in this record of study, a basic indentation background is provided along with an introduction to potentiodynamic polarization measurements. The background chapter will then introduce the relative literature related to stainless steel 316, HT-9, T91 and Zircaloy-4.

2.1 Nuclear Materials Issues

Nuclear energy systems materials must not only meet the standard material design criteria based on tensile properties, thermal creep, cyclic fatigue and creep-fatigue but also must provide adequate resistance to the radiation damage degradation mechanisms in a corrosive nuclear environment [68]. Of the many radiation degradation effects, irradiation embrittlement, segregation, creep, void swelling, and high-temperature helium embrittlement are five key mechanisms of bulk radiation degradation. While fuel cladding is affected by bulk radiation degradation, failure mechanisms of fuel rods are mostly attributed to surface interactions, such as wear, pellet-cladding interactions, and corrosion [67].

Wear of the fuel rod cladding is the removal of cladding material in an abrasive manner and can lead to failure of the fuel rod. Grid-to-Rod Fretting (GTRF) is a flow-induced vibration problem that results in wear and failure of the rods [69]. As one of the leading causes for nuclear fuel leakage, GTRF wear has cost power utilities millions in preventive measures. Another wear mechanism is debris fretting which became a major cause of fuel failures in the 1980s and into the 1990s [70]. Debris such

as metal particles and chips in the coolant lodge between the walls of the grid cells and the fuel rods results in abrasive removal of cladding surfaces. This fuel failure mechanism has become less prevalent due to fuel assembly being fitted with debris filters in the bottom nozzle and improved foreign material exclusion procedures.

Pellet-induced cladding failures that occur during power transients are classified as pellet-cladding interactions (PCI) and pellet-cladding mechanical interactions (PCMI) [71]. PCMI is the result of the thermal expansion and fission gas-induced swelling of the fuel pellet producing strain on the interior of the fuel cladding exceeding its yield strength. PCMI cracks can be initiated internally or externally the tube and can contribute to local hydride weakening of the cladding. For PCI, stress corrosion cracking (SCC) is initiated on the internal surface of cladding due to chemical interactions with the fuel pellet under sustained strain from PCMI and differs from conventional SCC in that the cladding strain is below its yield strength [71]. Figure 2.1 illustrates how the cylindrical fuel pellet deforms and interacts with the cladding [1].

Corrosion can be defined as a chemical or electrochemical interaction of a material with its environment resulting in the material's destruction or deterioration. Corrosion is classified into five general types which are galvanic, stress cracking, general localized, and caustic agent corrosion. These destructive processes contribute largely to the growing operation and maintenance cost of nuclear power plants, exceeding 8.4 billion USD for LWRs by 1998 [72]. Nuclear energy systems must also take into account irradiation assisted corrosion (IAC) mechanisms, such as irradiation-assisted stress corrosion cracking (IASCC).

IASCC has been observed since the early 1960's and mainly affects stainless steel fuel cladding, instrument tubes, and control rod followers [73]. IASCC is a form of SCC enhanced by radiation environments via mechanisms of radiation induced grain

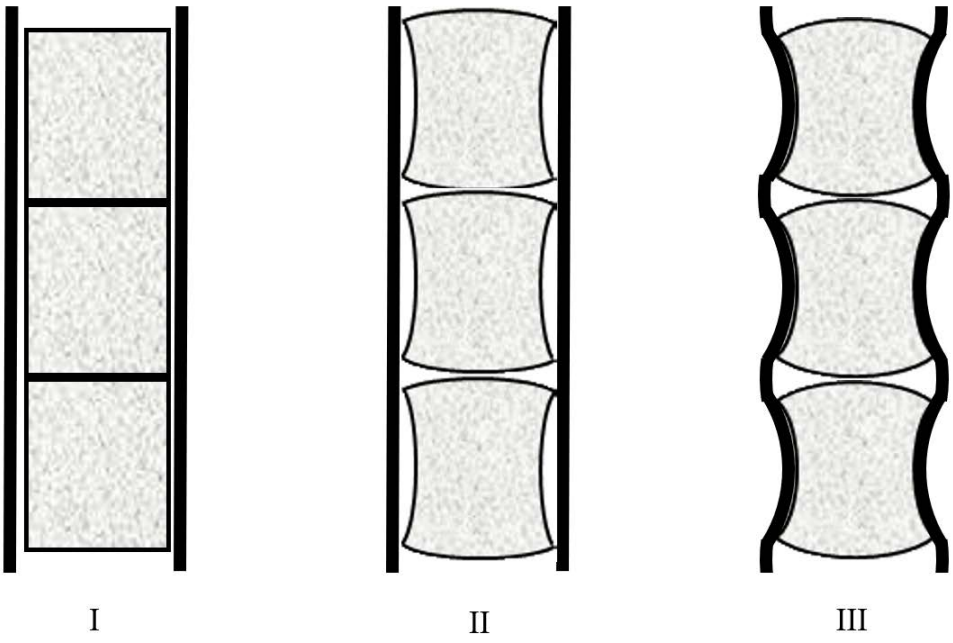

Figure 2.1: Interaction between fuel pellets and cladding: as fabricated (I), PCI (II), PCMI (III). Adapted from [1].

boundary chromium depletion, radiation hardening, localized deformation, selective internal oxidation, and irradiation creep [74]. It has a threshold-like behavior correlated to displacements per atom (dpa) and only occurs with the combination of an aggressive environment and irradiation.

Fuel cladding must not only meet the corrosion requirements of normal operating conditions, but must also meed design requirements for abnormal operating conditions [75]. The most commonly used cladding material in the nuclear power industry today is zirconium alloys primarily due to its low neutron absorption cross section, good fabricability, and high strength [68]. The advantages Zr fuel cladding are countered by its anisotropic properties of the HCP crystal structure and poor oxidation response in steam at high temperatures. While Zr cladding exhibits high corrosion resistance under normal operating conditions, accident response of hydro-

gen production and rapid oxidation is a well known disadvantage, as demonstrated in the Three Mile Island and Fukushima Daiichi nuclear accidents.

2.2 Nitriding Methods

Nitriding is process that alloys nitrogen into the surface of a metal to harden the surface of the metal [2]. Nitriding works by creating nascent nitrogen which is capable of diffusing into the surface of the material. This forms a nitride layer on the surface that has distinct properties from the bulk. Nitriding has been shown to increase wear resistance, corrosion resistance and hardness. The three main methods used for nitriding are gas, salt bath, and plasma nitriding.

2.2.1 Gas Nitriding

Gas nitriding uses gaseous ammonia (NH_3) as a nitrogen source. When heated to a high enough temperature, the ammonia decomposes producing hydrogen and nascent nitrogen in significant quantities. These nitrogen ions are then able to diffuse into the surface of the material exposed to the high temperature ammonia. Because the amount of free nitrogen produced is a temperature driven process, gas nitriding is performed at relatively high temperatures of 500 °C to 560 °C. While gas nitriding is a more popular nitriding method due ease and relatively low cost, the disadvantages of surface oil contamination control requirements and longer nitriding times limit the use of this technique.

2.2.2 Salt Bath Nitriding

Salt bath nitriding process uses cyanide or cyanate salts and produces nascent using the high chemical potential of the salts. Normal nitriding temperatures for salt bath nitriding range from 565 °C to 585 °C, but can be performed at much lower temperatures by increasing the nitriding time [2]. The process was created as an al-

ternative to gas nitriding because it could produce a more uniform nitride case. Due to the toxicity of the salts used, the salt bath process is now restricted in many countries due to environmental issues associated with the waste streams produced. These controls of the toxic chemicals makes salt bath a relatively costly nitriding process even though it requires less time to produce the same nitride thickness compared to gas nitriding.

2.2.3 Plasma Nitriding

Plasma nitriding is the process of using ionized nitrogen gas to accelerate nitrogen ions into the surface of a target [2]. This process is also called ion nitriding, glow discharge nitriding, and plasma ion nitriding. Plasma nitriding techniques were first implemented in 1932 as a metallurgical processing tool by a German physicist, Dr. Wehnheldt. Due to the instability of the glow discharge causing arcs, he was initially unable to control it as a nitriding process. Later Dr. Wehnheldt collaborated with Swiss physicist, Dr. Bernhard Berghaus, and the two of them developed a controllable plasma nitriding technique. The plasma nitridation technique eventually arrived in the United States during the 1950's, where General Electric successfully investigated the glow discharge method of nitriding. During the mid-1970's, pulsed dc current technology was developed at the University of Aachen in Germany to better control the glow discharge. This greatly improved the control of the nitriding procedure [2]. Due to the plasma being used to create nascent nitrogen for surface diffusion, the process can be performed at low temperatures and does not require a quenching process. Thus the bulk properties of the material undergoes little to no phase change which is often a desirable result. Since then, plasma nitriding techniques have continued to expand from conventional direct current plasma nitriding (DCPN), including plasma ion immersion implantation, inductive radio frequency

(RF), active screen, through cage, and cathodic cage plasma nitriding techniques.

2.2.3.1 Direct Current Plasma Nitriding

Conventional direct current plasma nitriding (DCPN) is the most common type of plasma nitriding used today. DCPN is performed in a vacuum chamber with a differential voltage potential applied between the component to be nitrided and the furnace wall (anode). A large negative electric potential is applied to the work piece which accelerates electrons away from the cathode. These accelerated electrons cause a cascade effect in the surrounding gas which produces positive ions. The positive ions in turn are accelerated toward the workpiece to which the negative voltage is applied, as shown in Figure 2.2 [2]. For nitrogen based gases, the positive ions that are accelerated to the workpiece are nitrogen ions, therefore producing nascent nitrogen that can diffuse into the workpiece. These nitrogen ions can also sputter the surface atoms which then reacts with active nitrogen in the plasma, redeposits on the surface, decomposes, and diffusing nitrogen ions into the surface.

Although the DCPN has some remarkable advantages compared to gas nitriding or salt bath nitriding technologies, such as not requiring dangerous toxic chemicals and lower operating temperatures, it also has its drawbacks [2]. One of the disadvantages is the hollow cathode effect (HCE). This occurs when there is a specific geometry between surfaces at a given pressure and voltage where the electrons and ion resonate. The resonating plasma causes intense localized heating that can produce localized heating and melting. Edge effects are also a disadvantage for DCPN, which is caused by concentrated electric field at corners and edges of the work piece. This dense field attracts an increased quantity of positive ions, resulting in localized heating due to increased ion bombardment intensity which also results in a non-uniformed nitriding. Another problem with DCPN is arcing on the surface of the

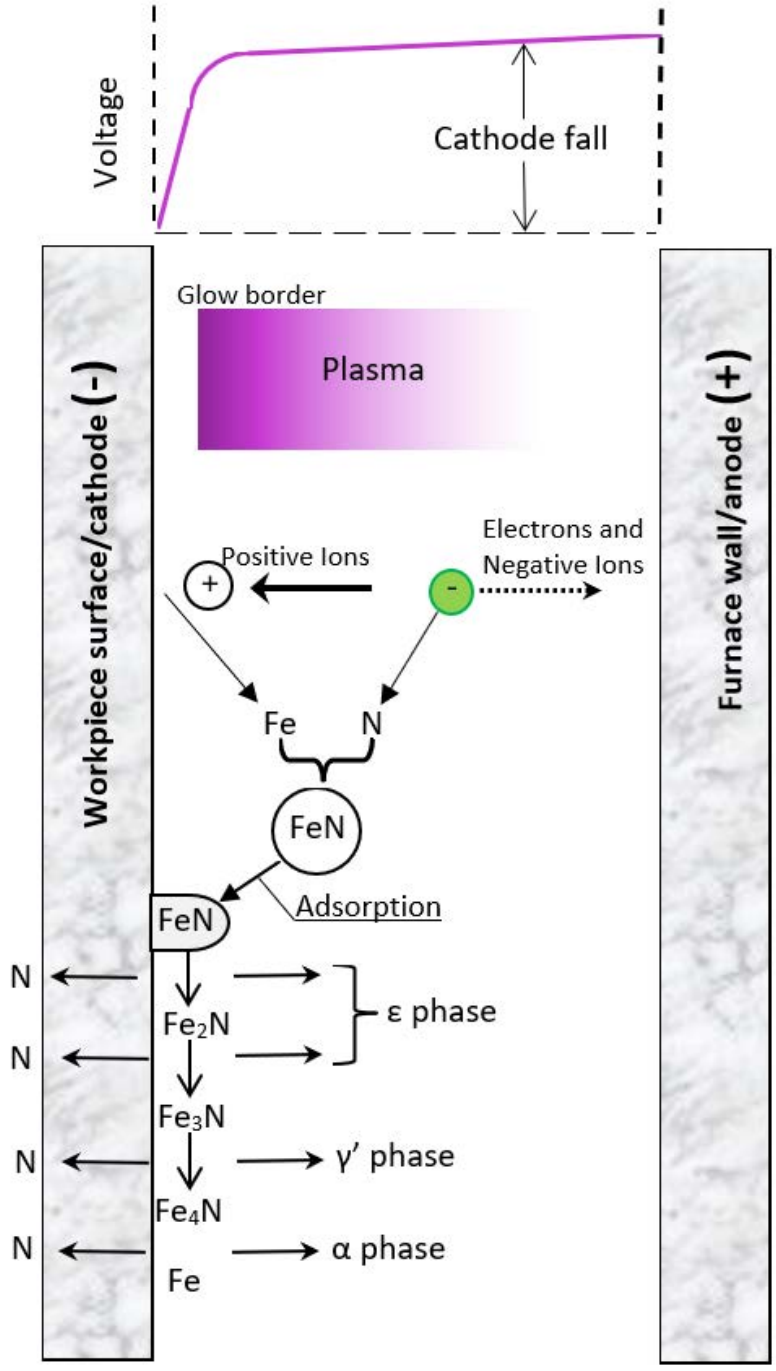

Figure 2.2: Diagram of direct current plasma formation. Adapted from [2].

work piece. This can be caused by surface contamination or as a side effect from the edge effect. Intense arcing can quickly vaporize and damage the work piece surfaces.

2.2.3.2 Active Screen Plasma Nitriding

Active screen plasma nitriding (ASPN), also called through cage plasma nitriding [76], is a relatively new nitriding method. It was invented by Jean Georges who patented this technique in 1999 [77]. In ASPN, the plasma is formed on a cathode with openings that allow the nitrogen ions in the plasma to pass through it. The workpiece is normally at a floating potential so that there are no electrostatic forces on the workpiece, though the workpiece can be subjected to a voltage bias. Heating of the workpiece is achieve through radiative heating from the active screen, which is heated by the plasma on the active screen. This results in a relatively uniform temperature distribution on the workpiece with no edge effects. Because the plasma is not formed on the workpiece there is also no damage from arcing that may occur during plasma nitriding. Cathodic cage plasma nitriding (CCPN) is similar to ASPN except that the work pieces is completely encloses within the cathode [17], as shown in the schematic view of a CCPN setup of Fig. 2.3*[3].

*[3] Reprinted from Surface and Coatings Technology, 201 / 6, C. Alves, F.O. de Araújo, K.J.B. Ribeiro, J.A.P. da Costa, R.R.M. Sousa, and R.S. de Sousa, Use of cathodic cage in plasma nitriding, 2450-2454, Copyright (2006), with permission from Elsevier. Reprinted from The Lancet, Vol. 201, C. Alves, F.O. de Araújo, K.J.B. Ribeiro, J.A.P. da Costa, R.R.M. Sousa, and R.S. de Sousa, Use of cathodic cage in plasma nitriding, 2450-2454, Copyright (2006), with permission from Elsevier.

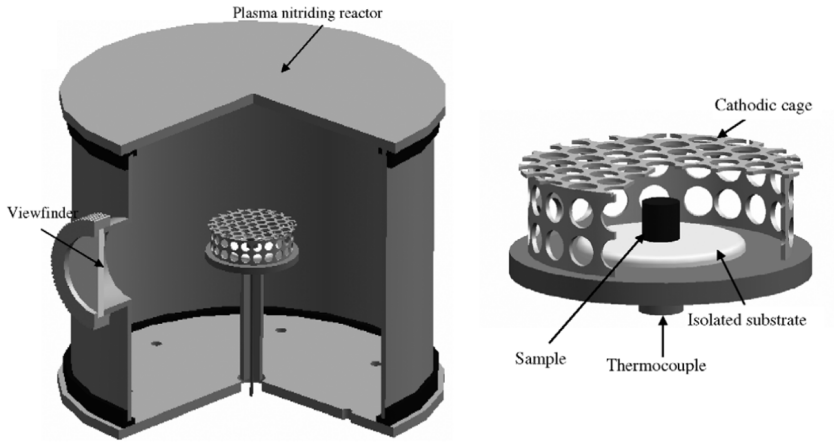

Figure 2.3: Schematic view of the reactor ion nitriding, showing the sample inside the cathode cage. Reprinted with permission from [3]*.

2.3 Mechanical Testing

Though a seemingly simple concept, material hardness is a properties that represents an effect of complex plastic and elastic stress fields in the material being tested [78]. Hardness is the measure of the materials resistance to localized plastic deformation and how the material will resist abrasion [79]. The first well known hardness tests used the Mohs scale. Developed in 1812 by a German mineralogist Friedrich Mohs, the Mohs scale is based on ten arbitrary natural minerals and the ability of one material to be able to scratch another, ranging from 1 for talc to 10 for diamond [80].

The next major improvement in hardness testing was the Brinell test, which was an indentation technique developed in 1900, as more systematic quantitative hardness techniques were needed [5]. Basic limitation of the Brinell test, which included large indent impressions and that harder steels could not be tested, lead to the the development of the Rockwell and the Vickers test methods in 1919 and

1925, respectively. The Vickers microindentation hardness test was developed at the same time as the Vickers macroindentation method [81]. As macrohardness test are indentation loads of 1 kgf or greater, microhardness test have lower applied forces that ranges from 1 to 3000 gf [5]. In 1936, Frederick Knoop modified the Vickers hardness test by changing the indenter's shape and the method used for calculation. Today hardness test may be classified with various criteria, including magnitude of indentation load, nature of the test, such as static, dynamic, or scratch, and type of measurement [78].

2.3.1 Scratch Testing

The scratch resistance of thin films is a measure of the layer to withstand abrasion without fracturing [4]. As diagrammed in Fig. 2.4 load is applied to the indenter F_N and then a tangential force F_T is applied. The coefficient of friction, μ is calculated with EQN 2.1 [4]. In some cases, a lateral force F_L can also be applied along with F_T but normally a single tangential force is applied.

$$\mu = \frac{F_T}{F_N} \tag{2.1}$$

2.3.2 Indentation

2.3.2.1 Brinell

The Brinell hardness test, diagrammed in Fig. 2.5*, is a simple indentation test that consist of applying a load, ranging from 500 to 3000 kgf, to a flat surface using a 5 or 10 mm diameter tungsten carbide ball [5]. The load time is from 10 to 30 seconds and is required to ensure that the plastic deformation of metals has reached

*[5] Used with permission of ASM International, from ASM Handbook, Volume 8: Mechanical Testing and Evaluation, Edward L. Tobolski and Andrew Fee, 8, 1999; permission conveyed through CopyrightClearance Center, Inc.

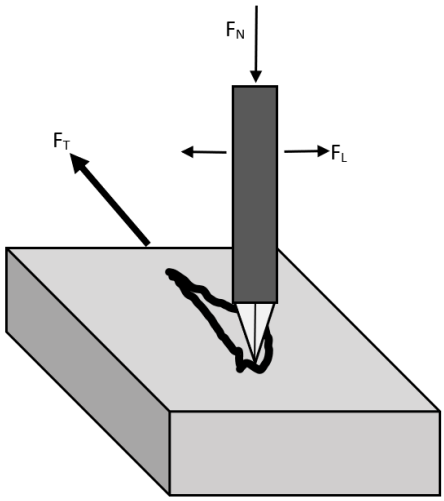

Figure 2.4: Configuration of an indentation scratch test. Adapted from [4].

equilibrium. The size of the round impression that is left after the load is remove is measured with a low-powered microscope.

The Brinell hardness number (HB) calculated in using the following equation:

$$HB = \frac{2P}{\pi D(D - \sqrt{D^2 - d^2})} \tag{2.2}$$

where P is load (in kgf), D is ball diameter (in mm), and d is diameter of the indentation (in mm) [78]. The ball size and force applied should be chosen such that the impression made on the sample should be between 24.0 and 60.0 percent of the ball diameter.

2.3.2.2 Vickers Hardness

Vickers hardness testing, originally known as the 136 degree diamond pyramid test, was introduce in England in 1925 [5]. Similar to the Brinell method, a defined shape is pressed into material with a known force and then removed which is shown

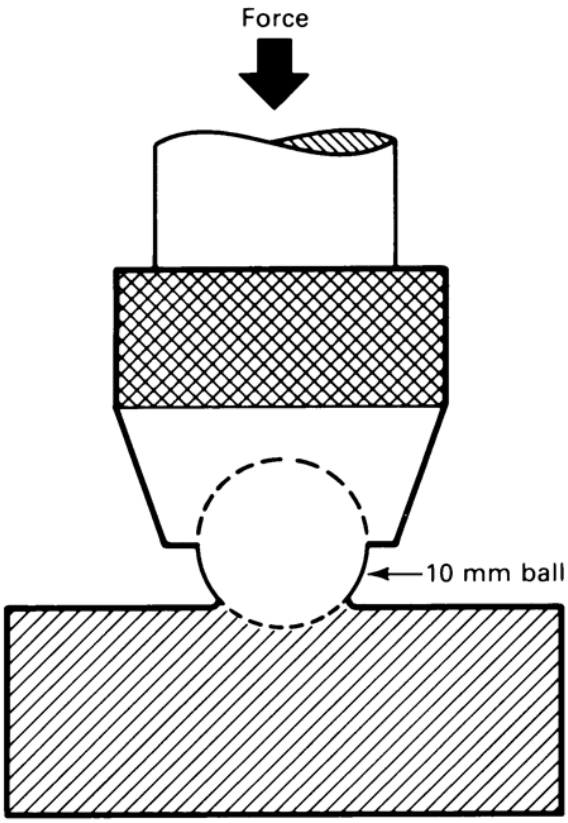

Figure 2.5: Brinell hardness test diagram. Used with permission of ASM International, from ASM Handbook, Volume 8: Mechanical Testing and Evaluation, Edward L. Tobolski and Andrew Fee, 8, 1999; permission conveyed through CopyrightClearance Center, Inc. [5]*.

in Fig. 2.6 [5]*. The resulting indentation diagonals are measured to find its surface area and then use with the applied force to calculate the hardness. Traditionally the processes were divided categories of macroindentation and microindentation, but a more recent technology has allowed for nanoindentation.

To perform the Vickers hardness test, the squared-based pyramidal diamond indenter is pressed into the material of interests with a predetermined load between

*[5] Used with permission of ASM International, from ASM Handbook, Volume 8: Mechanical Testing and Evaluation, Edward L. Tobolski and Andrew Fee, 8, 1999; permission conveyed through Copyright Clearance Center, Inc.

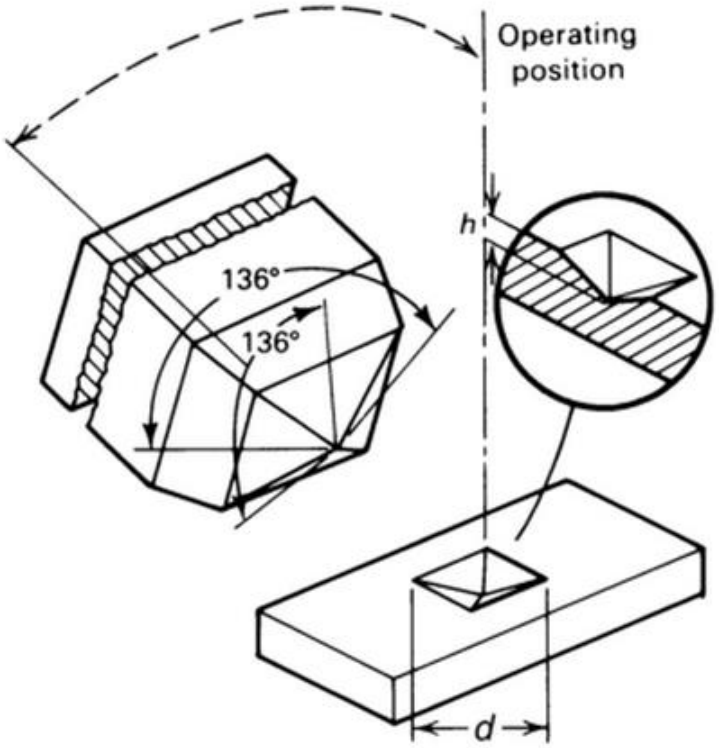

Figure 2.6: Vickers hardness testing diagram. Used with permission of ASM International, from ASM Handbook, Volume 8: Mechanical Testing and Evaluation, Edward L. Tobolski and Andrew Fee, 8, 1999; permission conveyed through Copyright Clearance Center, Inc. [5]*.

1 and 120 kgf [5]. After the indenter has fully stopped under desired loading, the force is applied of another 10 to 15 seconds and then removed. The resulting imprint diagonals are measured in millimeters. The geometry of the indenter is known and is used to correlate the force applied to the surface area of the indent. EQN 2.3 formula is used to calculate the Vickers hardness,

$$HV = \frac{2Psin(136/2)}{d^2} = \frac{1.8544P}{d^2} \tag{2.3}$$

where, P is the applied load in kgf and d is the diagonal length measured in

millimeters.

The Vickers hardness number is expressed in the format 440 HV30/20, where 440 is the calculated hardness from EQN 2.3, HV is the indication that Vickers hardness was used, 30 is the applied force, and 20 is the dwell time in seconds that the full load was applied. If the dwell time was between 10-15 seconds, it is not normally noted in the hardness.

2.3.2.3 Rockwell Hardness

Rockwell hardness testing is the most common method used to measure hardness [79, 5]. The main reason that it is the most widely used method is the simplicity to perform and the low degree of operator skill. The test is performed using either a 1/16, 1/8, 1/4, or 1/2 inch diameter steel sphere or a conical diamond (Brale) indenter with a 120 degree point. A major difference between Brinell and Rockwell hardness testing is the use of a minor load to establish a zero datum reference depth, which increases the accuracy of the measurement [5].

Rockwell test consists of two types: Rockwell and superficial Rockwell [5]. Rockwell has a minor load of 10 kgf with major loads of 60, 100, or 150 kgf while superficial Rockwell minor load is 3 kgf and major loads of 15, 30, or 45 kgf. With both the low and high pressure test, a diamond cone or a hardened sphere may be used as the indenter. The hardened ball indenters are used for testing softer materials, such as annealed steels and various nonferrous metals, and have diameters of 1/16, 1/8, 1/4, and 1/2 inches. While hardened steel balls have traditionally been used, they are being phased out and replaced by tungsten carbide. The Rockwell diamond indenters are used for harder material testing, specifically materials with hardness greater than 100 HHRB and 83.1 HR30T.

2.3.2.4 Nanoindentation

Nanoindentation is an indentation process that is capable of measuring hardness and reduced modulus of thin layers down to 30nm [4]. Also known as instrumented indentation testing, depth-sensing indentation, continuous-recording indentation, and ultra-low-load indentation, nanoindentation is a relatively new form of mechanical testing which greatly enhances capabilities of traditional hardness testing [5]. Nanoindentation not only measures hardness but can provide elastic properties from the same indentation data. It is capable of measuring very small volumes and is considered a nondestructive test.

2.4 Corrosion Testing

Electrochemical corrosion testing is a simple way measure values that correlate to how a material will respond to various corrosion mechanisms. Corrosion is a chemical process and is driven by differential potential in a given system attempting to achieve the lowest energy state. These potentials can be measured for particular solution by applying energy into the system (voltage potential) and the reaction rates measured via quantity of electrons exchanged under the assumption that the reaction is known. One of the most common corrosion test is large scale anodic polarization tests in a 3.5 wt. % NaCl solution.

2.4.1 Basics

In the early 1800's, Michael Faraday demonstrated that electrochemical reactions follow normal charge related chemical stoichiometric relations [7]. Faraday's findings resulted in rules that became known as Faraday's Laws. Faraday's First Law: the mass m, of an element discharged at an electrode is directly proportional to the amount of electrical charge Q, passed through the electrode [7]. Faraday's Second

Law: if the same amount of electrical charge Q, is passed through several electrodes, the mass m, of an element discharged at each number of moles of the electrons z, required to discharge one mole of the element from whatever material is being discharged at the electrode. Relating the mass loss rate, $\dot{m}$, to the charge density rate, q/t, gives the following:

$$\dot{m} = \frac{q}{t} \times \frac{AM}{nF\rho} \tag{2.4}$$

where AM is atomic mass, n is the number of electrons lost per atom oxidized, and ρ is the material mass density [7]. By combining Faraday's principles with electrochemical reactions of known stoichiometry, electrochemical corrosion rate measurements can be correlated to the mass loss rates or penetration rates based on Faraday's Laws [82].

Equivalent weight, EW, is the mass in grams of the alloy that will be oxidized with a charge exchange of one Faraday [82]. For pure elements, EW is given by:

$$EW = \frac{AM}{n} \tag{2.5}$$

EW is more complex for alloys with multiple elements and also many elements exhibit more than one valence value. To calculate the electron equivalent for 1 g of an alloy, Q is:

$$Q = \sum \frac{n_i f_i}{W_i} \tag{2.6}$$

where n_i is the valence of i^{th} element, f_i is the mass fraction of i^{th} element, and W_i is the atomic weight of i^{th} element in the alloy. Therefore, the EW of the alloy is the reciprocal of this quantity:

$$EW = \frac{1}{\sum \frac{n_i f_i}{W_i}} \tag{2.7}$$

Normally only elements above 1 mass percent are included when calculating EW [82].

2.4.2 Potentiodynamic Polarization Measurements

Potentiodynamic polarization technique has been widely used for many years and is a well established corrosion technique [83, 84, 85, 86, 8, 6]. This technique can be used to determine corrosion rates and is based upon the principle of mixed-potential theory [9]. Corrosion potential, E_{corr}, also called open-circuit potential (OCP) in traditional measurement techniques, is a mixed potential that is defined to be the potential when the anodic and cathodic reaction are equal. It should be noted that OCP is ideally equal to E_{corr} as traditional measurements required two separate measurement scans to obtain anodic and cathodic curves but scans are now commonly performed in a single measurment scan resulting in drift of E_{corr} during the cathodic scan. E_{corr} is not measured directly but is derived from corrosion current density measurements with a potentiostat. A basic setup of an anodic polarization circuit for potentiodynamic measurements is shown in Fig. 2.7 and typically consists of a potentiostat, electrolyte, auxiliary electrode, working electrode, and reference electrode [6].

The WE is the interface of interest, consisting of the test material with a known area exposed to the electrolyte within a sample holder. The auxiliary electrode, also called a counter electrode (CE), is an additional interface that has a sole purpose to act as an anode or cathode to the working electrode (WE) [7]. It is placed in the electrolyte with the WE and traditionally has been made of platinum or a platinized material. Graphite can be used but can become easily contaminated due to porosity

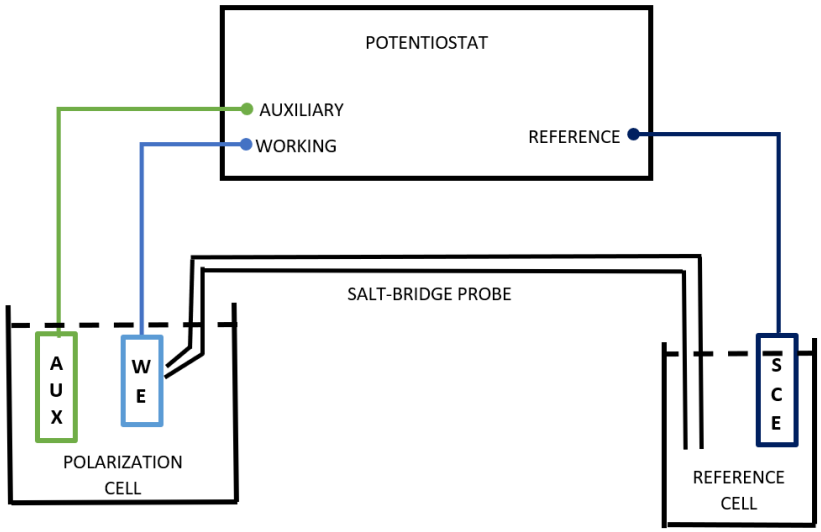

Figure 2.7: Schematic wiring diagram of potentiostat. Adapted from [6].

[6]. More recently, the use of glassy carbon, also called vitreous carbon, electrodes has become more prevalent due to its low porosity resulting in ease of maintenance.

The reference electrode (RE) is a third electrode introduced in the circuit as it maintains a known equilibrium reaction potential. It can be placed in the electrolyte with the WE and CE or in a second container electrically connected via a salt bridge. While the standard hydrogen electrode (SHE), based on the hydrogen reaction with platinum, has traditionally been used though a source of hydrogen gas typically makes its use impractical. The most commonly used REs are the saturated calomel electrode (SCE), Ag/AgCl reference electrode, and Hg/Hg_2SO_4 electrode [7].

A basic potentiostat's circuitry using an OpAmp is shown in Fig. 2.8 [7]. The WE is kept at ground potential and the potentiostat applies voltage to the CE to control the potential between the RE and WE while measuring current through the WE [7]. Ideally, no current flows through the RE, only the CE and WE. The current and the potential between the RE and WE are recorded. For potentiodynamic anodic

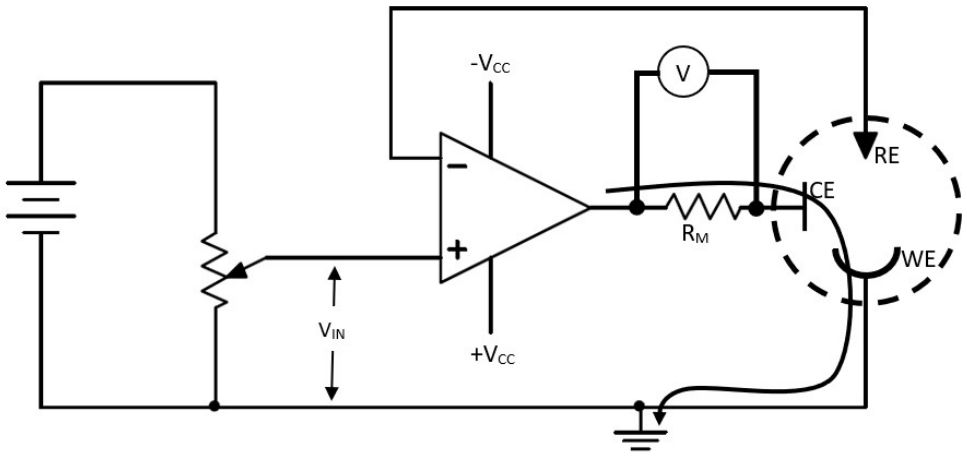

Figure 2.8: Configuration of op amp to function as a potentiostat. Adapted from [7].

polarization measurements, the potential is varied with time and potential plotted on the y-axis. The measured current, I_{app}, in EQN 2.8 is divided by WE area, A and current density, i_{app} is plotted on the x-axis on a log scale with units of µm/cm^2.

$$i_{app} = \frac{I_{app}}{A} \tag{2.8}$$

The polarization measurements in the region near E_{corr} are used to calculate corrosion rates. One method used is polarization resistance technique. The polarization resistance (R_p) is defined as:

$$R_p = \left(\frac{dE}{di}\right)_{E_{corr}} \tag{2.9}$$

which is the slope of the polarization curve with units of Ω/cm^2, where $i_{app} = 0$ as shown in Fig. 2.9 [8]. Corrosion current density, i_{corr}, can be calculated using the Stern-Geary equation [84]:

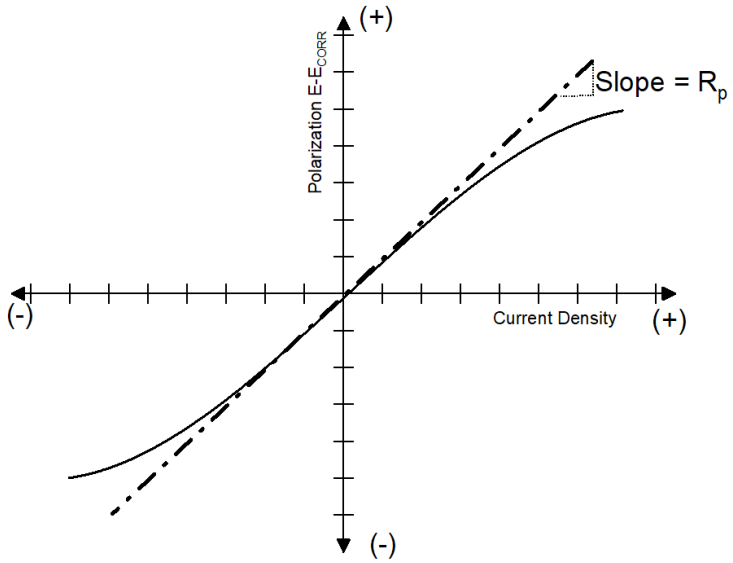

Figure 2.9: Hypothetical linear polarization plot of applied potential deviation from E_{corr} versus current density i_{app}. Adapted from [8].

$$i_{corr} = \frac{B}{R_p} \tag{2.10}$$

where B is a parameter based on Tafel slopes:

$$B = \frac{\beta_a \beta_c}{2.303\,(\beta_a + \beta_c)} \tag{2.11}$$

where β_a and β_c are the anodic and cathodic Tafel slopes. The Tafel slopes can be measured by plotting the polarization curve with linear potential versus current density on base 10 logarithmic scale [85]. An example of the Tafel slope extrapolation is shown in theoretical Tafel plot of Fig. 2.10 illustrating the Tafel extrapolation method [9]. More modern methods of determining Tafel slopes and R_p uses computer analysis to fit the polarization curve in the region near E_{corr}, called the pre-Tafel

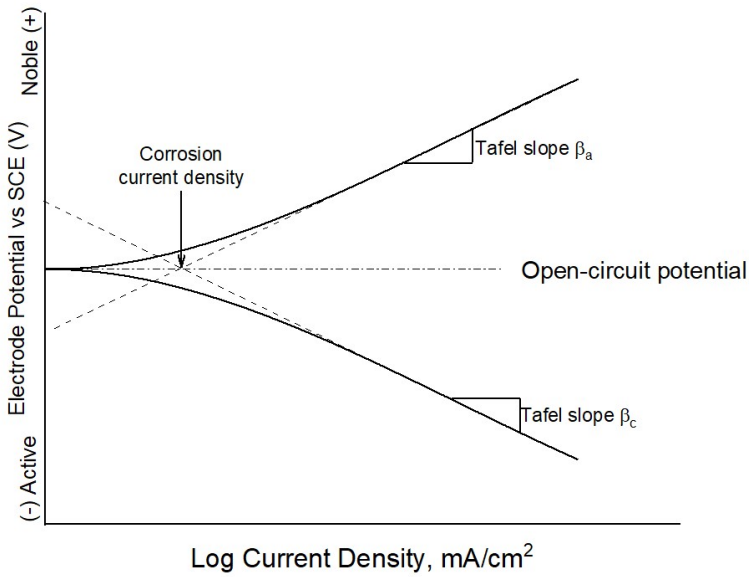

Figure 2.10: Theoretical Tafel plots illustrating the Tafel extrapolation method. Adapted from [9].

region [85, 86, 87].

$$i_{app} = \frac{\beta_a * |\beta_c|}{(\beta_a + |\beta_c|)\, 2.303 R_p} * \left[exp\left(\frac{2.303(E_{app} - E_{corr})}{\beta_a}\right) - exp\left(\frac{-2.303(E_{app} - E_{corr})}{\beta_c}\right)\right] \tag{2.12}$$

After parameters for i_{corr} are obtained, Faraday's Law can be used to calculate the corrosion rate in terms of penetrating rate CR where:

$$CR = K_1 \frac{i_{corr}}{\rho} EW \tag{2.13}$$

where K_1 is a conversion factor = 3.27E-3 mm-g/(µ-A-cm-yr), ρ is the material density in g/cm^3, and EW is the equivalent weight from EQN. 2.7. CR has units of

mm/yr, i_{corr} in µm/cm^2, and EW is considered dimensionless due to K_1 [82].

2.5 Materials

This section covers a literature review of 316, HT-9, T91, and Zircaloy-4. First, an introduction to steels is discussed. Second, background information of each material is reviewed. This is followed by reviews pertaining surface nitridation and nitrogen interactions of 316, HT-9, T91, and Zircaloy-4.

2.5.1 Steels

Steels are alloys composed of iron and other elements [88]. They divided into four major categories which are carbon steels, alloy steels, tool steels, and stainless steels [89]. Carbon steels containing low amounts of alloying elements have three main subcategories, low, medium and high carbon. Alloy steels are subdivided into low-alloy and high-alloy steels and contain various alloying elements. Common elements used in alloy steels are aluminum, copper, manganese, molybdenum, niobium, nickel, titanium, and silicon. High-yield-strength steels, such as HY-100, are included in low-alloy steels [89]. Maraging steels contain low carbon content and 15 to 25% Ni as the primary alloying element and rely on the formation of soft martensite. During aging, the formation of intermetallic compounds strengthens the soft martensite. Tools steels rely on the formation of tungsten, molybdenum, and cobalt carbides and have high heat resistance and durability [89].

Stainless steels have high Cr content which contribute to their corrosion resistance. With sufficient Cr content, chromium oxide layer that is formed on the surface forming a passivation layer. Stainless steels are categorized as ferritic, martensitic, duplex (ferritic-autenitic), precipitation hardening, and austenitic. Figure 2.11 shows the classification of stainless steels based on Ni and Cr content [10].

Standard ferritic stainless steels are nickel-free and contain 10.5 to 27% Cr. They

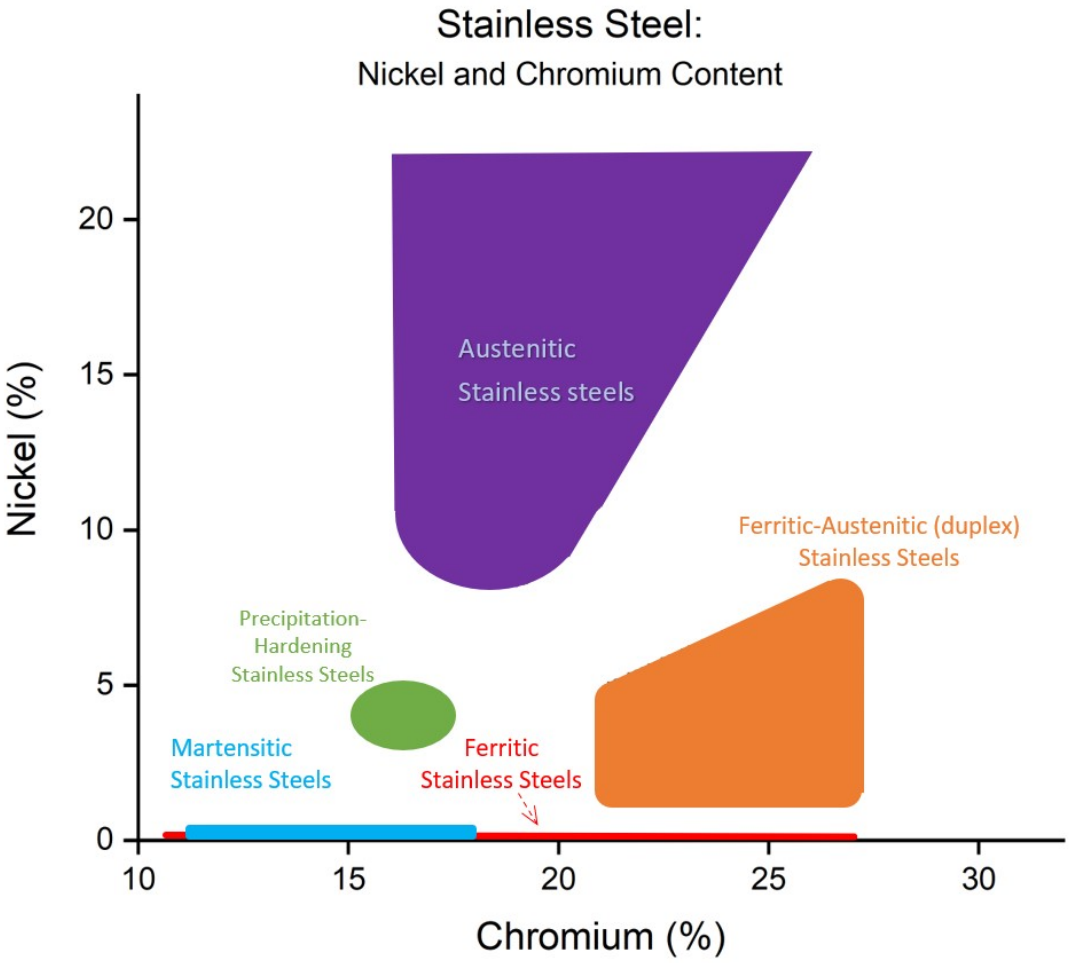

Figure 2.11: Graph of classification of stainless steels based on Ni and Cr content. Adapted from [10].

are not hardenable by heat treatment and have less critical anticorrosion applications because of their low carbon content which is less than 0.2% [10]. Ferritic steels have a body centered cubic structure which is responsible for its magnetic nature, differing from all other types of stainless steel [90]. Martensitic steels typically contain 11.5 to 18% Cr and up to 1.2% C with nickel sometimes added [10]. They have modest corrosion resistance and are hardenable by heat treatment. Austenitic stainless steels have a face-centered cubic (FCC) structure which is stabilized with nickel and manganese. The FCC structure makes them non-magnetic and not hardenable using heat treatment.

2.5.2 Stainless Steel 316L

Stainless steel 316 is an austenitic chromium-nickle stainless steel containing molybdenum and is one of the most used types of stainless steel in the world. 316L is widely used in light water reactors (LWR) as structural materials [91]. It has high corrosion resistance and is resistant to intergranular stress corrosion cracking, which is improved by reducing the carbon content [92]. One of the drawbacks of 316L is it has relatively poor swelling resistance, especially compared to HT9 [93]. At temperatures above 300 °C, it is estimated to have a steady-state swell rate of 1%/dpa [94]. Austenitic stainless steel present good creep resistance at higher temperatures and are candidates for fuel cladding in LFR reactors for temperatures up to 600 °C but have drawbacks of relatively high void swelling, radiation-induced segregation, and irradiation creep [95].

2.5.2.1 Nitrogen Modified Surfaces

Nitriding at temperatures below 450 °C forms a nitrogen rich modified surface layer on austenitic stainless steel and is associated with the absence of chromium nitride or carbide precipitation [96]. First reported by Zhang and Bell in 1985 [97],

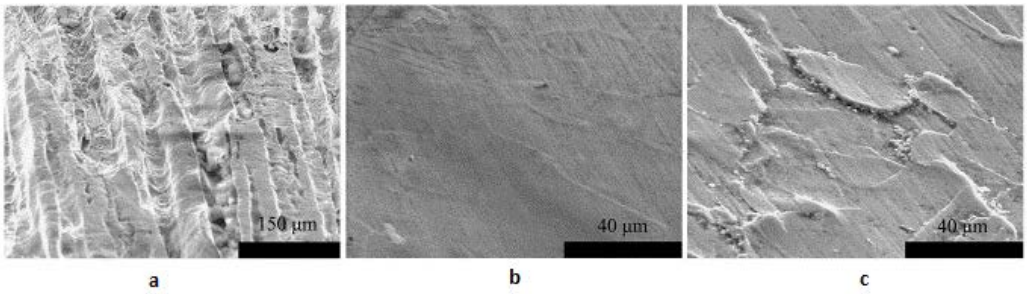

Figure 2.12: Crevice corrosion testing comparison of nitrided 316L after 60 days in 10% NaCl aerated solution at 50 °C (a) unnitrided (b) nitrided at 400 °C (c) nitrided at 450 °C. Reprinted with permission from [11]*.

a parallel investigation by Ichii in 1986 named it "S-phase" after x-ray diffraction spectrometry revealed detected peaks that were not previously indexed [98, 96]. The term expanded austenite (γ_N) was later used by Leyland in 1993 [99] and the two terms are now used interchangeably. The high nitrogen concentration results in a face-centered structure like austenite but the interstitial nitrogen distorts the lattice to a face-centered tetragonal. The lattice parameters are increased by up to 10% resulting in a high compressive stress in the nitride layer. The compressive stress contributes to the layer's corrosion and wear resistance with a hardness up to 14 GPa [18, 100, 101, 102, 103]. Figure 2.12* shows the surface morphology of nitrided 316L after 60 days of crevice corrosion testing using a 10% NaCl aerated solution. The nitrided 316L at 400 °C has improved corrosion resistance [11].

The S-phase is described as a supersaturated metastable phase and its decomposition is dependent on time and temperature. In Fig. 2.13 the transformation of 50%

*[11] Reprinted from Corrosion Science, 48 / 6, A. Fossati, F. Borgioli, E. Galvanetto, and T. Bacci, Corrosion resistance properties of glow-discharge nitrided AISI 316L austenitic stainless steel in NaCl solutions, 1513-1527, Copyright (2006), with permission from Elsevier. Reprinted from The Lancet, Vol. 48, A. Fossati, F. Borgioli, E. Galvanetto, and T. Bacci, Corrosion resistance properties of glow-discharge nitrided AISI 316L austenitic stainless steel in NaCl solutions, 1513-1527, Copyright (2006), with permission from Elsevier.

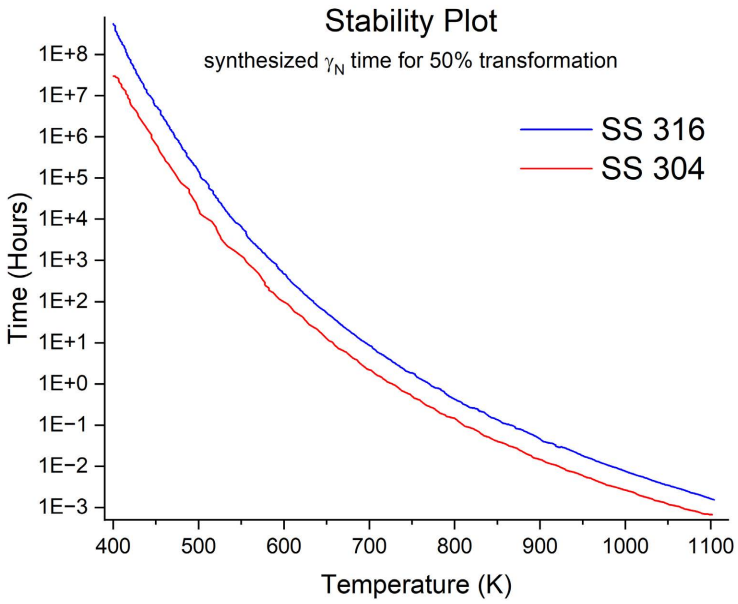

Figure 2.13: Plot of time against temperature for the transformation of 50% of the S-phase. Adapted from [12].

of the S-phase is plotted versus time for 316 and 304 [12]. When above the plotted line or for nitridation above 450 °C, the S-phase transforms to a compound layer of metal nitrides and a mixture of ferrite and austenite [96]. While there is consistency that one of the mixtures is austenite, the second mixture sources describe as ferrite [97, 104], martensite [105, 106] or pearlite [107].

The CrN precipitates in the lamellar structure results in increase of hardness up to 17 Gpa via precipitation hardening. This consumption of Cr removes the stainless property of the passivisation layer resulting in a decrease in corrosion resistance. The corrosion resistance decrease can seen in the sample nitrided at 450 °C in Fig. 2.12 which had more corrosion compared to 400 °C. The transition of the S-phase has been attributed to the increased mobility of chromium [19]. CrN precipitation destabilizes

the austenite promoted by the interstitial and are often noted to start at the grain boundaries . One theory is the higher diffusion along the grain boundary decreases the nitrogen content which results in the collapse of the metastable phase into a laminar structure [107].

The use if plasma nitriding in nuclear reactor environments, while limited, is not completely novel. Ion nitriding has been used in French nuclear power plants since 1992 to improve corrosion and wear resistance of rod cluster control assemblies (RCCAs) and thimble plug assemblies [108]. Areva's HARMONI RCCA has 316L cladding that has been ion nitrided to form an S-phase nitride layer. Aging tests have demonstrated S-phase stability after 500 hr at 380 °C and 8000 hr at 300 °C [104]. The nitrided RCCAs has shown improved wear resistance of more than 90% which significantly increases the lifetime of the RCCA resulting in nitrided HARMONI RCCAs being the design standard since 1992 [109].

2.5.3 HT-9 and T91

HT9 is a 12Cr-1Mo-VW martensitic stainless steel that is primarily used as tubing in high temperature environments. It is one of the potential candidates for use in GIV reactors, such as SFR, SCWR, and LFR at temperatures up to 500 °C [95]. When compared to austenitic stainless steels, HT9 has better thermal properties and compatibility with heavy liquid metals, such as lead. As with other ferritic/martensitic steels, HT-9 excellent swelling resistance as shown in Fig. 2.14* [13]. This can be attributed to their bcc crystal structure and complicated defect-sink interaction. Studies estimates HT-9 has a steady state swelling rate below 0.1%/dpa [13]. One of the draw backs of HT-9 is that it has a higher parasitic neutron cross section

*[13]Reprinted with permission from "Elevated temperature ferritic and martensitic steels and their application to future nuclear reactors" by R. L. Klueh, 2005. International Materials Reviews, 50(5), 287-310, Copyright 2005 by Taylor and Francis.

	Cr	Mo	V	W	Nb	C	Si	Mn	Ni	N
12Cr-1MoVW (HT9)	12	1	0.3	0.5	0	0.2	0.4	0.6	0.5	0
9Cr-1MoVNb (T91)	9	1	0.25	0	0.08	0.1	0.4	0.5	0	0.05

Table 2.1: Nominal weight percent composition of HT9 and T91.

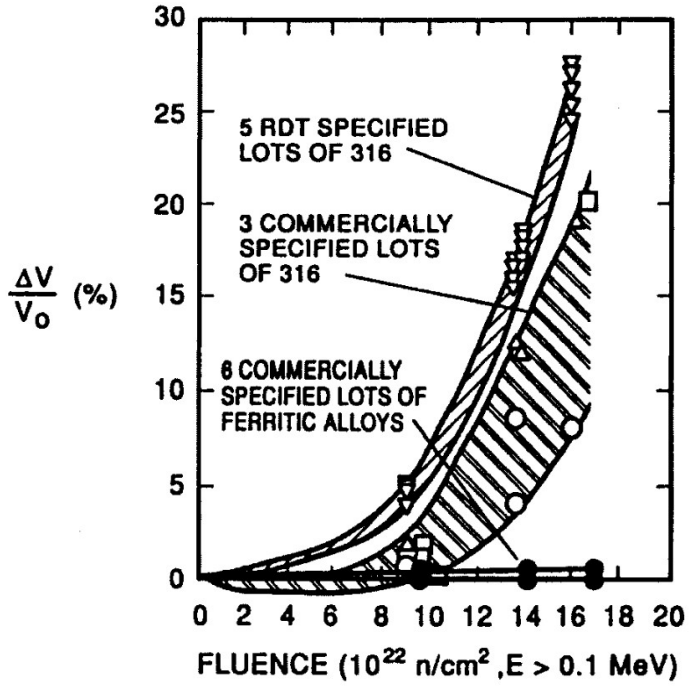

Figure 2.14: Plot of the swelling behavior of ferritic/martensitic steels versus 316 stainless steel irradiated in EBR-II at 420 °C. Reprinted with permission from [13]*.

compared to zirconium based alloys.

T91 is a modified 9Cr-1MoVNb made in the US that is defined as grade T/P91. It is a ferritic/martensitic alloy (9% chromium, 1% molybdenum) steel micro-alloyed with vanadium and niobium, and has a controlled nitrogen content according to ASTM A335, A213 or to EN10216-2 standard under the designation X10CrMoVNb9-1 [110]. T91 has been used extensively in non-nuclear power plant applications, such as tubing in boilers, super-heaters, and heat exchangers. It is a candidate for

reactor fuel cladding due to its good corrosion resistance, high strength, and swelling resistance.

2.5.3.1 Nitriding of HT-9 and T91

While no studies where found for nitriding of HT-9 or T91, studies have been performed on similar alloys. For T91, nitriding of EUROFER 9Cr steel was performed using various industrial nitriding techniques at high temperatures with heat treatments though the study focused on bulk properties [111]. JLF-1 (Fe-9Cr-2W-0.1C) was gas nitrided and chemical stability was tested in molten salt Flinak 600 °C for 2216 hours with findings indicating that surface nitriding can improve compatibility without decreasing thermal conductivity [112]. High temperature nitriding on modified 9Cr-1Mo steel was performed at 650 °C for 100 hours showing significant increase in creep rupture strength but the long high temperature nitriding time decreased rupture ductility [113]. For shorter nitriding times, the rupture ductility increased.

In relation to nitriding of HT-9, there has been nitriding studies performed on 410 stainless steel. Similar to 316, low temperature nitriding improved corrosion resistance [46]. Another study using DCPN demonstrated improved surface hardness of 10-14 GPa and corrosion properties at 500 °C and below [47, 48, 49, 50].

2.5.4 Zirconium Alloys

Zirconium (Zr) is a refractory metal with a closed packed hexagonal (alpha) crystal structure at temperatures below 863 °C. Above this temperature, the crystal structure undergoes an allotropic phase transformation to body center cubic (beta) up to the melting point at 1855 °C. Zr has good corrosion resistance and a low neutron cross section for absorption. As the early reactor designs scaled up in size, the lower parasitic absorption of zirconium allowed for smaller, more compact reactors and less

Common Designation	UNS #	Chemical Composition (wt%)						
		Sn	Nb	Fe	Cr	Ni	O (ppm)	Hf (ppm)
Zr 702	R60702			Fe+Cr <0.2			<0.16%	4.5%
Zircaloy-2	R60802	1.2-1.7		0.07-0.2	0.05-0.15	0.03-0.08	1200-1400	100
Zircaloy-4	R60804	1.2-1.7		0.18-0.24	0.07-0.13	0.03-0.08	1200-1400	100
Zr-2.5% Nb	R60901		2.4-2.8				1200-1400	100

Table 2.2: Composition of common Zirconium Alloys.

fuel loading, it quickly replaced aluminum and stainless steel cladding.

Zirconium based alloys, Zircaloy-2 and 4, are two of the most used cladding materials in the United States. Table 2.2 shows normal compositions for common Zr alloys. One of the major drawbacks with using zirconium alloys as a cladding material is the oxidation in event of a reactor accident. At higher temperatures, the cladding oxidizes rapidly in an exothermic reaction producing zirconium oxide and hydrogen. The oxidation reaction of zirconium alloys becomes significant at temperatures above 1200 °C [95]. At this temperature, this exothermic reaction becomes the dominate energy source driving the reaction. The rapid formation of ZrO_2 results in the production of a large amount of hydrogen gas. The most recent example of this was the Fukushima Daiichi nuclear disaster.

2.5.4.1 Zirconium-Nitrogen Systems

Zirconium Nitride (ZrN) has three stable phases as shown in Fig. 2.15*, alpha, beta, and delta [14]. The alpha phase is a HCP crystal structure and considered a

*[14] Used with permission of Springer Nature BV, from The N-Zr (Nitrogen-Zirconium) System, L. Gribaudo, D. Arias, and J. Abriata, 15(4), 1991; permission conveyed through Copyright Clearance Center, Inc.

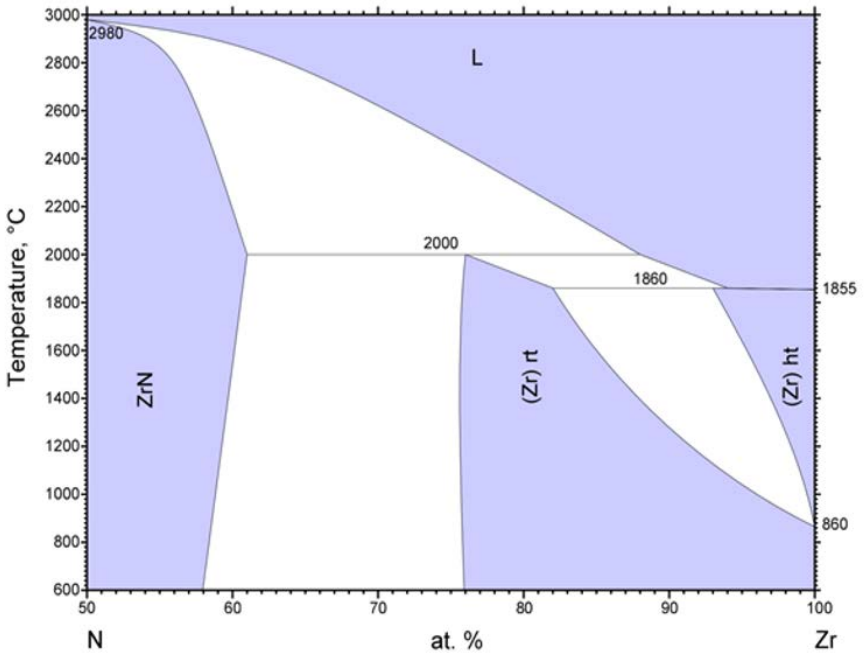

Figure 2.15: Zirconium-nitrogen phase diagram. Used with permission of Springer Nature BV, from The N-Zr (Nitrogen-Zirconium) System, L. Gribaudo, D. Arias, and J. Abriata, 15(4), 1991; permission conveyed through Copyright Clearance Center, Inc. [14]*.

solid solution. Zr undergoes a phase transformation from HCP to BCC at higher temperatures above 863 °C. The delta phase is a simple cubic structure that is also FCC and cF8 Pearson symbol. The expected hardness values of ZrN is 23-42 GPa with and elastic modulus up to 450 GPa. Although it is generally accepted that ZrN is the only stable intermediate compound, many studies have shown another metastable phase Zr_3N_4 [114], which may exist as c-Zr_3N_4 (Th_3P_4 structure, H=30 GPa and bulk molulus=250 GPa) [115], or o-Zr_3N_4 (orthorhombic structure, H=36 GPa) [116, 117]. The o-Zr_3N_4 was metastable and decomposed into ZrN and N_2 upon annealing. Formation of ZrN_x (NaCl structure) with $1.06<x<1.23$ was previously claimed [118].

While there has been no data found for plasma nitriding zirconium or Zircaloy-4, a nitrogen ion implantation in Zircaloy-4 study has been documented [15]. This study suggest that the formation of a ZrN layer could significantly increase corrosion resistance, as seen in Figure 2.16* indicated by reduced current density of nitrogen implanted samples [15].

*[15] Reprinted from Materials Science and Engineering: A, 263 / 1, S.J. Lee, H.S. Kwon, W. Kim, and B.H. Choi, Effects of compositional and structural change on the corrosion behaviour of nitrogen implanted Zircaloy-4, 23-31, Copyright (1999), with permission from Elsevier. Reprinted from The Lancet, Vol. 263, S.J. Lee, H.S. Kwon, W. Kim, and B.H. Choi, Effects of compositional and structural change on the corrosion behaviour of nitrogen implanted Zircaloy-4, 23-31, Copyright (1999), with permission from Elsevier.

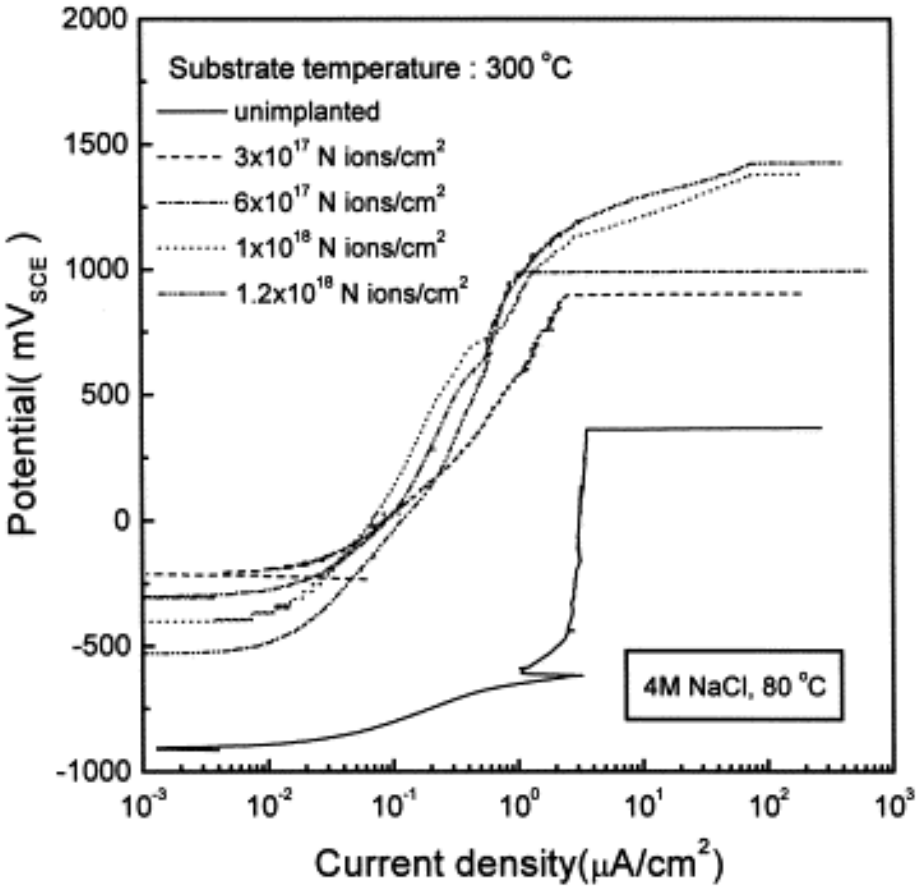

Figure 2.16: Anodic polarization curves of Zircaloy-4 implanted at 300 °C with various nitrogen doses. Tested in deaerated 4M NaCl at 80 °C. Reprinted with permission from [15]*.

3. PLASMA NITRIDING DEVICE

In this chapter the in-lab fabricated plasma nitriding device used for nitriding is described. Following the description of the nitriding setups used for experiments, observations that were made during the fabrication process are discussed.

Numerous problems were identified in the initial design and were been solved. Examples include sever arching when igniting plasma, metallic sputtering and deposition on inner ceramic insulators which cause electrical shortage and inconsistent nitriding results. Various solutions were found to eliminate or alleviate the issues which are discussed in this chapter. For example, anode was redesigned for stable electrical grounding, plasma shielded sample holders were used to replace single ceramic isolation disk, and additional plasma shields were used to isolate thermocouple and power supply feed-throughs.

The nitridation experiments involved various parameters including bias, temperature, time, pressure, cage-to-sample distance, and position of samples within the cage. In addition, cage materials also play an important role. Through systematic studies, it was found that some parameters, such as pressure, are not as important as others. Knowledge on parameter dependence is critical to developing the nitridation technique as a repeatable and controllable technique.

Changing voltage can change sample temperature. Changing distance and height of samples within the cage can change sample temperate as well. On the other hand, temperature and nitridation time are most critical parameters to determine both phase formation and the thickness of the nitride phase.

3.1 General Description of Nitriding Device and Setup

The vacuum chamber for the nitriding device was a 6-way cross made of stainless steel with a 10 inch inner diameter with lengths of 24 inches. The vacuum chamber was electrically connected to earth ground potential and the inner chamber wall acted as the anode for the plasma. The cage platform (cage base) was placed in the center of the chamber on ceramic 3 standoffs 6 inches in height, each having a plasma shield on top. To provide improved electrical isolation from metallic plasma deposition shorting and raise the cage platform to the vertical center of the chamber, the cage platform was connected to 1 inch shielded standoff via each of the 6 inch standoffs. Electrical connections were insulated in ceramic tubes with fitted plasma shields. Voltage was applied to stage platform and acted as the cage base, which was a 2 mm thick titanium plate with a 65 mm diameter. Various cage and sample holder configurations were used for CCPN. The cages were placed on the cage base and voltage potential applied via electrical contact with the base. Figure 3.1 diagrams a typical CCPN setup.

The nitriding device was designed with an adjustable 8 inch diameter ground plate centered above the nitriding cage. The adjustable ground plate was attached to a stainless steel 1/4 inch tube that also functioned as the gas inlet. A gas flow gauge with a built in needle throttle valve at the gas inlet was used to measured and controlled the gas flow rate. The gas outlet was at the bottom of the chamber connected to a rotary oil sealed pump used for vacuum. A needle throttle valve between the chamber and the vacuum pump was used to control the vacuum pressure. Pressure was measured with a Granville-Phillips 275 convection gauge and meter.

Three main sample holder and cage configurations were used. Figure 3.1 shows a typical configuration for Zircaloy 4 cage nitrided at cage potential. For steel nitrided

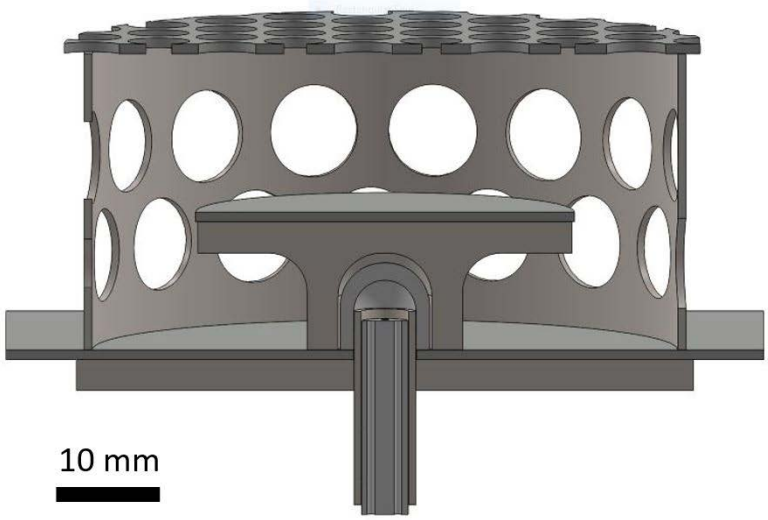

Figure 3.1: Nitriding cage setup for cage bias nitriding of Zircaloy-4.

at lower temperatures and variable pressure, samples were placed on the simple sample isolation holders from Fig. 3.3a. Figure 3.2 shows a typical setup with samples on holders.

For Zircaloy-4 nitriding the cage top was 1 mm thick perforated Zr702 with 1/4 inch staggered holes and a 50% open area spacing. The cage side was 1 mm thick perforated titanium, or Zr702 with 3/8 staggered holes and a 50% open area spacing. The height and diameter of the cage was 30 mm and 60 mm, respectively. The electrically conductive cage was placed on the base and cathodic voltage applied via the cage base.

Two different cages made of 304 stainless steel were used for nitriding steel samples. The first 304 cage was 3 mm thick with 3/16 inch staggered holes and a 50% open area spacing. The cage top was welded to the cage side. The height and diameter of the cage was 40 mm and 60 mm, respectively. The second 304 cage was 1

Figure 3.2: Sample placement

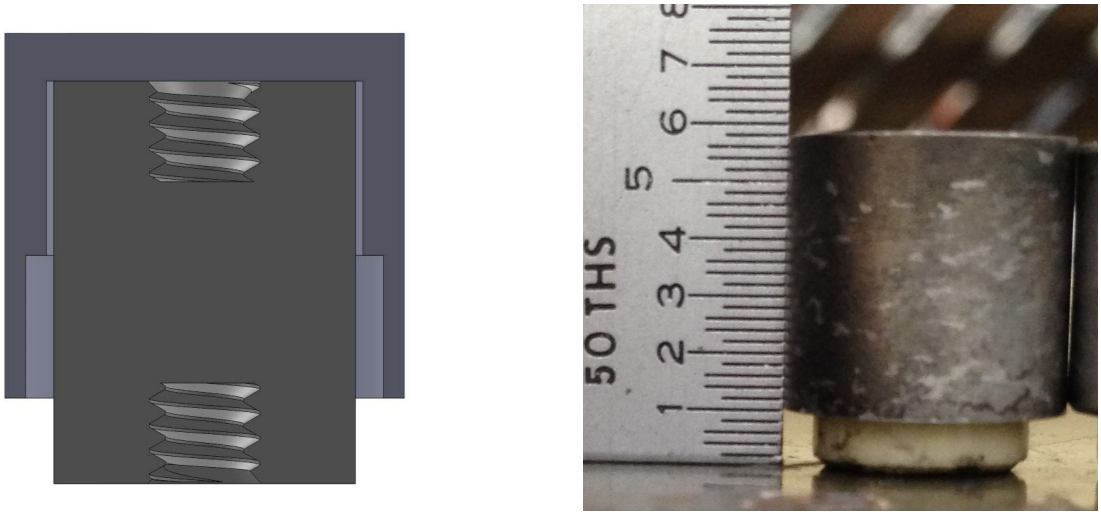

(a) Cross section (b) Photo

Figure 3.3: Ceramic sample holder with plasma shield.

mm thick with 1/4 inch staggered holes and a 50% open area spacing. The height and diameter of the cage was 30 mm and 60 mm, respectively and the cage top was not welded to the cage side.

Three different sample holders were used for CCPN. The first type of sample holder used was a shielded cylindrical ceramic standoff shown in Fig. 3.3. The standoff was a 94335A125 electrical insulating ceramic standoff with a 3/8 inch outer diameter and height of 1/2 inch. The plasma shield was fabricated from 17-4 PH steel to maintain the samples at floating potential. Three shielded ceramic holders were placed in the cage surrounding a 4th shielded sample holder modified for temperature measurements. A K-type thermocouple was mechanically attached to the center sample holder. The sample holder arrangement was later modified using a single sample holder.

A single sample holder was fabricated to allow all samples to be placed on a single holder shown in Fig. 3.4. The single sample holder allowed all samples to be

(a) Dimensions (b) Cross section

Figure 3.4: Steel float sample holder diagram.

placed on a single surface centered radially in the cylindrical cage and vertically to half the height of the cage. This also allowed on samples to sit on a single surface to which the thermocouple was mechanically secured. Another benefit of using a single floating sample holder was that the floating potential was the same for all nitrided samples in the nitridation set.

3.1.1 Temperature Measurement

A K-type thermocouple with a wire diameter of 0.02 inches with a Jenco model 765 thermometer was used to measure temperature. The thermocouple was placed in the center sample holder via alumina insulated feed-through. Temperature measurements were taken via an electrically floating circuit to maintain the thermocouples at floating plasma potential. For nitriding performed with cage voltage biased on the samples, the temperature was measure radiatively through an alumina insulator. The cage bias was supplied to the sample stage by adjusting the sample holder to contact the cage base. Nitriding performed at floating potential, the thermocouple was mechanically secured to the sample holder and the sample holder was raised using an alumina insulator tube.

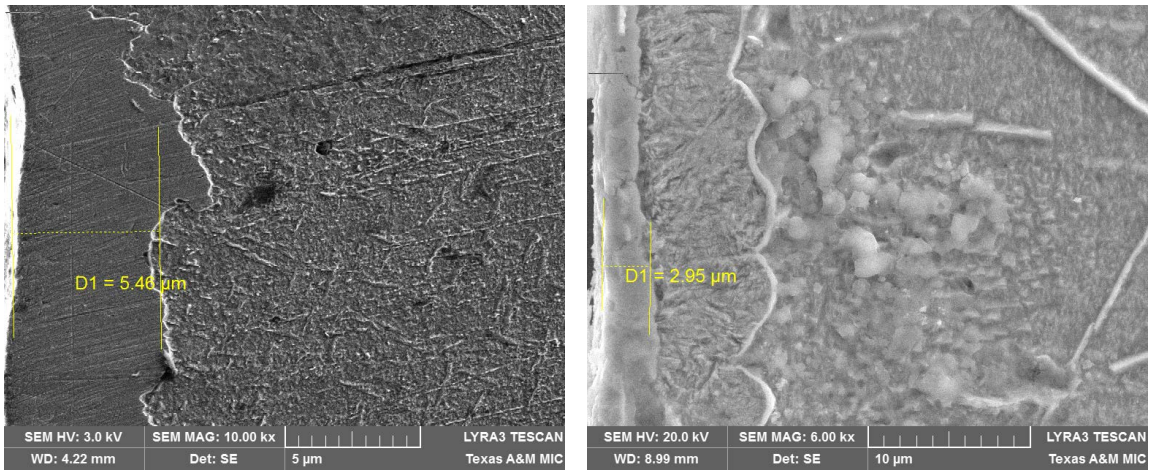

(a) 515 °C (b) 525 °C

Figure 3.5: SEM images of nitrided iron for 1 hour at measured temperature (without adjustment factor applied) 515 and 525 °C showing transformed austenite for the nitrided sample above 525 °C.

The measured temperatures have been adjusted by a factor of 1.135 due to indication that all pure iron samples nitrided greater than 525 °C, such as the examples shown in Fig. 3.5, contained transformed austenite (γ) which forms above 592 °C [119]. The temperature shift may be due to the affects of floating bias potential interacting with the thermocouple meter or lack of power produced from the thermocouple combined with inherent properties of thermometer. As K-type thermocouples produce 0 power at 0 °C, the factor was applied to the measured target Celsius measurements.

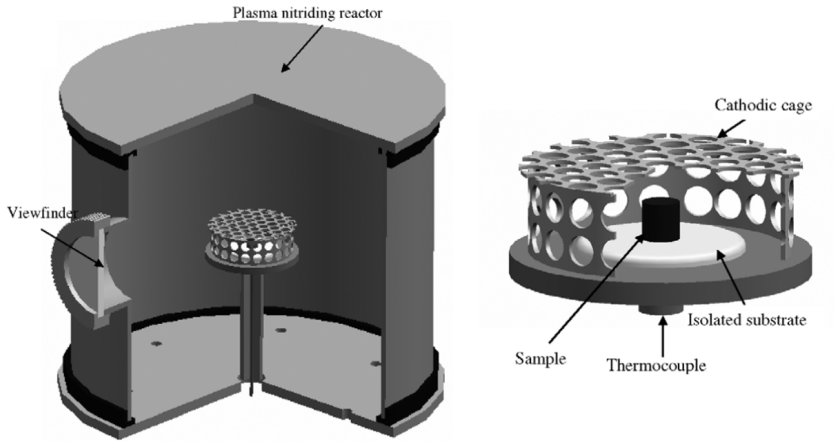

Figure 3.6: Schematics basis of the plasma chamber designed and optimized in this project. Reprinted with permission from [3]*.

3.2 Progression of Building Nitriding Device*

Figure 3.6* shows schematics basis of the plasma chamber designed and optimized in this project [3]. Different from the tradition plasma nitridation technique, this project uses a cathodic cage to stabilize plasma distribution to avoid edge effects. The design can be readily extended to a larger volume for realistic fuel cladding tube treatment. Figure 3.7 shows one image of plasma nitriding when the device is operated.

The initial design of the nitriding system was modeled from the experimental setup used by Alves et al. in 2006 shown in Fig. 3.6 [3]. The initial nitriding device that was built is shown in Fig. 3.8. After a few nitridation, problems were noticed that needed to be addressed for experimental consistency and longer nitriding times.

*[3] Reprinted from Surface and Coatings Technology, 201 / 6, C. Alves, F.O. de Araújo, K.J.B. Ribeiro, J.A.P. da Costa, R.R.M. Sousa, and R.S. de Sousa, Use of cathodic cage in plasma nitriding, 2450-2454, Copyright (2006), with permission from Elsevier. Reprinted from The Lancet, Vol. 201, C. Alves, F.O. de Araújo, K.J.B. Ribeiro, J.A.P. da Costa, R.R.M. Sousa, and R.S. de Sousa, Use of cathodic cage in plasma nitriding, 2450-2454, Copyright (2006), with permission from Elsevier.

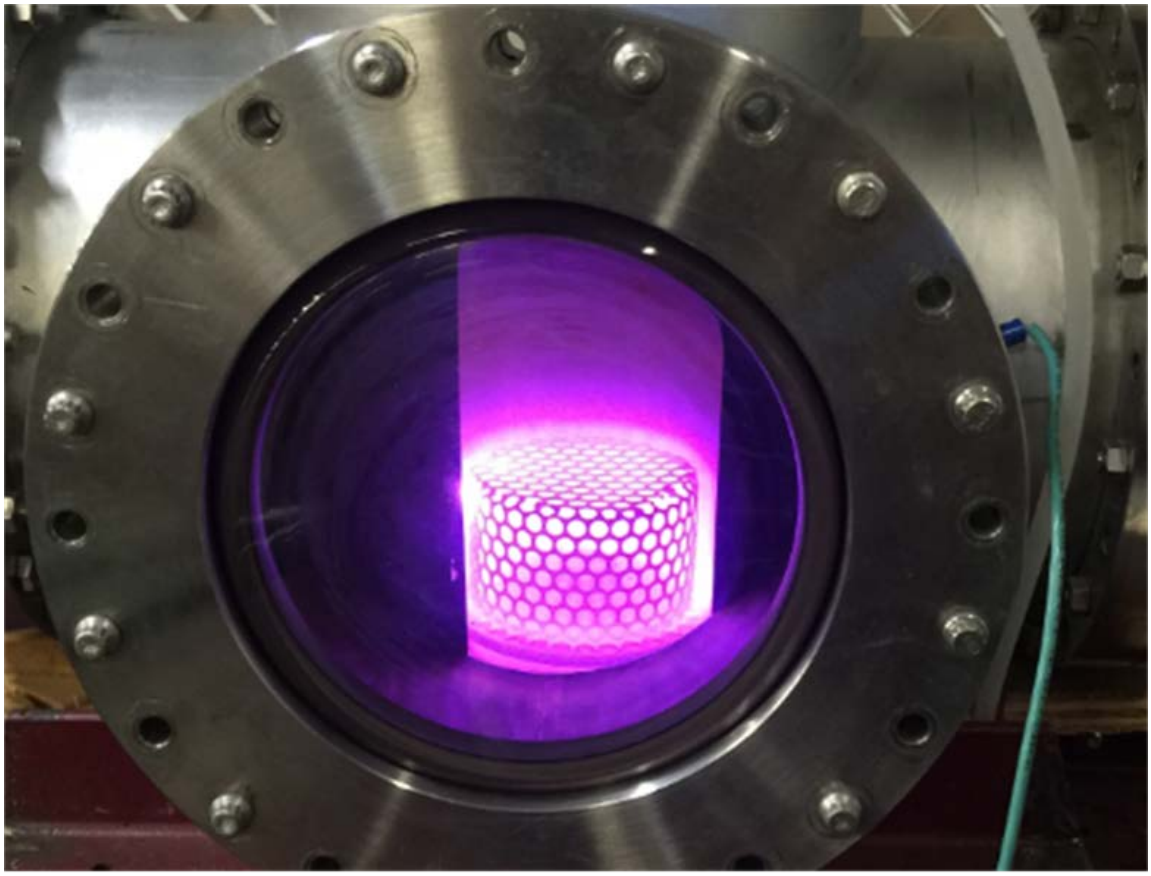

Figure 3.7: An image of plasma nitriding in operation.

Figure 3.8: First nitriding cage setup.

In this section, observational experience from constructing a plasma nitriding device are discussed along with solutions used and hypothesis that could be of use to future work.

The hollow cathode effect (HCE) was typically only formed on one cage opening at a time and the location was unstable. This produced a variable temperature distribution inside the nitriding cage due to the single HCE causing localized energy deposition. This temperature variation produced large variations of the nitride layer. This variation was addressed and parameter (cage hole size) was tested after matrix

to produce a completely uniform sample temperature. This temperature variation was found to have insignificant effect on the rest of the sample materials.

For the most successful example having clear nitride-matrix interfaces, 316L nitride layer shows pressure has an insignificant effect on the nitride layer and the time and temperature are the dominate parameters. As expected from literature reviews, nitriding 316L above 430 °C produces CrN precipitates producing a hardness increases from 2 to 12 GPa. No delamination problems were observed. The 316L nitride layer hardness for 400 °C increased to 5 GPa. Scratch testing of 316L by Oklahoma State University Ultraprecision Surfaces Group show an increase resistance to scratching.

An appropriate selection of cage materials is critical. For Fe-based steels, an unused stainless steel cage is ideal to avoid Fe contamination. For Zr-based Zircaloy, a Zr cage is needed. As an example, Fig. 3.9 shows SEM images of the nitrided Zircaloy-4 using a 316 cage. On top of the expected nitride layer, there were islands in the center of the sample surface with typical size about 30 µm. EDS analysis was performed on both islands and the flat surfaces of nitrided samples. The islands were rich in Fe and C. On the other hand, the flat surfaces are rich in Zr and N, as expected from a nitride layer. The contamination was caused by the significant sputtering of Fe atoms from the cage and the deposition of the sputtered atoms on the Zircaloy surface.

In order to avoid contamination from the cage materials, we optimize the voltage bias to maximize the plasma density, in order to dynamically sputter the deposited materials. Furthermore, self-materials were used as cage materials to further reduce contamination. Figure 3.10 shows SEM images of the nitrided Zircaloy-4, which is smooth without any island formation on the surface. The presence of N atoms is both confirmed by both EDS and SIMS analysis. Figure 3.11 shows SIMS N profiles,

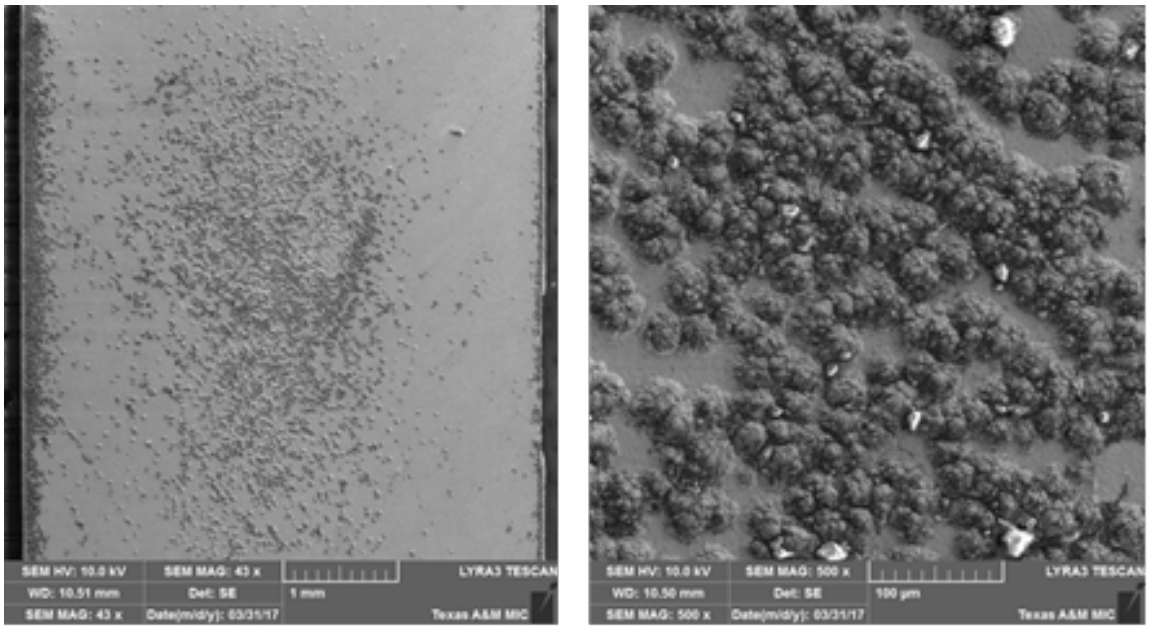

Figure 3.9: SEM surface images of Zircaloy-4 nitrided using 316L cage. Nitriding was performed at cage bias potential for 24 hours at 600 °C.

superimposed with SEM image of the crater after SIMS analysis. The SIMS analysis beam is scanned over the cross-section of the nitrided sample. Due to the difference of mechanical properties in nitrided layers and deep Zircaloy-4 regions, sputtering yields are different, leading to a distinctive contrast of the nitride layer which is smooth and relative darker. The curves of Fig. 3.11 are N counts as a function of the distance from the surface.

3.2.1 Electrical Insulators

Efforts to reproduce the experiment used by Alves et al. resulted in inconsistent nitridation results [17]. Figure 3.12 demonstrates variation of surface deposition with repeated experiments. The main issue was that the alumina isolating disc and other ceramic insulators, though surface deposition was also attributed to changes of the cathodic cage due to nitridation. As one of the mechanisms for nitrogen trans-

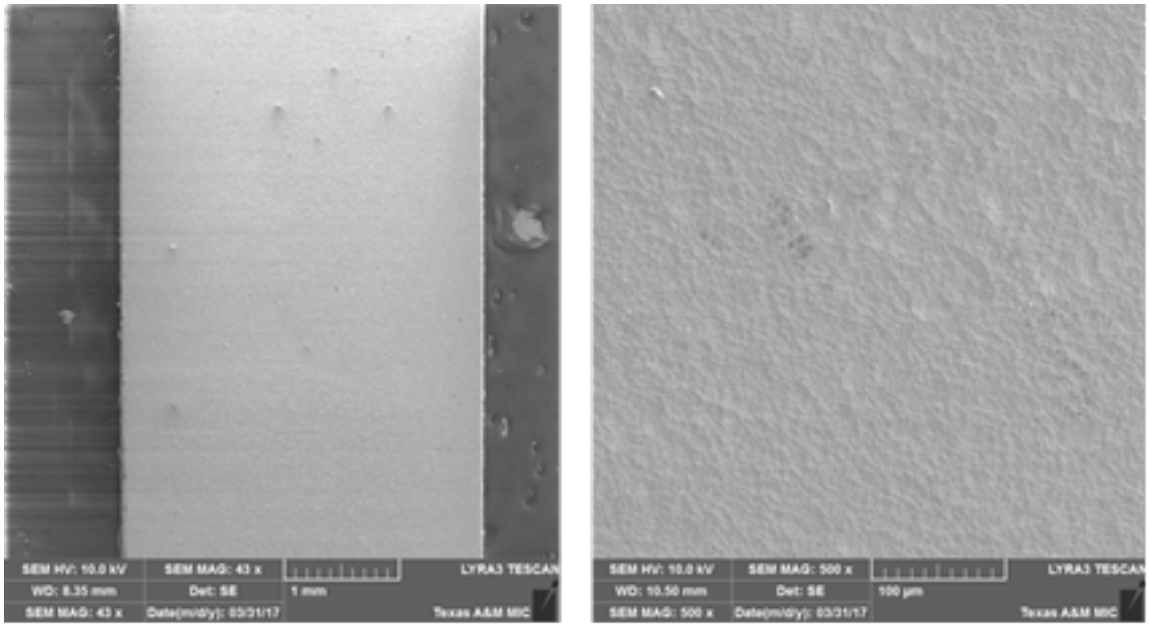

Figure 3.10: SEM image of a clean Zircaloy-4 surface after nitridation.

port is the sputter and deposition of the cathode, the metallic ions would be drawn to the insulators. The insulators would become coated with a conductive metallic layer resulting in electrical shorting, sever arcing, and inconsistent nitridation of samples. The alumina isolation disc that the samples were placed was meant to keep the samples at a floating biased. After about an hour of nitriding at 400 °C, a clean isolation disc would become conductive due to metallic deposition. As the thermocouple was attached to a dummy sample, voltage on the thermocouple would increase with nitriding time and eventually reach the cathode voltage. This indicated that the samples had a variable bias that changed with nitriding time which also affect temperature. With the cathode voltage applied to the thermocouple, arcing to the thermocouple and plasma formation on thermocouple wiring inside the chamber would occur which also resulted in inaccurate temperature measurements. The insulating standoff would also become conductive. As nitriding time progressed, the

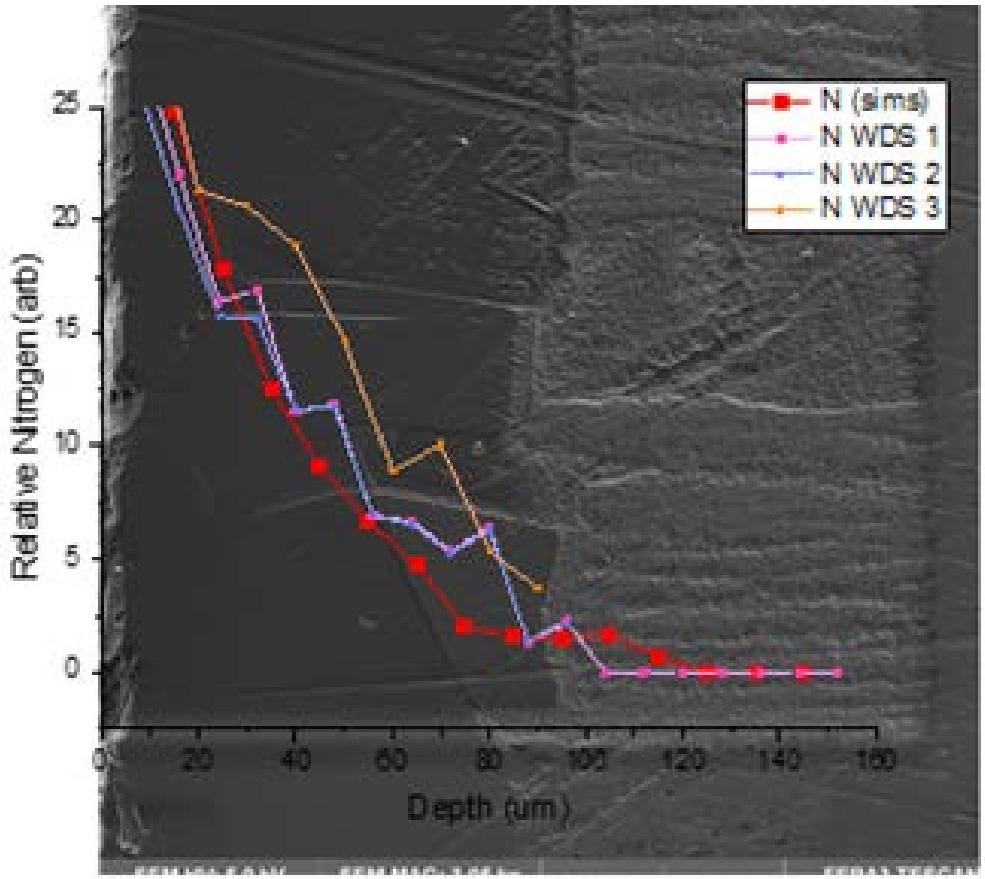

Figure 3.11: SIMS N depth profiles as a function of distance from the surface. The profiles are superimposed with a SEM image of the crater where SIMS analysis is scanned over.

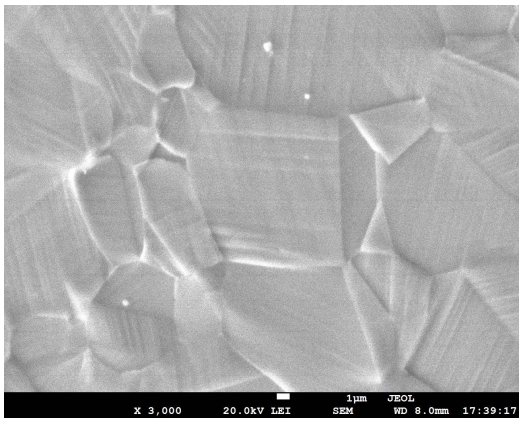

(a) 454 °C 1HR

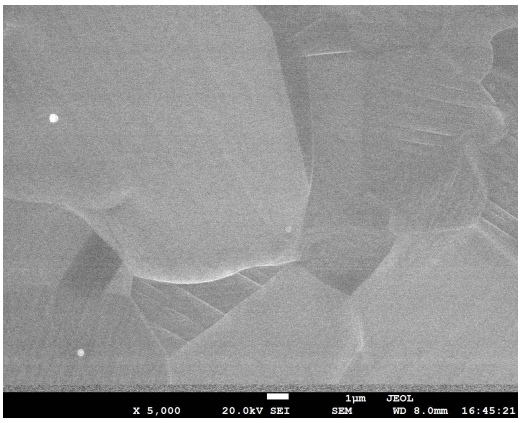

(b) 400 °C 1HR

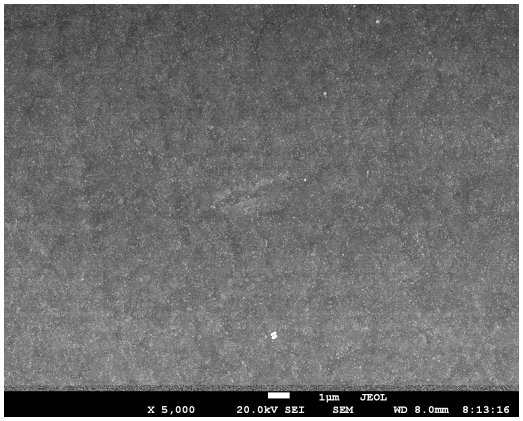

(c) 454 °C 1HR

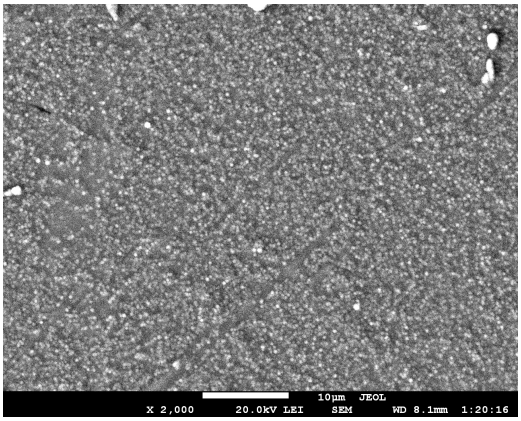

(d) 400 °C 1HR

Figure 3.12: SEM surface images of inconsistent nitridation results.

plasma on the cage would start to form on the insulating standoffs near the cathode which lead to shorting and arcing to the insulating stands.

The solution to the loss insulating properties was to design plasma shields. Steel shield were fabricated with a gap that had a depth to width ratio. Ceramic cylindrical standoffs 1/2 inch in length and a 3/8 inch diameter were fitted with plasma shields as in Fig. 3.3a.

3.2.2 Cathodic Cage

3.2.2.1 Material

The choice of cage material should be chosen based on the sample material. For a floating sample, the sputter and deposition nitrogen transport mechanism results in some cage ions sputtered into the workpieces. The nitrides that are formed from the the cage should be taken into account. For example, using a titanium cage to nitride steel. The small amount of titanium may deposit on the surface of the sample. Nitrogen diffusion in titanium is very slow compared to nitrogen diffusion in steels. This will limit the diffusion rate of the nitrided steel resulting in thinner nitride layers, though the small amount of titanium may benefit the near surface corrosion resistance. It is recommended to be cognitive of how the cage material's nitrogen diffusion rate affects the nitride layer's growth rate. Though the sputter rate of titanium was noted to be significantly less that than of the stainless steel cage.

The changes to the cathodic cage during the nitriding process is also of concern, especially if the cage is not welded or is made of thinner material. As the temperature and nitriding hours increase, the cage's electrical conductivity will be affected. The nitriding cage fabricated from perforated 316L with a thickness of 1 mm was eventually noticed to have been completely nitrided through to the core. The key reason the cage base was switch from stainless steel to titanium is the electrical conductivity of TiN is increased compared to titanium [120]. In comparison, the electrical conductivity of iron nitride films is significantly impaired compared to pure iron [121]. As the cathodic cage voltage is applied to the cage side and top via electrical contact, the increased electrical resistance decreases the voltage potential of the two components in comparison to the base.

3.2.2.2 Fabrication

Due to the changes of the electrical properties of stainless steel cages during the nitriding process, it is recommended that the cage top be welded to the cage side. In addition, a thicker cage is recommended if the cage will be used multiple times as the internal material conductivity will take longer to be affected by surface nitridation. As the nitride layer thickness increases, the conductivity of the cage decreases. This can lower the voltage that reaches the cage surface and becomes more significant at higher currents. The cage is placed on the stage base and the cage top is placed on the cage side. The electrical connection is not typically welded. As the nitride layer increases, this will increase the electrical resistance between the three components. The effects of the nitride layer of the cage and the temperature of the cage has not been experimentally investigated. The side and top cage can be welded together to prevent a voltage loss between them. Prior to use, the nitride layer on the bottom of the cage that connects to the base should be ground to remove nitride layer. Another option to maintain good electrical conductivity to the cage is to design a connection that is shielded from the plasma, though gas nitriding may still occur.

3.2.2.3 Stainless Steel Cages

For the 304 stainless steel 1/4 inch perforated cage, the temperature and degree of nitriding that the cage had undergone seems to affect the nitriding. If the cage had consistently been used above the transition temperature of 430 °C, the amount of sputter deposition or sputter ions from the cage was observed to increase. The thickness of the cage material also appeared to contribute to sputter deposition and experimental consistency. For nitriding experiments, it is recommended to start with a newly fabricated cage for each experiment. This is more important for low temperature experiments if the nitride layer on the stainless steel cage has started

to decompose from expanded austenite.

3.2.3 Gas

The gas use chosen for plasma nitriding was ultra high purity (UHP) N_2/H_2 (90/10) gas based on previous work indicating that hydrogen assists with nitride layer formation [3]. Pure nitrogen was tested but it was found that hydrogen addition greatly assisted in oxygen removal from the chamber and nitrided samples. Though the hydrogen content resulted in variation of gas composition during the nitriding process.

One of the notable effects of using a N_2/H_2 mixture was that the plasma electrical properties would change with time. This was indicated by the general trend of the voltage, current, and pressure changes from the start of nitriding to an equilibrium condition. Equilibrium condition were usually observed after 30 to 60 minutes which could suggests that the gasses are undergoing a chemical change during the nitriding process. For higher temperatures, the formation of ammonia could clearly be observed upon opening the chamber due to the distinct smell. Increasing the gas flow rate may assist with maintaining the initial gas mixture but is overall limited to the rate that the gas can be pumped out of the chamber.

3.2.4 Gas Flow Rate

The gas flow rate may be able to assist with minimizing the rate at which the sputter deposition occurs on the samples. By increasing the gas flow rate the sputter ions are also pumped away and therefore minimizing the total number of sputtered ions in the chamber. Though, as the gas flow rate is increased, the gas wastage or consumption is increased also. This may be an concern for industrialization of the process. Another hypothesis for reducing unwanted sputter deposition and changes in gas composition or gas non-uniformity would be to add a recirculating pump. A

recirculating pump would increase the gas mixing and could allow for removal of the sputter ions. The degree of sputter ion removal can be increased with various methods. One method may be to add fine mesh screens that the recirculation gas would pass through, maybe adding a mix of potentials to the screens to attract any ions. Increasing the surface area that the recirculated gas is exposed to may also assist in removal of the neutral particles and ions. If a recirculation flow is used, it would be an optimal location to connect a gas analysis system. Measuring the gas composition for optimal nitriding would minimize gas wastage by only adding the gases needed, possibly eliminating a discharge once the various other contaminates are removed after surface cleaning.

4. EXPERIMENTAL PROCEDURES

4.1 Sample Preparation

4.1.1 Sample Polishing

Samples were cut into approximately 5 by 8 by 1 mm coupons. Samples were adhered to a flat aluminum polishing block with crystal bond and mechanically ground with 180, 400, 600, 800, and 1200 grit SiC sandpaper with flowing water to level the back of the samples to the same thickness. Next, the back of each sample was inscribed with a unique sample identification number (SIDN). Samples were removed from polishing block, cleaned with acetone, and adhered to the block again with the polished labeled side to the block. The exposed unpolished side of the samples were then mechanically ground with 180 through 2400 grit SiC sandpaper with flowing water. Then the samples were polished with 1 um colloidal alumina followed by 40 nm colloidal silica on a nap cloth pad. Next the samples were removed from the polishing block and ultrasonically cleaned with acetone.

4.1.2 Cross-sectional Sample Preparation

For cross-section analysis, nitrided samples were first ground with 400 grit SiC sandpaper to remove approximately 1 mm of material from the edge of the sample to allow inspection of nitride layer representative of one dimensional diffusion. The samples were then cross-sectionally lapped with 30, 15, 3, and 0.3 µm diamond lapping paper prior to cross-section mechanical testing and SEM analysis. Samples were ground and lapped in the direction into or perpendicular to the nitride layer to minimize damage to the nitride layer. HT-9, T91, and 316L samples were acid etched if needed, typically with 5% nital solution or marbles reagent, for nitride layer evalu-

ation using SEM. Acid etchant was applied using a cotton swab for various duration and cleaned using recommended procedures from ASM HANDBOOK ETCHANT TABLE [122].

4.2 Cathodic Cage Plasma Nitriding Surface Treatment

The samples were placed on the sample holder and temperature was measured via K-type thermocouple. The thermocouple was mechanically attached to the sample holder with a set screw. The movable ground plate was moved to 1 cm from top of cage to minimize arcing when igniting plasma. The chamber was then evacuated below 100 mTorr, as measured by a convection pressure gauge, and filled with ultra high purity (UHP) N_2/H_2 (90/10) gas to greater 10 Torr. This evacuation and fill was repeated three times before setting pressure to 400 mTorr. Cage voltage was increased to ignite the plasma. After the cage surface was conditioned and the plasma was in steady state, the ground plate was raised to 6 cm above the cage, pressure was increased to target pressure, gas flow set to 60 cm^3/min, and cage voltage increased such that current was 150 mA. These parameters were maintained for 30 minutes to remove the oxide layer from samples and maintain the temperature below 200 °C to maintain nitrogen diffusion negligible. After conditioning, the cage voltage and current were controlled to maintain the temperature of the samples. Samples were then nitrided at target temperature, pressure and duration. After nitriding, the voltage was decreased while maintaining plasma until the samples were cooled to less than 200 °C, where typical cooldown rate was 40 °C/min. Then the voltage was set to zero and samples cooled to less than 50 °C under flowing N_2/H_2 gas before the chamber was vented to atmosphere.

4.3 Characterization Techniques

4.3.1 Nanoindentation Testing

The hardness and reduced modulus mechanical properties were measured with a Hysitron TI 950 Triboindenter. Prior to and after performing indentations, the calibration of the transducers were verified on fused quartz. Surface indentations were performed using standard load and high load transducers with diamond Berkovich probes. A load controlled quasi-static partial-unload load function was used to measure surface hardness and reduced modulus as a function of contact depth. Figure 4.1 is an example of the standard load controlled quasi-static partial-unload load function and settings provided with the Hysitron TI 950 Triboindenter software. The number of partial-unload and magnitude of maximum force applied were adjusted as based on sample properties. Cross-sectional nanoindentation was performed with a diamond Berkovich probe and a standard load transducer. A trapezoidal load function was used where load and unload times were 5 seconds, and the hold time at the peak force was 2 seconds. Cross-sectional nanoindentation was performed on the polished cross-section of the nitrided sample at various distances away from the surface edge. The distances represent the depth beneath the nitrided surface.

!!!!!!add notes already written on variation of load for xsec!!!!!!

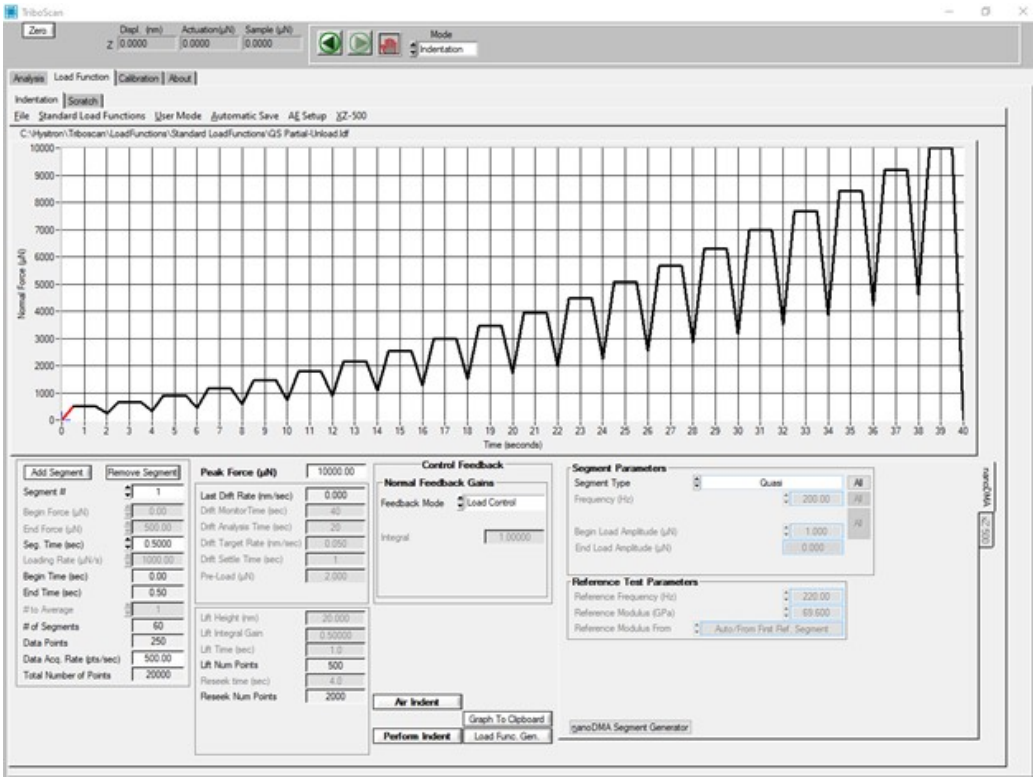

Figure 4.1: Standard load controlled quasi-static partial-unload load function and setting used as basis surface indentations.

4.3.2 SEM and EDS

The following scanning electron microscopes (SEM) were used to analyze the nitrogen modified layers of samples based on availability and purpose:

- JEOL JSM-7500F field emission scanning electron microscope (FE-SEM) with EDS
- Tescan LYRA-3 Model GMH Focused Ion Beam Microscope with EDS
- Tescan FERA-3 Model GMH Focused Ion Beam Microscope

For visual evaluation of samples, an electron beam energy of 5 keV was used with a nominal sample distance of 5 mm. The secondary electron detector was used to

obtain images for visual analysis. Electron dispersive spectroscopy (EDS) was performed on sample cross-sections to analyze nitrogen concentrations as a function of depth. For EDS, a 10 keV electron beam energy was used with the sample distance at 9 mm. Oxford Instruments Inca and AZtec EDS software were used for elemental analysis of samples. For nitrided Zircaloy-4 sample analysis, EDS software was calibrated using high purity ZrN microspheres with a 10 and 20 keV electron beam at 9 mm.

4.3.3 FIB and TEM

A Tescan LYRA-3 Model GMH Focused Ion Beam Microscope was used to prepare TEM specimens by using 5-30 keV Ga beam. The 30 keV Ga beam is first used for cutting and lift-out, followed by 5 keV Ga beam with a weaker beam current for the final stage of specimen thinning to a thickness of ∼100 nm. A FEI TECNAI G2 F20 ST FE-TEM was used to characterize effects of nitridation on microstructural changes of fuel cladding materials. TEM characterization was conducted using an operating voltage of 200 kV. Localized diffraction pattern analysis was performed to identify phases.

4.4 Nitriding Diffusion Kinetics

The nitrogen layer thicknesses were measured using SEM, EDS, WDS and nanoindention. The effective nitrogen diffusion coefficients were then calculated using Fick's diffusion equation

$$L \approx \sqrt{D(T)t} \tag{4.1}$$

where L is the nitrogen layer thickness, $D(T)$ is the diffusion coefficient at temperature T, and t is the nitridation time. The diffusion coefficients were then grouped by

temperatures. For temperatures with only a single nitriding duration, the diffusion coefficients were averaged and plotted with error bars and denoted as "single time". The error bars included the standard deviation of the averaged diffusion coefficients and a temperature error of 10 °C. For nitrided samples with more than 1 nitriding duration at the same temperature, EQN 4.1 was linearized as follows,

$$L^2 = D(T) * t \tag{4.2}$$

and $D(T)$ was calculated using OriginLab software fitting function. The linearized Fick's diffusion equation fittings were then plotted with error bars that represented the standard deviation of diffusion coefficients. It should be noted that the use of this linearized fitting method does not take into account possible non-linearity as nitriding duration approaches zero. These calculated diffusion coefficients were plotted with error bars, labeled as "Time Averaged". The error bars include the error calculated from OriginLab software, which uses a Linear Least Squares (LLS) method, and a 10 °C temperature uncertainty. The $D(T)$ values were then fitted using the Arrhenius equation,

$$D(T) = D_0 * e^{(\frac{-Q}{R*T})} \tag{4.3}$$

where D_0 is the maximal diffusion coefficient, also called the pre-exponential factor, in cm^2/sec, Q is the activation energy in units of eV/atom, R is the gas constant, 8.617333262E-5 eV/(K-atom), and T is the temperature in Kelvin. D_0 and Q values and uncertainty were calculated using OriginLab software fitting function.

4.5 Corrosion Testing

4.5.1 Potentiodynamic Polarization Measurements

A potentiostat designed and fabricated in-lab was used for potentiodynamic polarization measurements. Figure 4.2 shows the experimental setup (image and the schematics). ASTM G3 and G5 procedures were used as a general guideline for potentiodynamic polarization corrosion testing [8, 6]. Deionized water was used to mix a 3.5 wt% NaCl electrolyte. 120mL of electrolyte was measured and heated from room temperature to 30 $\pm$1 °C. Next, the electrolyte oxygen level was reduced by bubbling flowing Argon at 150 cm^3/min for 30 minutes through the electrolyte. Nitrided samples were corrosion tested without further preparation after nitriding. Unnitrided reference samples were mechanically ground using 400, then 600 grit SiC sandpapers and ultrasonically cleaned in methanol within approximately 15 minutes prior to sample immersion. The samples were placed in a Teflon holder with a 6.2 mm^2 surface area exposed to the electrolyte. The working electrode (sample holder), reference electrode, collector electrode, and pH meter were immersed in the electrolyte after the degassing was completed. A glassy carbon collector electrode and a 3.5M Calomel reference electrode reference electrode were used. For redundancy, 0.6M Ag/AgCl reference electrode was also immersed in electrolyte in conjunction with the 3.5M Calomel reference electrode but was not connected to the potentiostat circuit. Potential difference between the reference electrodes, measured with a Fluke multimeter before and after scan, was typically 2 mV. The pH, temperature, and open circuit potential (OCP) were measured immediately after the samples were immersed and within 10 minutes prior to starting the test. One hour after the samples were immersed in the electrolyte, the potentiodynamic scan was started at a set potential below the measured OCP, typically 100 mV, and increased at a rate of 0.6

V/hr. The scan was stopped at the maximum current of the potentiostat or at 1.6 Volts.

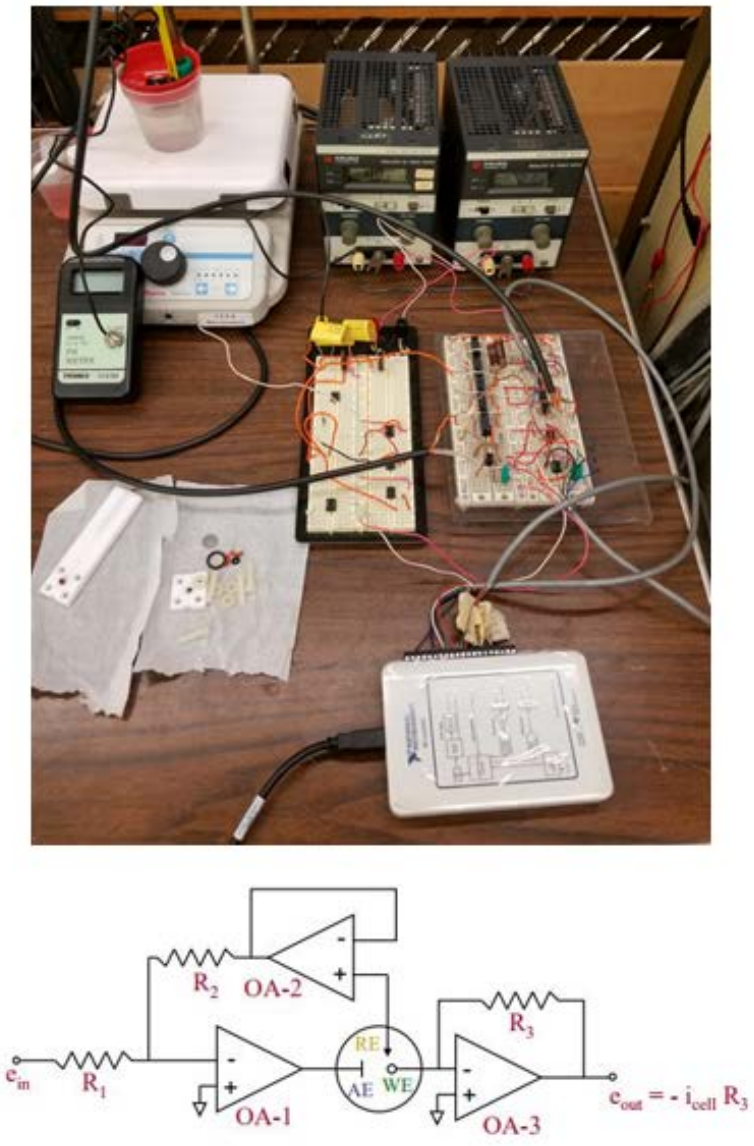

Figure 4.2: Potentiodynamic measurement experimental setups following ASTM G3 and G5 procedure.

4.5.1.1 Corrosion Rate Analysis

Corrosion rates were calculated using pre-Tafel region polarization fitting method. Analysis was performed using OriginLab software. First, E_{corr} was set to the applied voltage associated with the measured minimum of i_{app}. Using EQN. 2.12 with OriginLab non-linear fitting function, the pre-Tafel current density and potential were fitted to calculate β_a, β_c and R_p. An example of this step using a Zircaloy-4 reference sample is shown in Fig. 4.3. Next, i_{corr} was calculated using EQN. 2.10 and EQN. 2.11. Corrosion rates were then calculated using EQN 2.7 and EQN. 2.13 per ASTM G102 [82].

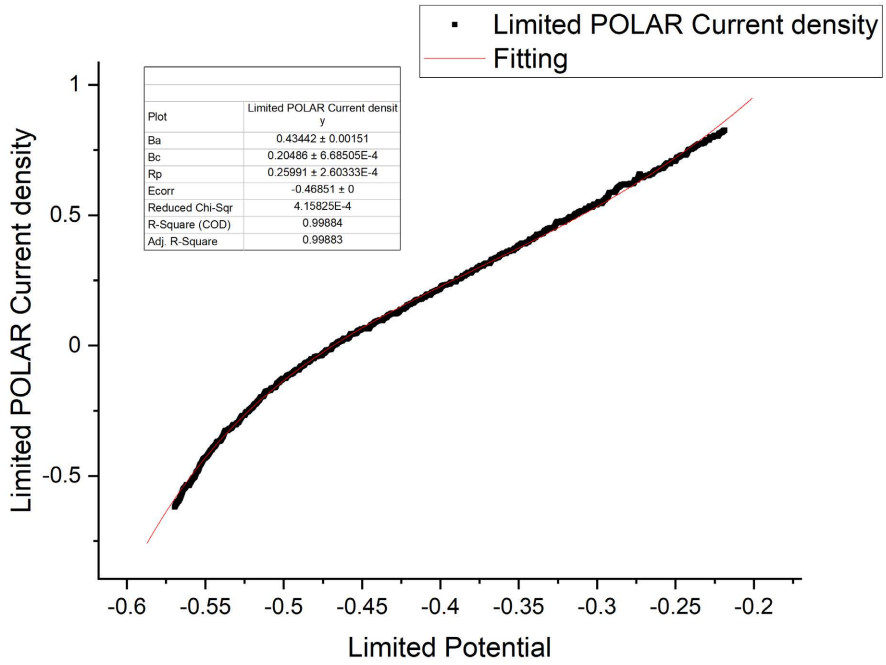

Figure 4.3: Example of a pre-Tafel corrosion fitting of Zircaloy-4 reference sample.

11	12	13	14	15
Control Sample	Nitride coated 600 °C/2h	Nitride coated 700 °C/2h	Nitride coated 800 °C/2h	Nitride coated 800 °C/10h

Table 4.1: Condition of nitrided samples exposed to FLiNaK corrosion environment.

4.5.2 Corrosion Testing in Molten Salt

Nitride coated Hastelloy-N samples of different coating treatments were corroded in liquid FLiNaK at 700 °C for 400 hours. The corrosion testing was conducted inside of an argon-atmosphere glove box. During the corrosion experiment, the oxygen and moisture level were kept bellow 1ppm each. 80g of FLiNaK was used for the corrosion testing. The individual salt components were purchased from Alfa-Aesar with purity level higher than 99.99%. Then the salt components were weighted and melted in a glassy-carbon crucible. The labeling information of the tested samples is summarized in Table 4.1.

Corrosion testing was conducted using nickel crucible to reduce the influence from the crucible materials. Hastelloy N samples were held from the top by Ni 200/201 rods. All the materials in contact with the salt were either pure Ni or the samples. During the testing, the nickel crucible was placed inside of a ceramic glassy carbon crucible. The assembly was placed inside of a furnace and the temperature monitored via a K-type thermocouple inserted from the top.

The testing began by melting the FLiNaK at 500 °C and then lowering the nickel crucible cover with the samples into the liquid salt. The testing ended by lifting out the nickel crucible cover with samples after 400 hours. Pictures of the testing facility and details are summarized in Fig 4.4.

After the corrosion testing, the samples were first cleaned by DI water to remove the salt attached on the surface. The samples were then cut by a low-speed saw

to expose the cross-section. Half of the samples were hot mounted by conductive Bakelite powder sand mechanically polished down to 0.06 µm silica grit to analyze the cross sections. The samples were then examined using SEM in backscattering mode (Phenom XL Desktop SEM).

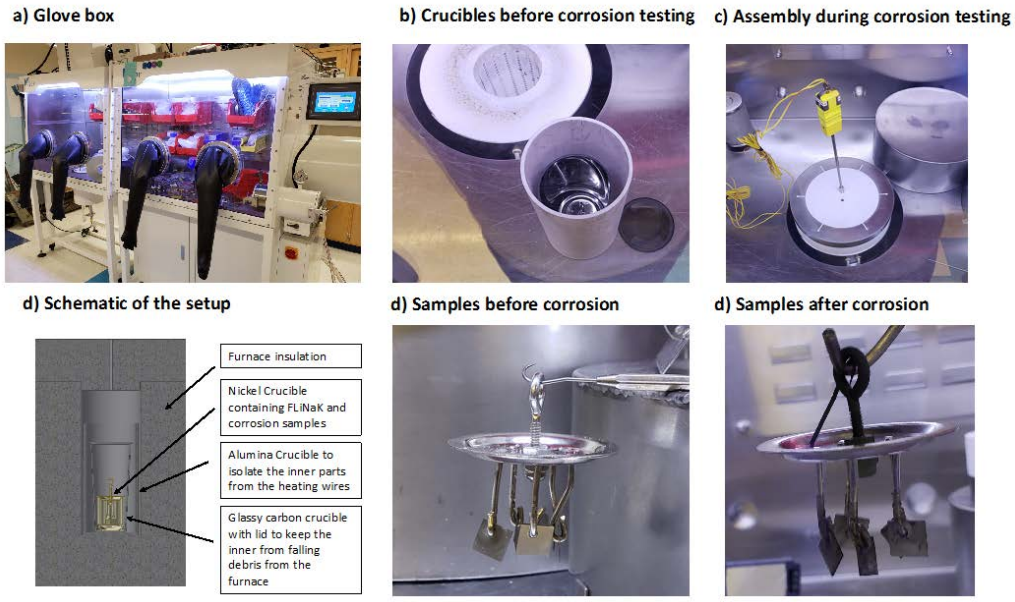

Figure 4.4: Experimental setup for molten salt corrosion testing and images of samples at different testing stages.

4.6 Ion Irradiation of Nitrided Stainless Steels

The irradiation response of nitrided steels was studied. Considering the importance of 316 stainless steels in both LWR and fast reactor applications, 316L was selected for this study. The study consists of three steps. Firstly, 316L is nitrided to form a surface nitride layer. Then the nitrided sample is cut and the newly created cross section is polished and irradiated by using 3.5 MeV Fe ions to 50 peak dpa at 600 °C. Next, focused ion beam is used to prepare lamellae specimens from different

locations of the cross section. Lastly, transmission electron microscopy is used to characterize void swelling.

4.7 Uranium Diffusion Couple

The interface interactions between U and Zircaloy-4 was studied. For a comparison study, both nitrided and untreated Zircaloy-4 were bonded with U in order to study whether nitridation can affect U diffusion. The study is important since nuclear fuel can swell and mechanically touch fuel cladding, hence inducing interface interactions. The nitriding processing can be designed to treat the inner surface of Zircaloy-4 cladding tubes.

The study consisted of three steps. In step 1, a Zircaloy-4 sample is nitrided by nitrogen plasma. In step 2, both an un-treated sample (as a control sample for comparison) and a nitrided sample are bonded with pure U (U238 of purity of 99.8%) to form a diffusion couple. In step 3, longtime annealing was performed to induce interface diffusion and reaction.

For a diffusion couple formed by mechanically bonding two polished metals, thermal annealing with sufficient thermal budget will drive atom diffusion cross the original interface and form interface compounds [123, 124]. For a bonded binary system at early stage of diffusion, the atom penetration is governed by Fick's law. When the thermal budget is high enough, the concentration profile evolves into step height distributions, with each step corresponding to an equilibrium phase predicted by the phase diagram. A diffusion couple can be formed at a pre-selected temperature and is quickly quenched to ambient temperature. Thus, the microstructures corresponding to a higher temperature in the phase diagram is preserved at a low temperature for characterization. In this way, temperature dependencies of phase diagrams can be systematically studied.

5. MECHANICAL PROPERTIES

As one of the primary reasons to perform surface nitriding is to improve surface hardness, hardness testing it is essential to evaluate the initiatives of surface nitriding. For hardness testing on materials with variable hardness and elastic modulus properties, the accuracy of the results can be affected by this variation as shown in Fig. 5.1 [16]. A common rule is that the indentation depth should be at most 10% of the homogeneous layer [125]. In other words, if the indentation contact depth is one micrometer then the hardness and elastic modulus should be constant for a depth of at least 10 micrometers. Another condition for accurate indentation measurements is low surface roughness relative to the contact depth of the indentation.

In this chapter the mechanical properties for nitrided 316L, T91, HT-9 and Zircaloy-4 obtained from indentation measurements are covered. As the plasma nitriding technique used for this record of study resulted in surface deposition on samples performed at floating potential, surface indentation performed perpendicular to the nitrided surface was not extensively studied. To measure the mechanical properties of the nitride layer, cross-sectional indentation was performed to allow accurate measurements of the nitrogen modified layer as a function of depth. As Zircaloy-4 nitriding was performed with cage bias potential on the samples, a set of surface indentation measurements were included.

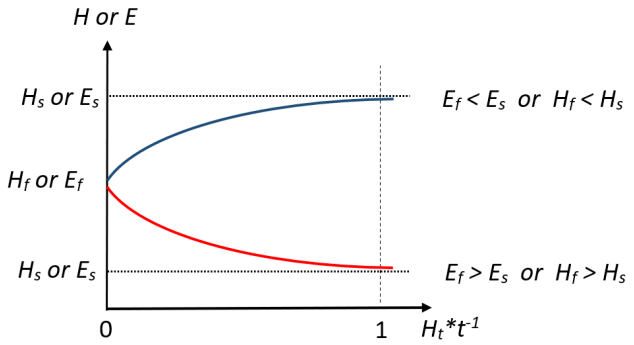

Figure 5.1: Typical evolution of Young's modulus and hardness for a coated specimen as a function of the normalized indentation depth. Adapted from [16].

5.1 316L Results and Discussion

In Fig. 5.2, cross-sectional SEM images of nitrided 316L after nanoindentation are shown where the left sides of the images are the samples surfaces and the right sides are the unaffected substrate. The samples were nitrided for 2 hours at temperatures of 511 and 596 °C. The shallower indents indicates increased hardness of the nitrogen modified layers. The nitrogen modified layers are visible in the SEM images by the smoother texture after cross-sectional polishing and the darker regions as compared with the un-nitrided 316L at the left of the images.

Figure 5.3 shows the nanoindentation cross-section measurements corresponding with the images in Fig. 5.2 with the exception of the sample nitrided at 454 °C which was not imaged. The open faced symbols are indentation measurements taken perpendicular the surface of the nitride layer. The surface measurements, with an average contact depth of 100 nm, indicates the very near surface has an increased hardness as compared with the underlying nitride layers. The corresponding reduced moduli are also higher than the cross-sectional nitrogen layer for the 454 and 511 °C samples. In Fig. 5.3a, all three nitrided samples the cross-sectional hardness has

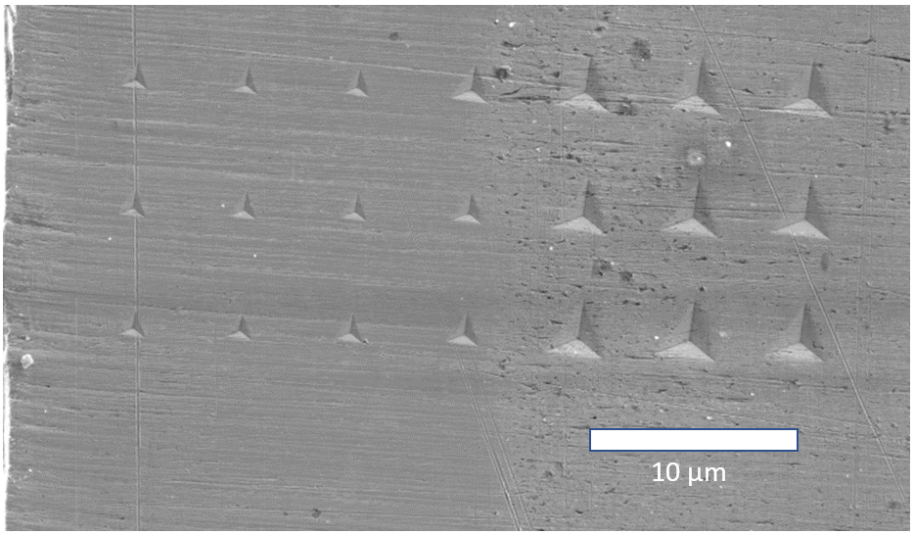

(a) 511 °C

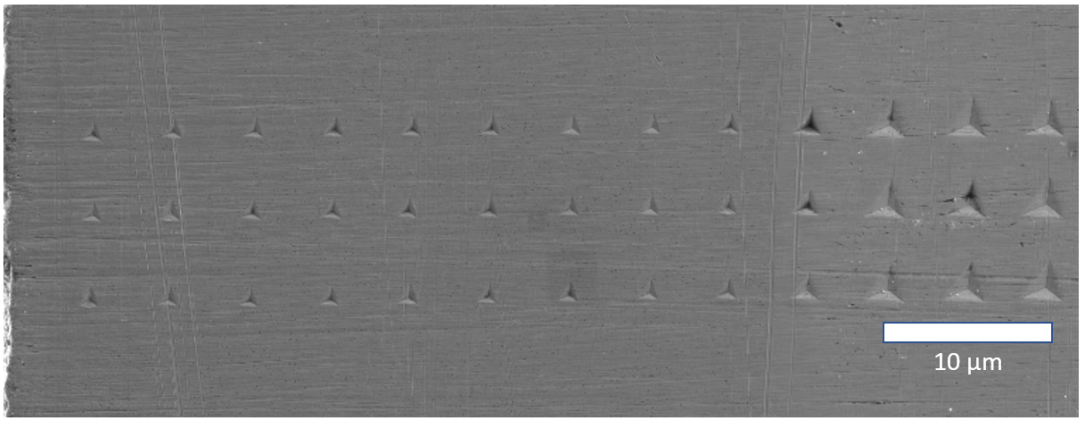

(b) 596 °C

Figure 5.2: SEM images of cross-section nanoindentation for 316L nitrided for 2 hours at temperatures of 511 and 596 °C.

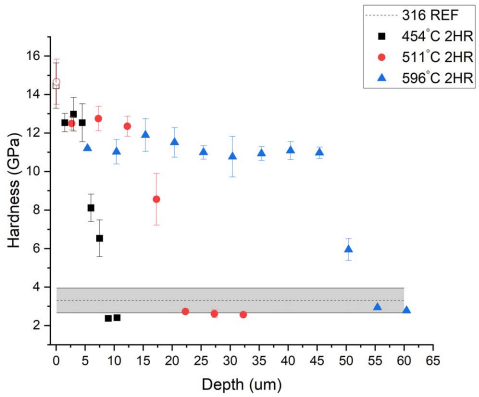

(a) Hardness

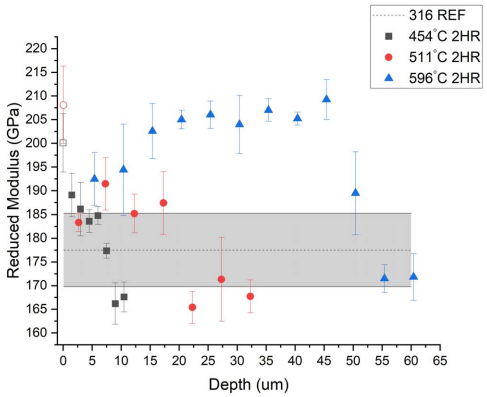

(b) Reduced Modulus

Figure 5.3: Nanoindentation cross-section measurements of 316L nitrided for 2 HR at 454, 511, and 596 °C.

plateau regions with hardness of 11-13 GPa. After the plateau regions, the hardness decrease within 5-10 µm to substrate values of 2-3 GPa which are slightly lower than the measured reference sample values of 3.2 GPa. The disparity of hardness of the un-nitrided region of the nitrided 316L samples and the reference sample may be contributed to surface deformation of the reference samples as a result of sample polishing. The hardness plateau regions is related to nitrogen atomic concentration greater than approximately 17%, which is covered in more detail in the next chapter.

Figure 5.3b show the reduced moduli obtained from nanoindentation for 316L. The reference 316L reduced modulus was 177.5 ± 7.5 GPa. For nitrided samples at 454 and 511 °C, the nitrogen modified layer increased the reduced moduli from approximately 165 GPa to 187 GPa. The surface reduced moduli were 200 GPa and 208 GPa respectively. Differing from the 454 and 511 °C nitrided samples, the 316L nitrided at 596 °C reduced modulus was approximately 193 GPa at 5 and 10 µm and increased to 205 GPa throughout the rest of the nitride layer. The increase in may be due to induced strain from the nitrogen interstitials. At a higher temperature, the

increased thermal diffusion may have allowed for the first 10 µm to relax the induced compressive strain. For the nitrided samples, the measured moduli of the nitrogen free 316L was approximately 170 GPa, which is on the low end of the standard deviation of the reference sample. As with the hardness measurements, the slightly lower reduce moduli of the substrate of the 316L nitrided samples can be contributed to the surface deformation layer caused by mechanical polishing.

5.2 T91

5.2.1 T91 Results and Discussion

The cross-sectional SEM images of nitrided T91 after nanoindentation are shown in Fig. 5.4, where the left sides of the images are the samples surfaces and the right sides are the nitrogen free substrate material. The samples shown were nitrided for 2 hours at 454, 511, and 596 °C and 30 minutes at 681 °C. In the SEM images, the nitrogen saturated layers corresponding to the shallowest indents have visible grain boundaries that are not observed in the nitrogen free substrate and may be nitride precipitates. The measured hardnesses and reduced moduli of these indentations are shown in Fig. 5.5 with the addition of T91 surface reference measurements and cross-sectional measurements for samples nitrided at 454 and 681 °C for 30 minutes.

For all nitrided samples in Fig. 5.5a, nitriding improved surface hardness compared to the substrate and reference sample hardness of 3.8 ± 0.4 GPa. For T91 nitrided at 454 °C for 30 minutes, the peak hardness was only 7.6 GPa at 2 µm. This is due to the nitrogen modified layer not reaching saturated values due to an insufficient thermal budget. As can be seen for all the nitrided samples, the diffusion zone between equilibrium nitrogen content and substrate covers a depth of approximately 25 µm. The wider diffusion zone of T91 compared to 316L can be contributed to the higher nitrogen diffusivity of its ferrite structure as compared to austenite. Samples

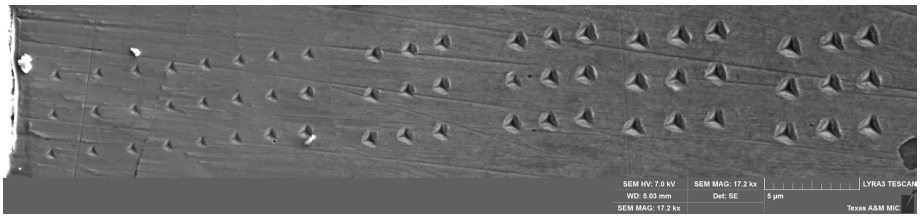

(a) 454 °C 2HR

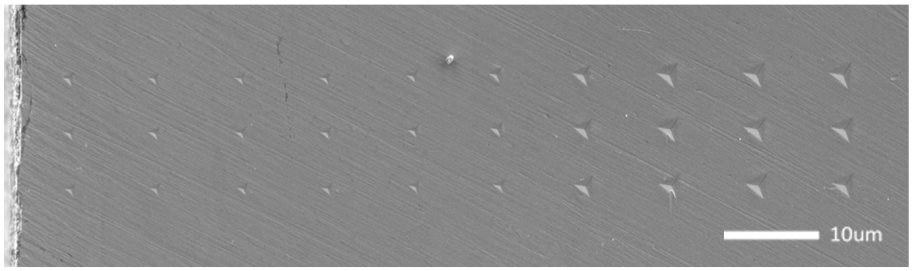

(b) 511 °C 2HR

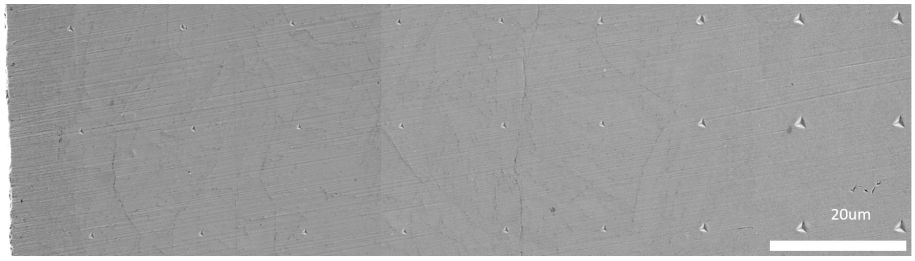

(c) 596 °C 2HR

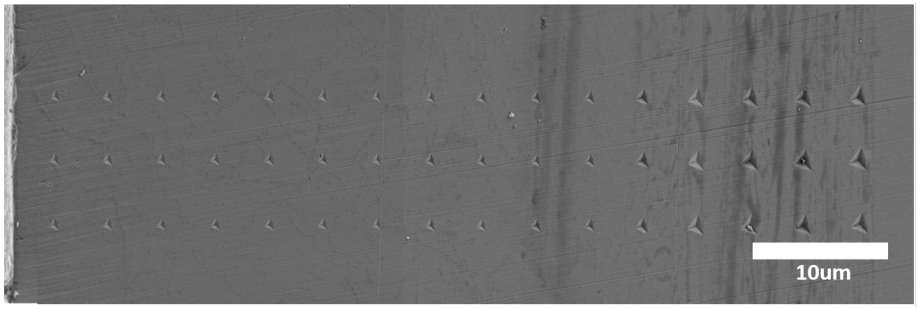

(d) 681 °C 30 MIN

Figure 5.4: Nanoindentation cross-section measurements of T91 nitrided for 2 hours at 454, 511, and 596 °C and 30 minutes at 681 °C.

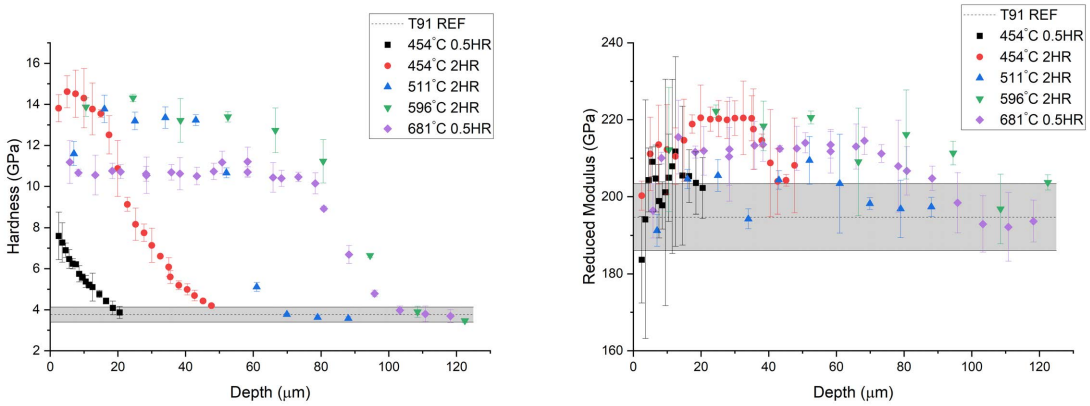

(a) Hardness (b) Reduced Modulus

Figure 5.5: Nanondentation cross-section measurements of T91.

nitrided for 2 hours at 454, 511, and 596 °C resulted in a fully developed nitrogen layer which achieved a typical hardness value of 14 GPa throughout the depth of the nitrogen saturated layer. At 681 °C, the nitrogen layer hardness decreases to approximately 11 GPa. The decrease in hardness may be contributed to thermal annealing of nitrogen induced compressive stresses at the higher nitriding temperature.

The T91 reference sample reduced modulus was measured to be 194.7 ± 8.7 GPa. On average, the developed nitrogen compound layer resulted in an increase of the reduced moduli. The reduced moduli of the nitrided T91 samples near the surface were lower than the deeper nitrogen compound layers.

5.3 HT9

5.3.1 HT9 Results and Discussion

Figure 5.6 shows SEM images of cross-section nanoindentation for HT-9 nitrided for 1 hour at temperatures of 454, 511, and 556 °C. The small circular objects in Fig. 5.6c are likely deposits resulting from the poor contact with the diamond lapping pad during cross-sectional polishing. On all three samples, triangular figures are

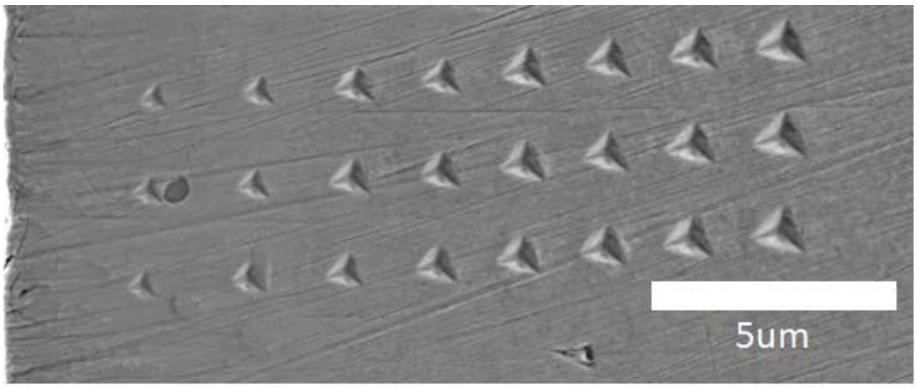

(a) 454 °C

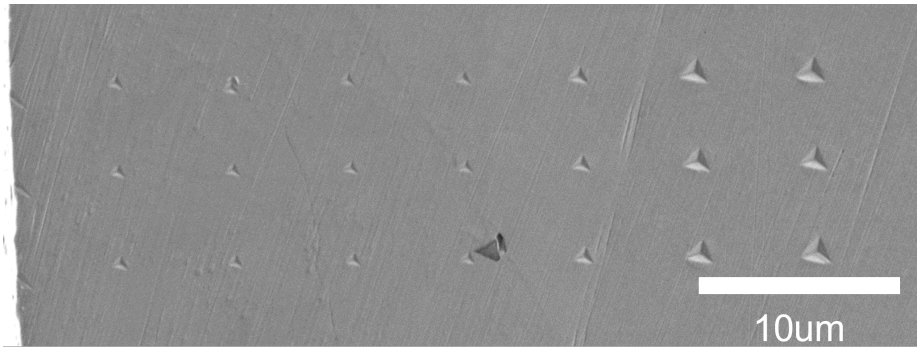

(b) 511 °C

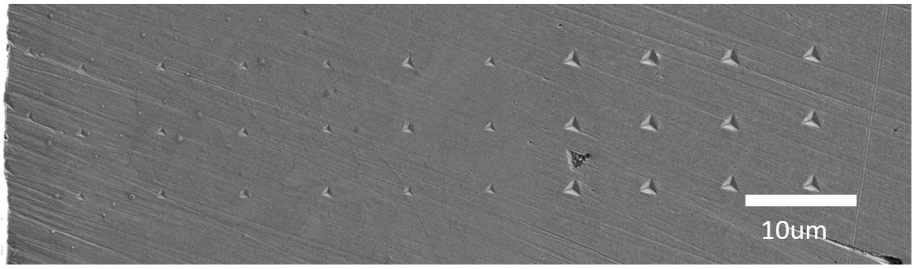

(c) 556 °C

Figure 5.6: SEM images of cross-section nanoindentation for HT-9 nitrided for 1 hour at temperatures of 454, 511, and 556 °C.

noted and may be precipitates inherent to the HT9 samples. The resulting hardness and reduced modulus measurements corresponding the SEM images are shown in Fig. 5.7. The developed nitrogen layer resulted in an increased hardness of 14-16 GPa as compared to the reference sample hardness of 4.6 ± 0.5 GPa. The diffusion zone for HT9 ranged from 15 µm for 454 °C to approximately 7 µm for the 556 °C sample. The reduce modulus of un-nitrided HT9 was measured to be 191.1 ± 8.5 GPa. At the lower nitriding temperature of 454 °C, the reduced modulus increased to approximately 215 GPa in the diffusion zone. This may be a result of surface deformation during cross-section sample preparation. Another explanation is that the increased modulus is a result of the stress induced from the nitrogen layer. The reduced moduli for the HT9 nitrided at 511 and 556 °C exhibited a lesser degree increase compared to the substrate which was lower than the reference sample. As with the other stainless steel nitriding, the near surface reduced modulus of the 556 °C sample decreased compared with the deeper compound layer. This decrease may also apply to the 511 °C sample but indentation were not performed close enough to the surface.

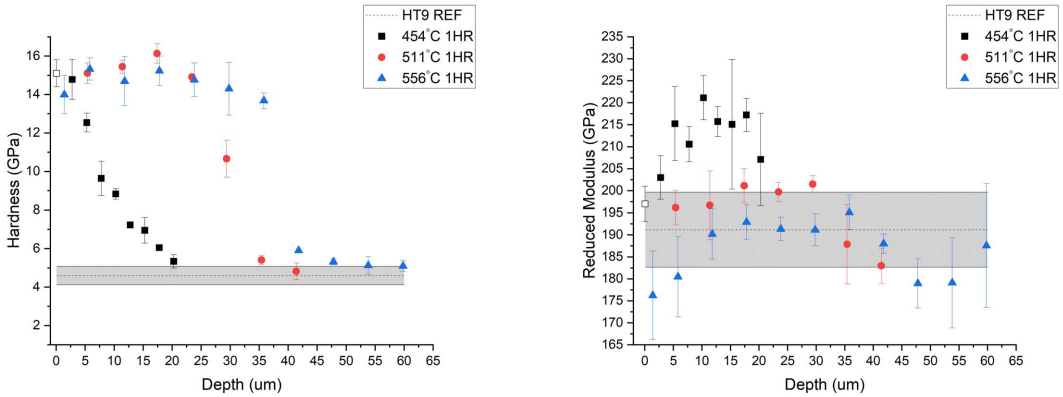

(a) Hardness (b) Reduced Modulus

Figure 5.7: Nanoindentation cross-section measurements of HT-9 nitrided for 1 hour at 454, 511, and 556 °C.

5.4 Zircaloy-4

Zircaloy-4 hardness is 1.67 to 2.69 GPa with the harder result being due to various forms of work hardening [126, 127, 128, 129, 130]. The elastic modulus is 99.3 GPa [126].

Nanoindentation tests were performed on both the surface and the cross section of nitrided Zircaloy-4. The cross sectional indentation was used to show hardness changes as a function of distance away from the surface.

The distance of the indentation spot can be well controlled and there is no limitation on the maximum distance. However, the cross sectional indentation approach is difficult to characterize the near surface nitride layer δ-phase of Zircaloy-4 due to its brittle nature and the indenter's spatial resolution. To solve this issue, the traditional surface indentation (perpendicular to the nitrided surface) was used to study the surface nitride layer. Due to its high hardness, traditional surface indentation approach is limited by its maximum force of the low load transducer. Hence,

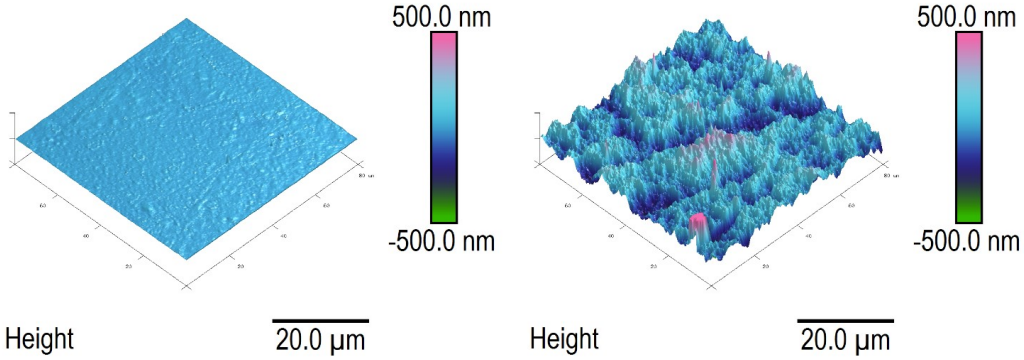

(a) Reference (b) Nitrided

Figure 5.8: AFM height images of Zircaloy-4 before and after nitriding 680 °C for 24 hours with sample bias at 640V. (scan size: 80 µm x 80 µm)

a combination of these two approaches overcome the issues and are supplementary to each other.

5.4.1 Zircaloy-4 Results and Discussion

Figures 5.8 and 5.9 shows surface topography of Zircaloy-4 before and after nitriding at 680 °C for 24 hours. The surface roughness increased significantly after nitriding. The peaks and valleys are due to the ion sputtering of the surface caused by the 640V sample bias that had the function of preventing sputter deposition associated with nitriding at floating potential. As the Zircaloy-4 surface is nitrided, some areas have preferential diffusion resulting in hardening and changes in electrical conductivity properties. This results in increased sputtering of softer or more electrically conductive areas, creating a relatively rough surface for nanoindentation purposes.

Figure 5.10 shows the Raman spectra of Zirconium and Zircaloy-4 before and after nitriding with two peaks around 220 and 500 cm-1, which were consistent with

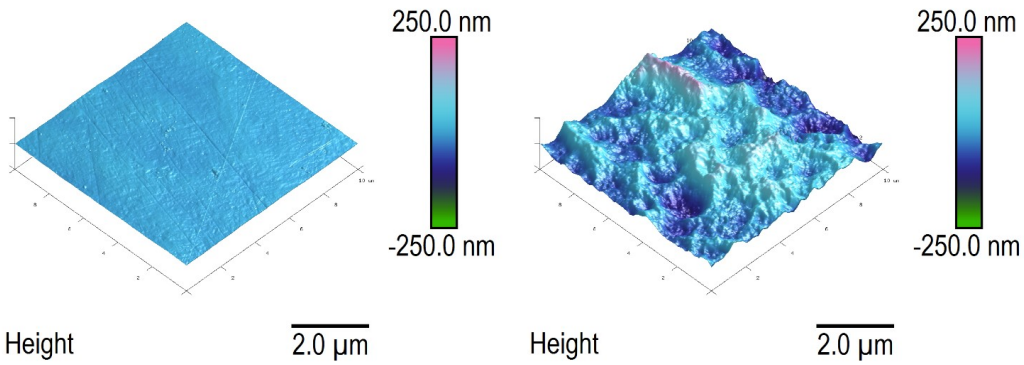

(a) Reference (b) Nitrided

Figure 5.9: AFM height images of Zircaloy-4 before and after nitriding 680 °C for 24 hours with sample bias at 640V. (scan size: 10 µm x 10 µm)

those reported in the literature and attributed to the formation of ZrN.

Due to the surface roughness of nitrided Zircaloy-4, the detailed procedure used for its surface measurements are covered here for clarity. To minimize error due to surface roughness of nitrided Zircaloy-4 samples, surface areas with low roughness were selected using scanning probe microscopy, as shown in Fig. 5.11a. The selected area was imaged again after performing indentations as illustrated in Fig. 5.11b. The average surface roughness R_a, of the indentation area was then measured using the Hysitron TI 950 Triboindenter software in the areas of indentations. R_a measurements were then averaged for the standard load and high load indentation areas. A load controlled quasi-static partial-unload load function was used to measure surface hardness and reduced modulus as a function of contact depth. The partial load indentation measurements were then grouped by the measured contact depths for standard and high load transducers, respectively. The hardness and reduced modulus measurements were then plotted as a function of contact depth.

Figure 5.12 shows surface hardness and reduced modulus of nitrided Zircaloy-4 at

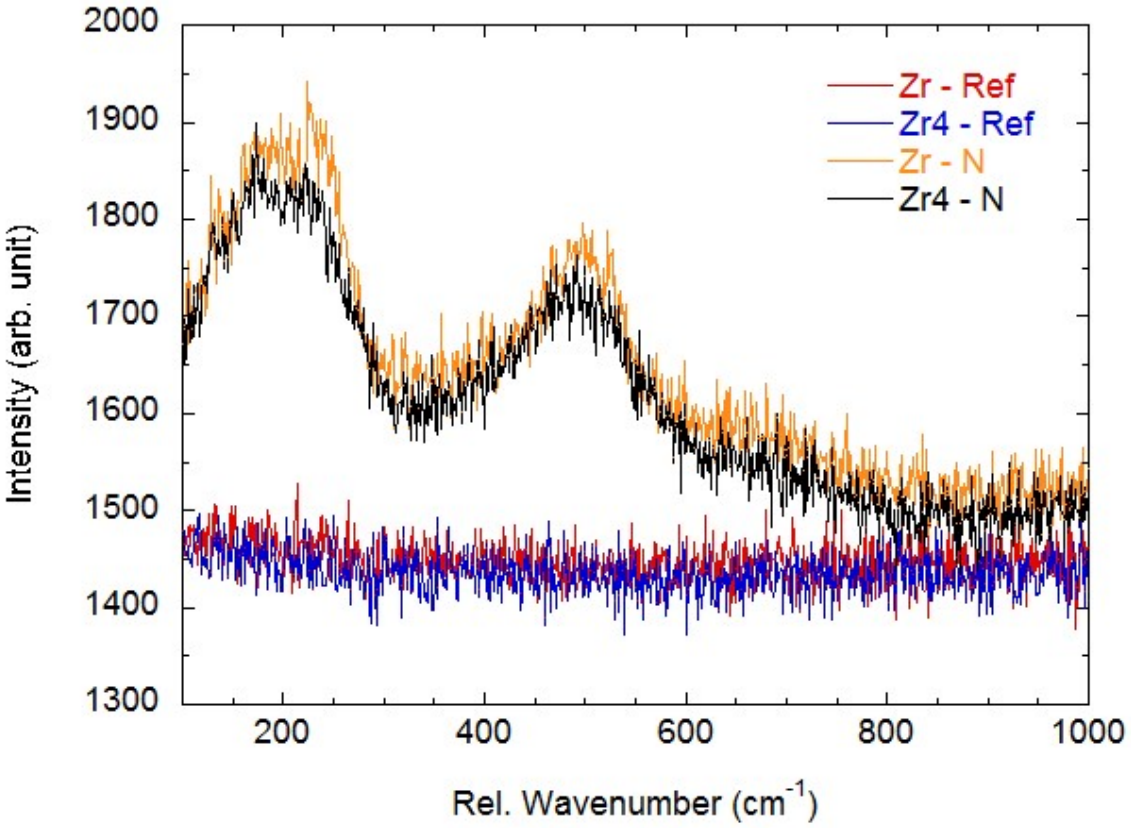

Figure 5.10: Raman spectra of Zirconium and Zircaloy-4 before and after nitriding at 680 °C for 24 hours.

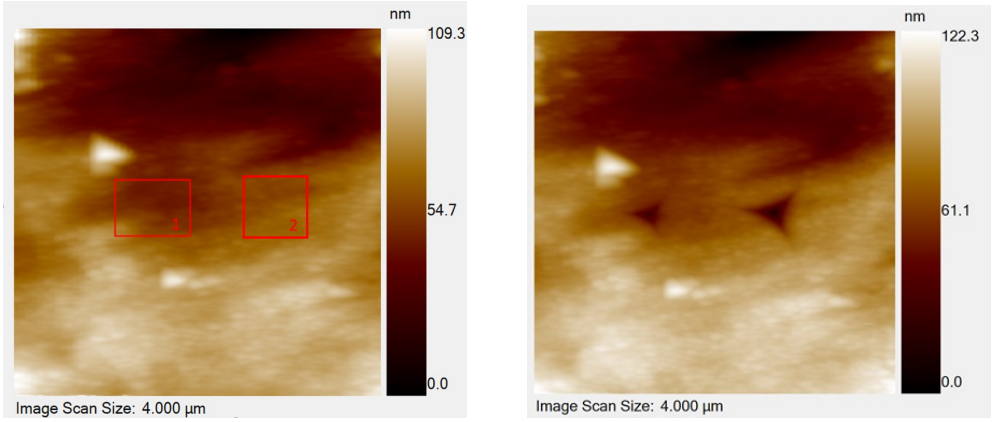

(a) before (b) after

Figure 5.11: Scanning probe microscopy images illustrating methodology used for surface indentation measurements. (**a**) Surface scan prior to indentation. (**b**) Surface scan after indentation. Box 1 and 2 labeled in (**a**) are the areas of measured roughness of the left and right indentations in (**b**) with R_a = 5.3 nm and 3.5 nm, respectively.

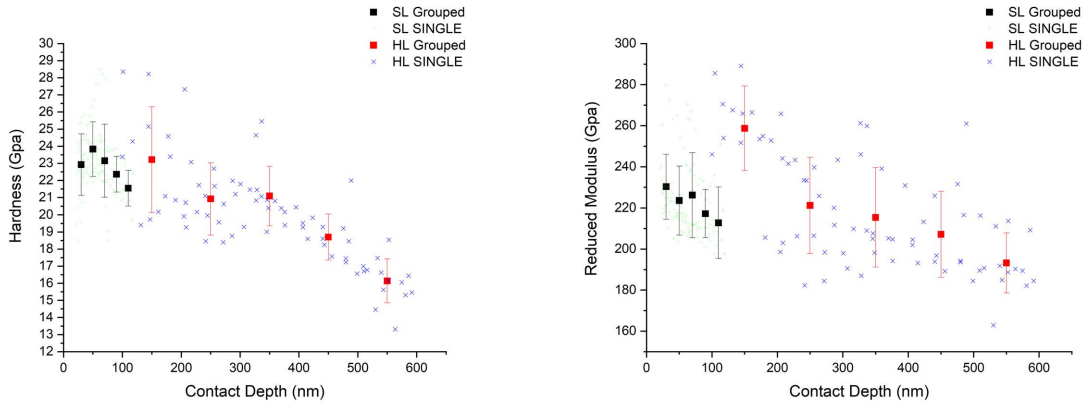

(a) Hardness (b) Reduced Modulus

Figure 5.12: Zircaloy-4 surface indentation measurements nitrided at 1010 °C for 24 hours. The standard and high load transducers measurements are denoted as SL and HL respectively.

1010 °C for 24 hours as a function of contact depth. The average roughness for the standard and high load transducer measurements were 6.1 and 14.3 nm, respectively. In Fig. 5.12a the single standard load measurements are shown in green ranging from 18 to 29 GPa with most of the measurements falling in the range around 23 GPa. After grouping the standard load measurements, the peak average hardness at a depth 50 nm was 24 GPa and decreased to approximately 21 GPa at 110 nm. The single high load measurements, show in blue, ranged from 19 to 29 around 100 nm and decreased to 13 to 19 GPa at 550 nm. The group averaged hardness at 150 nm was 23 GPa and decrease to 16 GPa at 550 nm. The reduce modulus of the nitrided surface in Fig. 5.12b ranged from 170 to 290 GPa for single measurements and 190 to 260 GPa after averaging. The hardness and reduced modulus within a contact depth of 350 nm are comparable to ZrN properties found in literature.

As surface indentation measurement of thin film with variable hardness and elastic moduli between the film and substrate, the general trend of the of the nitride

layer properties in Fig. 5.12 decreasing with contact depth are similar to the typical evolution shown in Fig. 5.1. The expected surface layers produced as a result of nitriding Zircaloy-4 at 1010 °C that may contribute to the surface measurements are ZrN, ZrN+α-$ZrN_{0.46}$ and α-$ZrN_{x<0.46}$, each layer having different hardness and elasticity. Another possible source of variation with depth is strain induced from phase changes and nitrogen diffusion. These sources of mechanical properties changing as a function of depth differs from deposition surface modification where the materials properties of the film and substrate are relatively constant. With known indentation properties of the film and substrate, the film thickness can be extracted based on changes of indentation data with contact depth. Due to the hardness and elastic modulus changing with depth combined with the ZrN layer thickness having not been included in this study, a precise measurement of the hardness, elastic modulus, and ZrN thickness cannot be drawn from the surface indentation measurements. While this indentation study did not investigate the material properties on the nanoscopic scale with indentation measurements in the near surface region, it can be concluded that a nitride layer with a hardness and reduced modulus greater than 20 GPa and 210 GPa, respectively was formed on Zircaloy-4 after nitridation. Also, drawing on the expected evolution of harder and more elastic thin films on substrates, the mechanical properties up to 350 nm shown in Fig. 5.12 extend significantly deeper into the Zircaloy-4 surface.

Figure 5.13 shows SEM images of cross-section nanoindentation for Zircaloy-4 nitrided for 24 hours at temperatures of 925 and 1010 °C. Differing from the standard 3 by x cross-sectional indentation arrays used throughout this study, the measurements performed on the 1010 °C sample was performed with only 2 indentations for each depth with relatively close spacing. As these measurements were some of the first cross-sectional indentation using this technique, the array spacings parallel to the

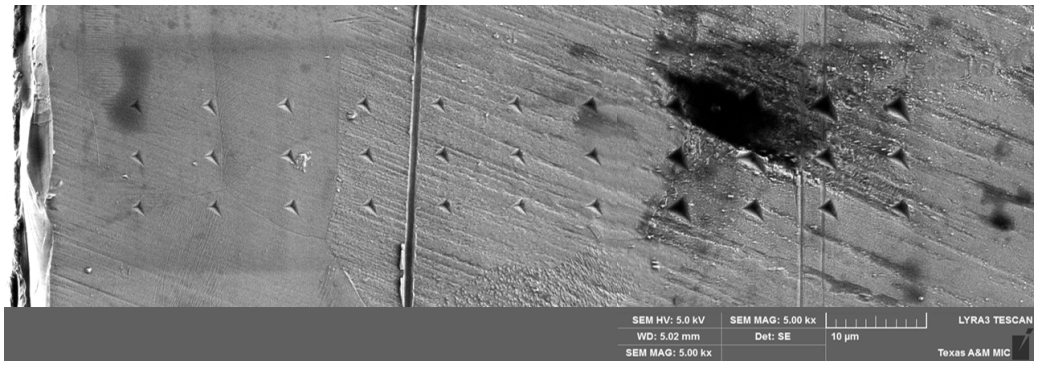

(a) 925 °C

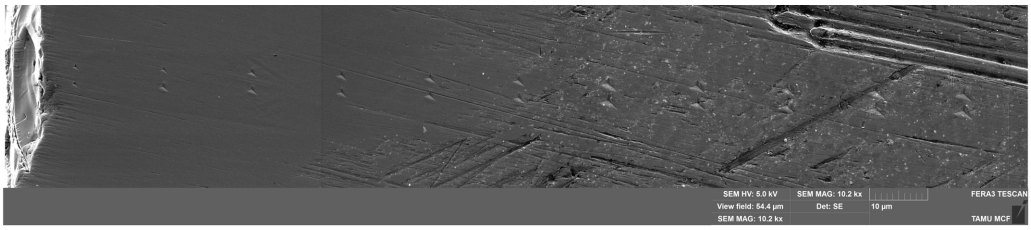

(b) 1010 °C

Figure 5.13: SEM images of cross-section nanoindentation for Zircaloy-4 nitrided for 24 hours at temperatures of 925 and 1010 °C.

surface were based on the indentations of the harder nitrogen layer. This resulted in the larger indentation affected volumes of the softer substrate possibly interacting. In addition to the array spacing, the cross-sectional polishing of Zircaloy-4, as compared to stainless steel samples, required increased preparation time with the 1 µm and 0.3 µm diamond lapping (mechanical grinding) pads based on the SEM images of relatively rough substrate. It is hypothesized that the increased difficulty, which was also notice in surface polishing, may be associated this the hexagonal crystal structure.

The results of the indentation shown in Fig. 5.13 are plotted in Fig. 5.14 showing the nanoindentation cross-section measurements of Zircaloy-4 nitrided for 24 hours at temperatures of 925 and 1010 °C. In addition the these two indentation arrays, two indentation sets at a depth of The reduced modulus and harness were obtained

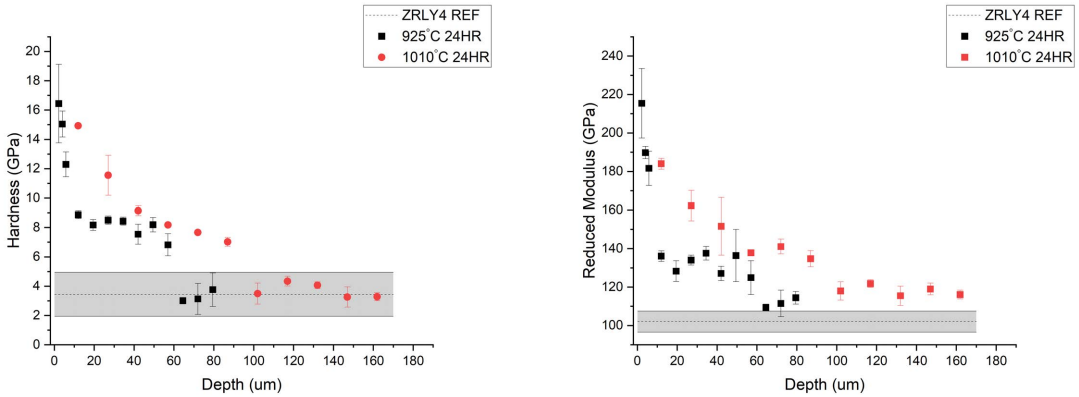

(a) Hardness (b) Reduced Modulus

Figure 5.14: Nanoindentation cross-section measurements of Zircaloy-4 nitrided for 24 hours at temperatures of 925 and 1010 °C.

from the cross sectional characterization. Hardness is noticeably increased from the surface to about 100 microns in depth. This depth region is consistent with the N diffusion zone formation.

Surface indentation and cross sectional indentation were both performed on nitrided Zircaloy-4. Surface indentation tests show that the surface polycrystalline ZrN phase has noticeable hardening. Cross sectional indentation tests show that the nitrogen diffusion zone which forms beneath the surface ZrN layer also exhibit hardening due to the incorporation of N atoms into the matrix. Although these N atoms do not induce nitride phase formation, they increase hardness due to impurity effects.

5.5 Conclusion

Surface nitriding improved the mechanical surface properties of all the investigated cladding materials. The hardness increase in the very near surface region of the steels and Zircaloy-4 was 14-16 GPa and 20-24 GPa, respectively, which was a

significant increase compared to the bulk matrix. At deeper depths, the nitrogen modified layer increased the hardness of all materials by a factor of 3-4 GPa compared to the unnitrided materials. This suggest that nitriding can be used to improve the surface mechanical properties of cladding materials.

6. DIFFUSION KINETICS

A systematic nitridation was performed on 316L, HT9, T91 and Zircaloy-4 as a function of temperatures and time. After nitridation, samples were cross-sectionally polished and the nitrogen layer analyzed to quantitatively measure diffusion lengths and determine boundary locations. The diffusion thickness were then used to calculate the nitriding kinetics for each material.

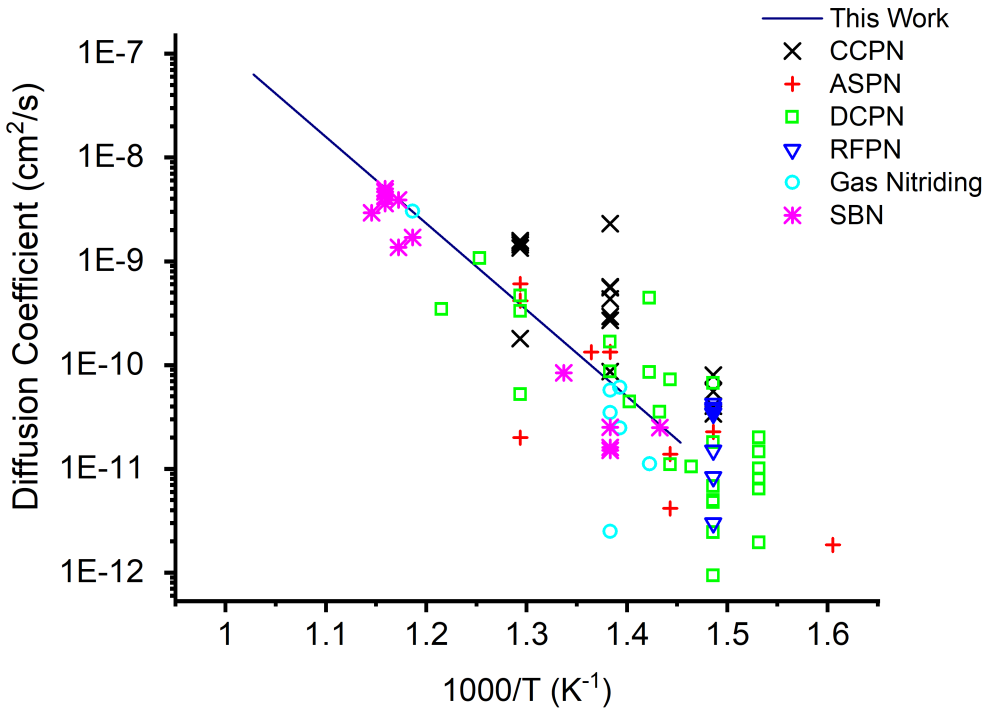

Figure 6.1: Compiled Arrhenius diffusion plot of nitrided 316 by nitriding method from literature [17, 3, 18, 19, 20, 21, 22, 23, 24, 25, 26, 27, 28, 29, 30, 31, 32, 33, 34, 35, 36, 37, 38, 39, 40, 41, 42, 43, 44, 45].

6.1 316L

Figure 6.1 the nitrogen diffusion coefficients for 316 were complied from literature based on reported diffusion coefficients or the calculated using Fick's diffusion equation. For calculated nitrogen diffusion coefficients, the nitrogen layer thicknesses used were based on reported nitrogen layer thickness or from visual inspection of the nitrogen layer thickness show in reported images. Salt bath and gas nitriding are less likely to exhibit high nitrogen diffusion for surface nitriding as there aren't any added heating effect during the nitriding process. This is in contrast to plasma nitriding techniques where temperature variations can occur due to nonuniform energy deposition from plasma ions being drawn to the workpieces edges due to applied voltage potentials.

Though these nitriding techniques may have improved temperature control of the workpiece, they are prone to not achieving sufficient nascent nitrogen to achieve maximum nitrogen diffusion, especially at lower temperatures as they are thermal driven processes. The Arrhenius plot of active screen plasma nitriding diffusion coefficients for 316 also appears to approach a maximum slightly higher than salt bath and gas nitriding. This may be due to the capability of the active screen technique being able to achieve maximum nascent nitrogen to the surface of the workpiece. This could also be attributed to minor temperature gradients between measured temperature and the workpiece surface caused by ion heating.

The plotted direct current, cathodic cage, and radio frequency plasma nitriding nitrogen diffusion coefficients in literature do not approach a theoretical maximum, though only a single temperature was included for radio frequency plasma nitriding. As direct current plasma nitriding applies voltage potential directly to the workpiece, the scattered diffusion coefficients are expected due to nonuniformed heating. As for

cathodic cage, the nitrogen diffusion rates are unexpectedly high as all the cathodic cage experiments included in Fig. 6.1 are at floating potential. A possible reasons for the abnormally high diffusion rates are unintentional bias applied to the workpieces resulting in large temperature variations between temperature measurement location and the surface of the workpiece. Another cause may be due to unforeseen influences of the plasma within the cathodic cage on the temperature measuring system.

6.1.1 Results and Discussion

Figure 6.2 show SEM images of nitrided cross-sections for 316L nitrided at 454, 511 and 596 °C for 30 minutes, 1 hour and 2 hours. The presence of the nitrogen modified layer is visible, including the samples that were not etched. For all the etched samples shown with the exception of the 30 min, 454 °C samples, there is indication of the decomposition of the γ_N phase as describe in literature. The decomposition starting at grain boundaries, forming CrN precipitates, can be noted in Fig. 6.2c and Fig. 6.2e. EDS analysis of the atomic nitrogen concentration versus depth is shown in Fig. 6.3. While only full cross-sectional EDS data sets are have been plotted, the nitrogen layer thicknesses measured using the SEM images were checked using EDS to verify the depth at which nitrogen was no longer measurable. It should be noted that the SEM images were taken with the secondary electron detector. The use of the backscatter detector may provide greater visibility of nitrogen layer in polished 316 cross-sectional samples that have been nitrided.

The fitting for calculated D(T) using EQN 4.2 are graphed in Fig. 6.4, where the vertical axis is the nitrogen layer thickness and horizontal axis is the nitriding time in minutes. The results of the calculated diffusion coefficients in Fig. 6.4 are plotted in the Arrhenius diffusion graph for 316L and denoted as Time Averaged in Fig. 6.5. The calculated D_0 and activation energy, Q, for nitrogen in 316L are

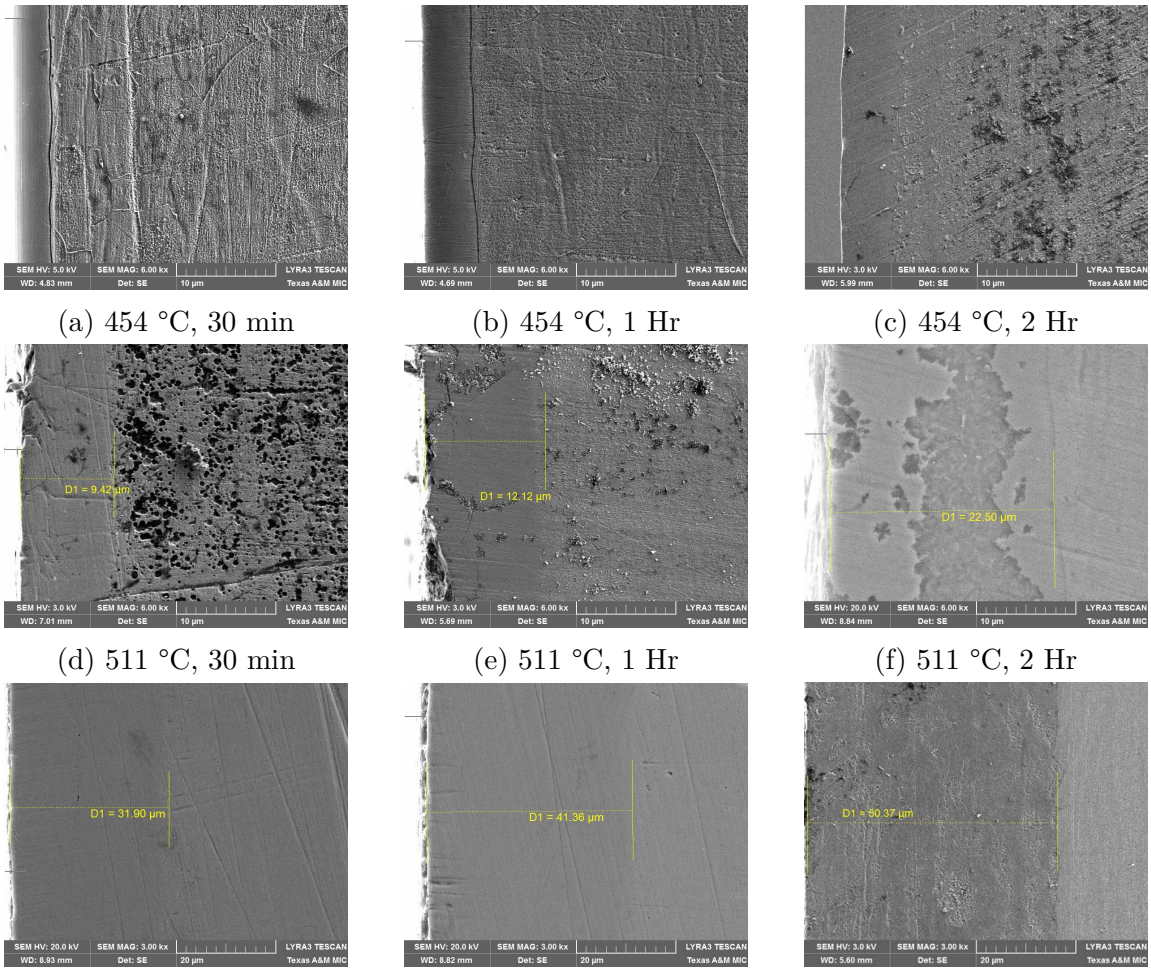

(a) 454 °C, 30 min (b) 454 °C, 1 Hr (c) 454 °C, 2 Hr

(d) 511 °C, 30 min (e) 511 °C, 1 Hr (f) 511 °C, 2 Hr

(g) 596 °C 30 min (h) 596 °C, 1 Hr (i) 596 °C, 2 Hr

Figure 6.2: SEM cross-sectional images of 316L nitrided at 454, 511 and 596 °C for 30 minutes, 1 hour and 2 hours.

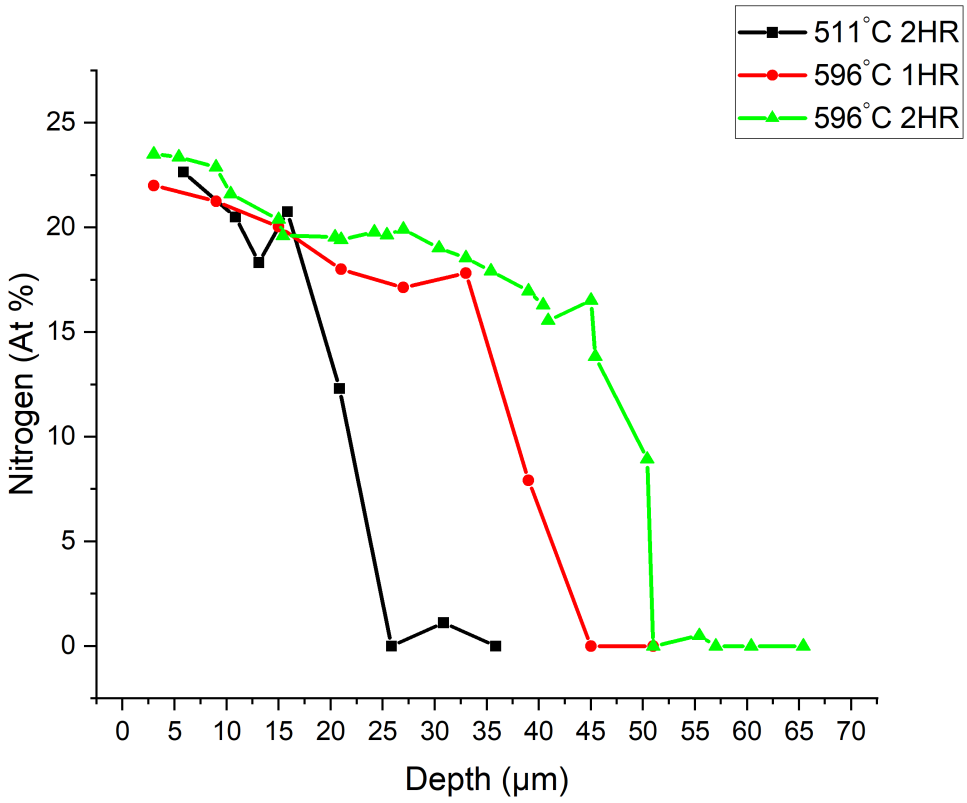

Figure 6.3: Plot of atomic nitrogen percent versus depth of nitrided 316L as measured by EDS.

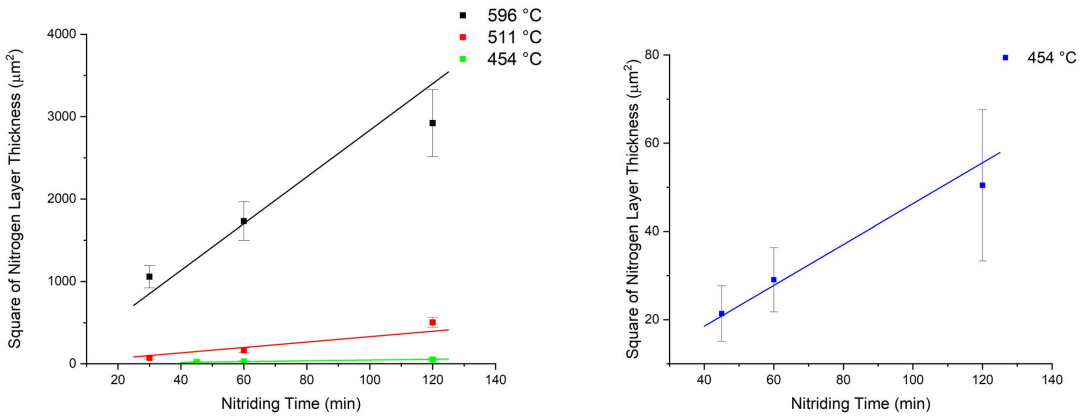

(a) (b)

Figure 6.4: Graphs of L^2 diffusion coefficient fittings for 316L.

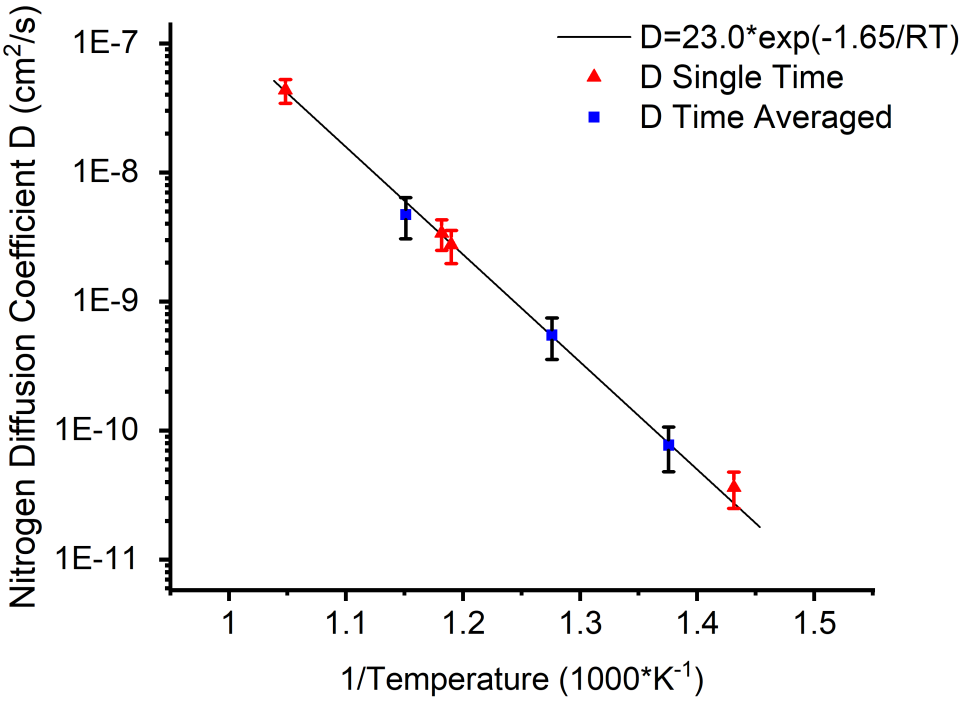

Figure 6.5: Arrhenius diffusion plot of nitrided 316L.

23.01±6.55 cm^2/sec and -1.65±0.02 eV/atom respectively. As can be seen in Fig. 6.1, the calculated diffusion parameter agrees well with the literature.

Though the Arrhenius diffusion parameters do agree with values reported in literature, the unexpected temperature shift from target values resulted in almost all nitriding temperatures being above 430 °C. As can be seen in Fig. 6.5, the lowest nitriding temperature of 425 °C had a diffusion coefficient of 3.62E-11 cm^2/sec, which is above the predicted value. Also, the temperature adjustment factor was based on realignment at 590 °C and assumed a linear error from 0 °C. It is possible that the floating potential of the plasma or the internal losses of thermometer used to measure temperature resulted in a non-linear error. This could result in the uncertainty of the diffusion parameters increasing proportionally as the temperature difference

from 590 °C increases. It is hypothesized that there may be a diffusion rate shift around 430 °C that is a function of time. As it is well established that the γ_N phase is metastable and largely depended on time and temperature, the diffusion kinetics of nitrogen in 316 may not be accurately modeled using the standard Arrhenius equation. As this author has not found any literature on this subject and the nitrogen diffusion rates for low temperature nitriding of 316 found in literature vastly vary, further experiments would need to be performed.

6.2 T91 Results and Discussion

Figure 6.6 shows SEM images of etched nitrided cross-sections for T91 nitrided at temperatures between 454 and 681 °C for durations between 20 minutes and 2 hours. The etching duration was 30 seconds. Unlike 316 cross-sections, the full depth of the nitrogen depth is not very obvious using visual inspection of the SEM images. The nital etching of the 454 °C T91 sample nitrided for 20 minutes, shown in Fig. 6.6a, does not have a distinctive boundary. While the nital etching was only for 30 seconds, it did produce small cracks covering most of the depth of the nitrogen diffusion zone. In general, the Marble's etchant attacked the substrate while the Nital etchant attacked the nitrogen layer. At temperatures above 590 °C, both etchants fully revealed the saturated nitrogen layer but did not fully reveal the end of the diffusion zones which had a typical width of 20 µm. Both nital and Marble's etchants may be capable of fully revealing the diffusion zone if the etching time is greatly extended, though another etchant may produce better results for T91 surface nitridation.

Fig. 6.7 show SEM surface images of T91 nitrided for 30 minutes at 454 and 556 °C. The surface morphology shown are typical for the nitrided T91 at various temperatures except for the increase of surface deposition, which has a powder like

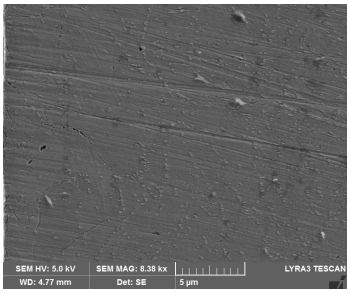

(a) 454 °C, 20 min, Nital

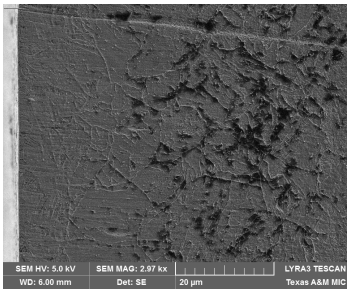

(b) 454 °C, 2 Hr, Marble

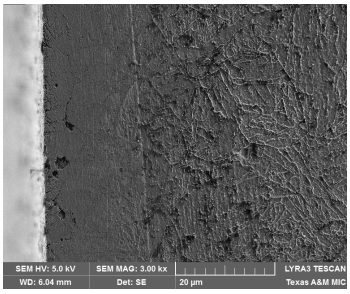

(c) 511 °C, 30 min, Marble

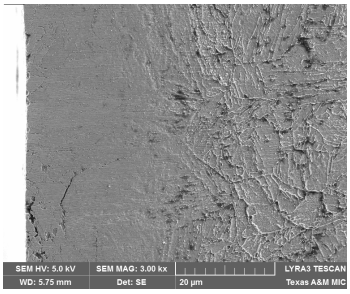

(d) 511 °C, 1 Hr, Marble

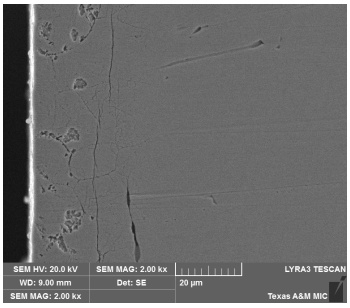

(e) 556 °C, 30 min, Nital

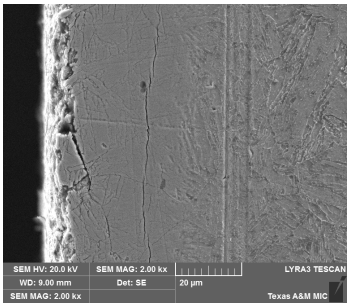

(f) 556 °C, 30 min, Marble

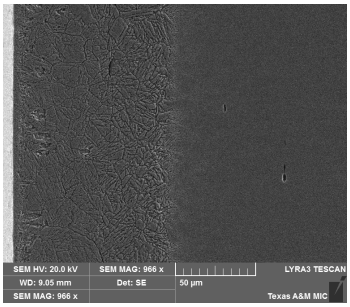

(g) 596 °C, 2 Hr, Nital

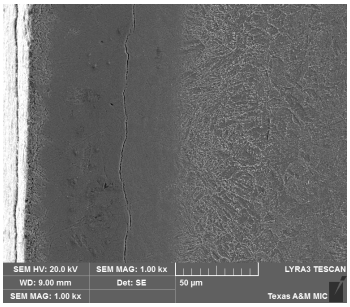

(h) 596 °C, 2 Hr, Marble

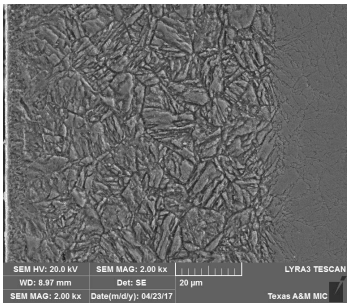

(i) 681 °C, 30 min, Nital

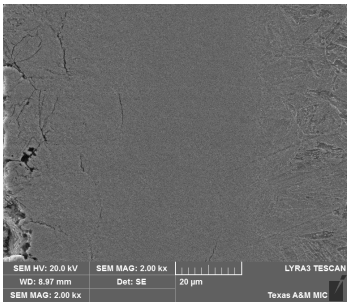

(j) 681 °C, 30 min, Marble

Figure 6.6: SEM cross-sectional images of nitrided T91 etched with Marble's regent or Nital.

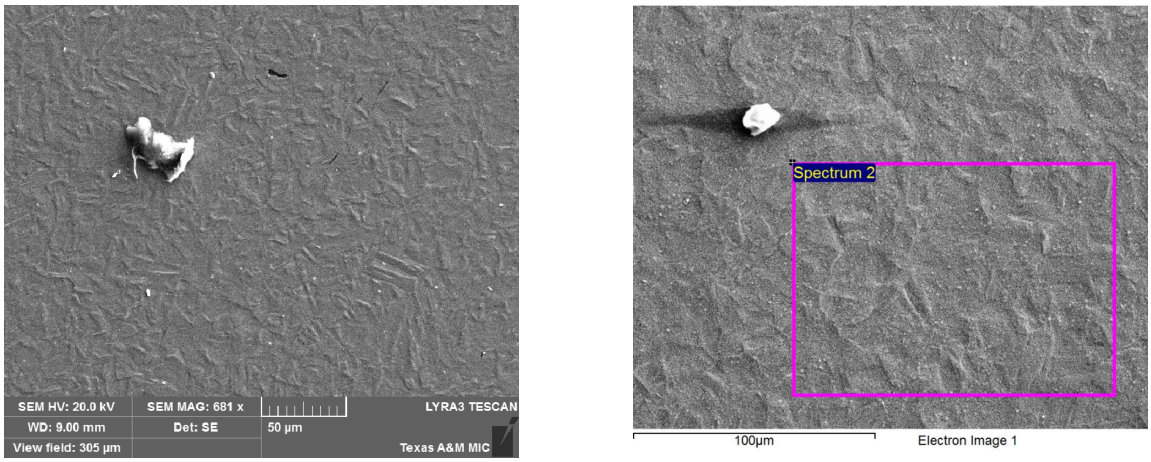

(a) 454 °C (b) 556 °C

Figure 6.7: SEM surface images of T91 nitrided for 30 minutes.

appearance, with time and temperature. The measured surface nitrogen content using EDS ranged from 28 to 32 At% for nitrided T91. In Fig. 6.8, the cross-sectional atomic nitrogen concentrations versus depth are shown. The nitrogen modified layer typically contained 13 to 15 At% nitrogen which increased to about 30 At% closer the surface.

The linearized time averaged diffusion fitting for the T91 are shown in Fig. 6.9 and the results are plotted in Fig. 6.10 along with the single time diffusion coefficients. The calculated D_0 and Q for nitrogen in T91 are 9.91E-4 ± 1.97E-4 cm^2/sec and -0.82 ±0.02 eV/atom respectively.

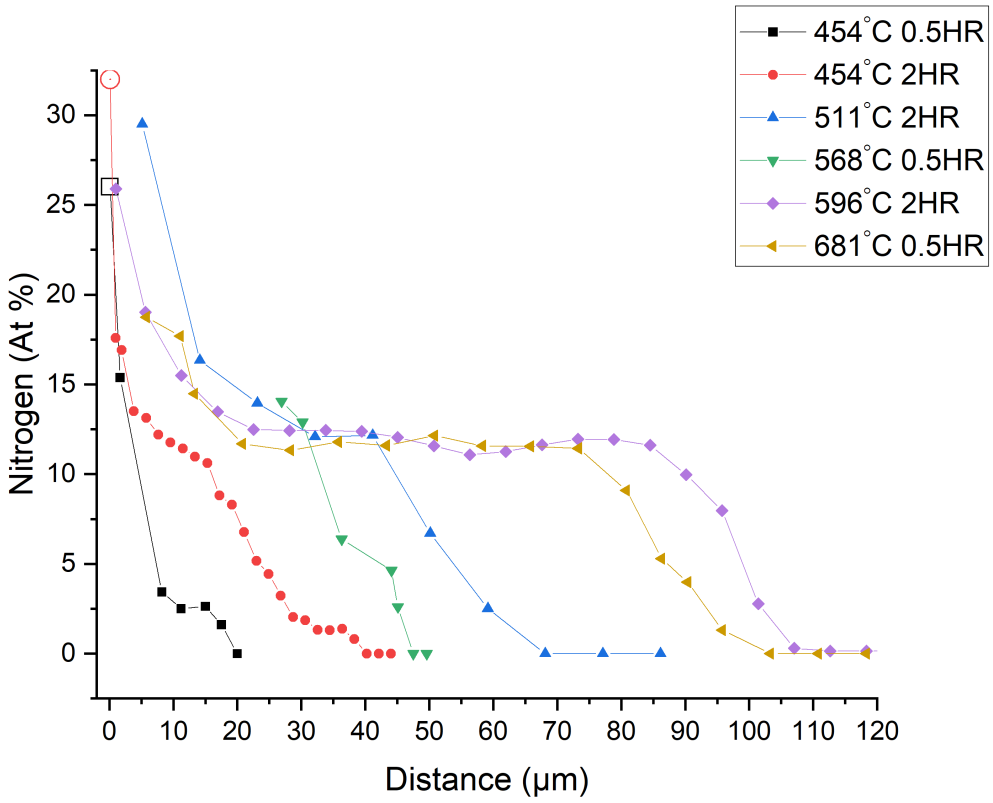

Figure 6.8: Plot of atomic nitrogen percent versus depth of nitrided T91 as measured by EDS.

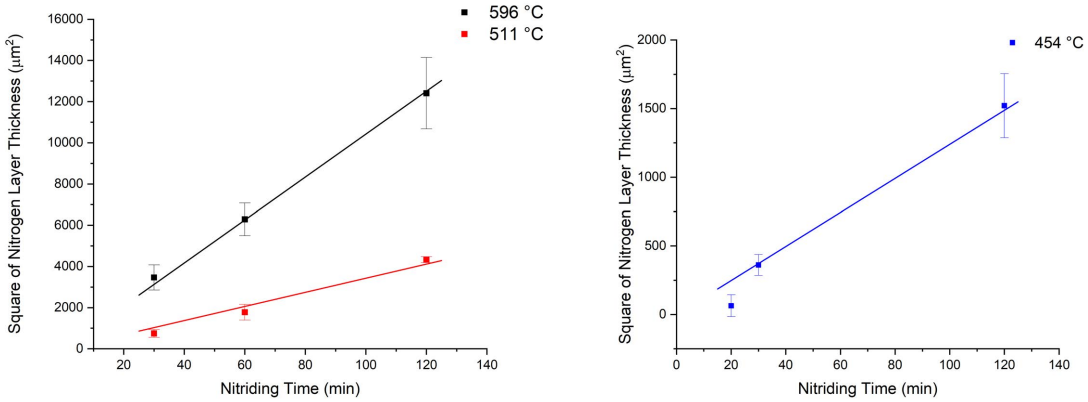

(a) (b)

Figure 6.9: Graphs of L^2 diffusion coefficient fittings for T91.

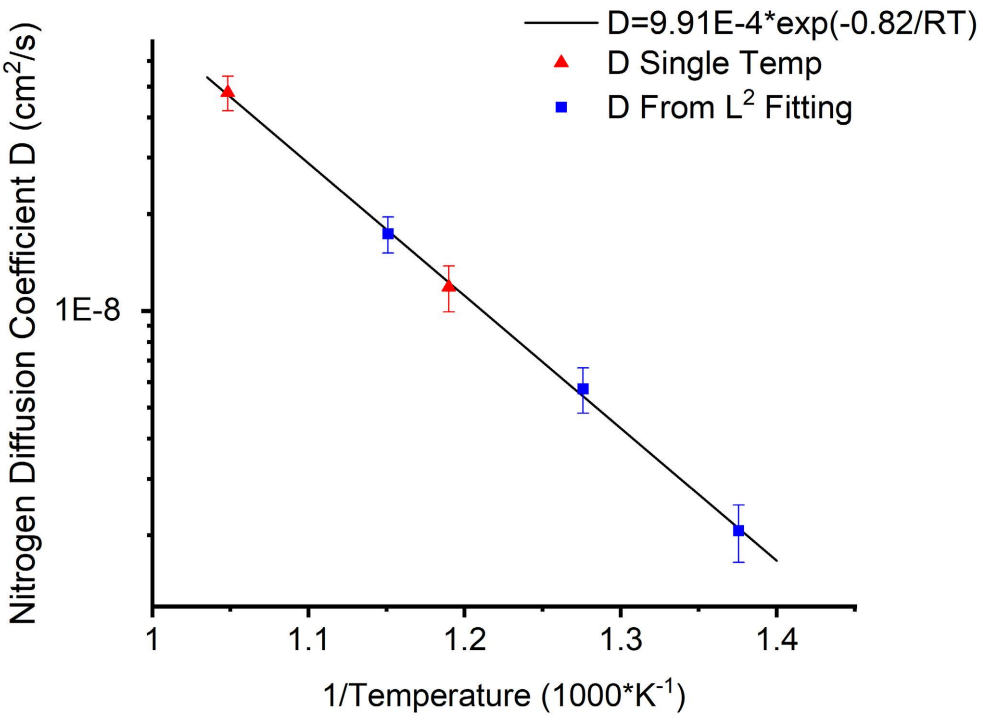

Figure 6.10: Arrhenius diffusion plot of nitrided T91.

6.3 HT9

As no data has been found for nitriding HT9, nitridation of 410 and 420 stainless steels has been used for comparison. In Fig. 6.11 the nitrogen diffusion coefficients obtained from literature for 410 and 420 stainless steels have been compiled and plotted by nitriding method. As both materials diffusion data overlapped, distinction between 410 and 420 stainless steels diffusion data was not included. As previously discussed for Fig. 6.1, the same trends by nitridation method can be seen.

6.3.1 HT9 Results and Discussion

SEM cross-sectional images of nitrided HT9 are shown in Fig. 6.12. As with etching nitrided T91, both nital and Marble's etchants reveal the saturated nitride layers. In Fig. 6.12a, the visible saturated layer depth was approximately 12 µm followed by the diffusion zone which was approximately 8 µm wide. Figures 6.12d and 6.12e compares nital etching durations of 30 seconds and 2 minutes respectively. The 30 second etch depth was 20 µm while the measure nitrogen diffusion depth was 38 µm. Extending the etching duration to 2 minutes increased the etch depth to 30 µm. This suggests that the nital etchant may be able to fully reveal the nitrogen layer with longer etching duration. The cross-section etching using Kalling's for 20 seconds at room temperature was tested on a few HT9 samples. The visibility of the nitrogen diffusion depth was comparable to nital and Marble's etchants.

The nitrided HT9 cross-sectional atomic nitrogen concentrations versus depth are shown in Fig. 6.13. The linearized time averaged diffusion fitting for the HT9 are shown in Fig. 6.14 and the results are plotted in Fig. 6.15 along with the single time diffusion coefficients. The calculated D_0 and Q for nitrogen in HT9 are 5.16 ± 3.52 cm^2/sec and -1.46 ± 0.04 eV/atom respectively.

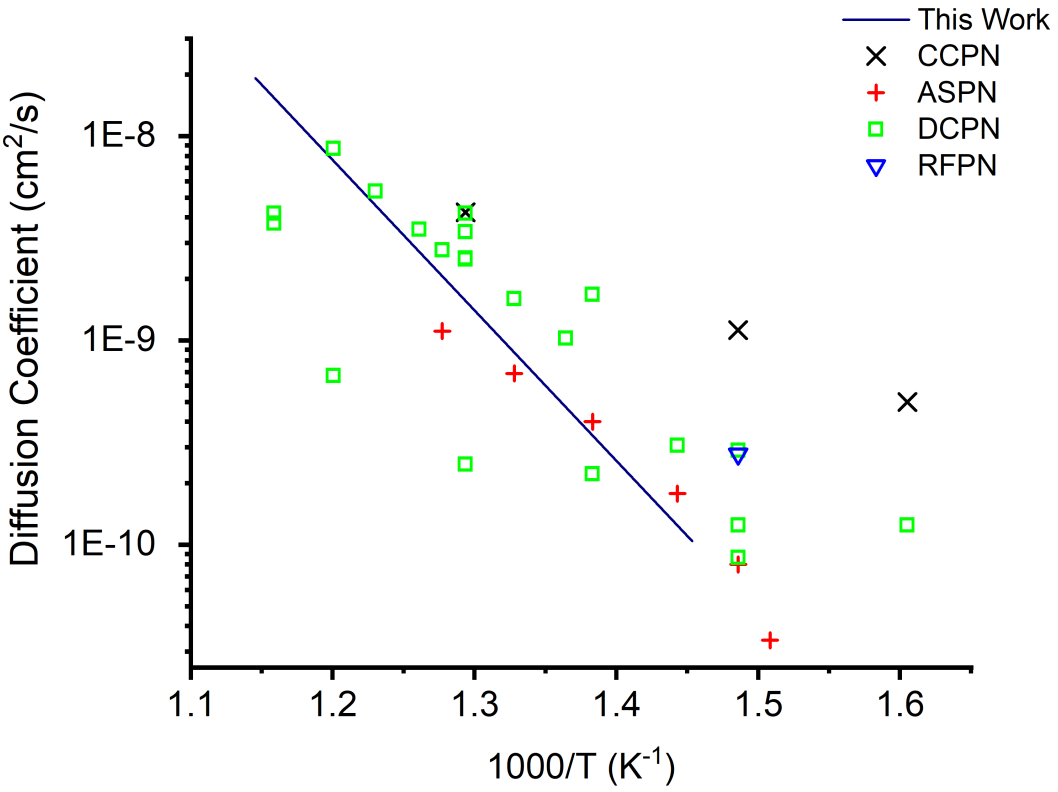

Figure 6.11: Compiled Arrhenius diffusion plot of nitrided 410 and 420 stainless steels by nitriding method from literature [46, 47, 48, 49, 50, 51, 52, 53, 54, 55, 56, 57, 58, 59].

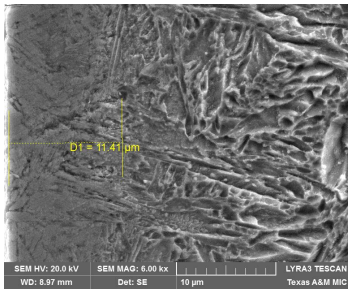

(a) 454 °C, 2 Hr, Marble

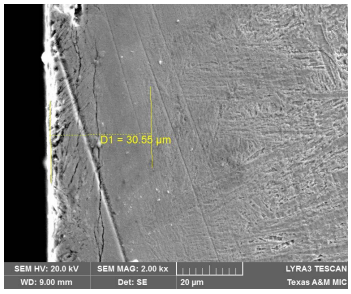

(b) 511 °C, 1 Hr, Kalling

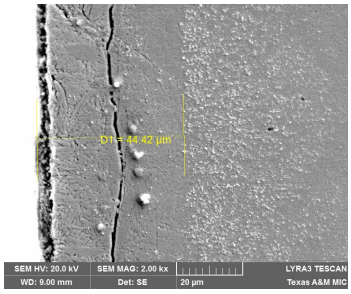

(c) 511 °C, 2 Hr, Kalling

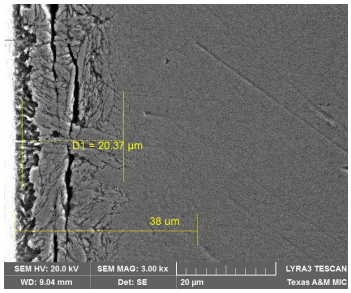

(d) 556 °C, 30 min, Nital

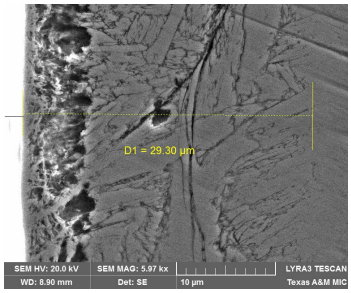

(e) 556 °C, 30 min, Nital

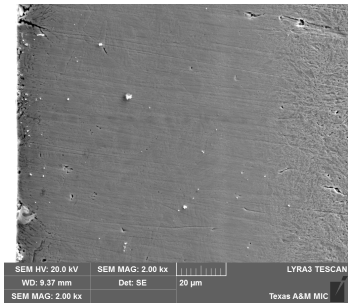

(f) 596 °C, 2 Hr, Kalling

Figure 6.12: SEM cross-sectional images of nitrided HT9 etched with Marble's, Kalling's or Nital.

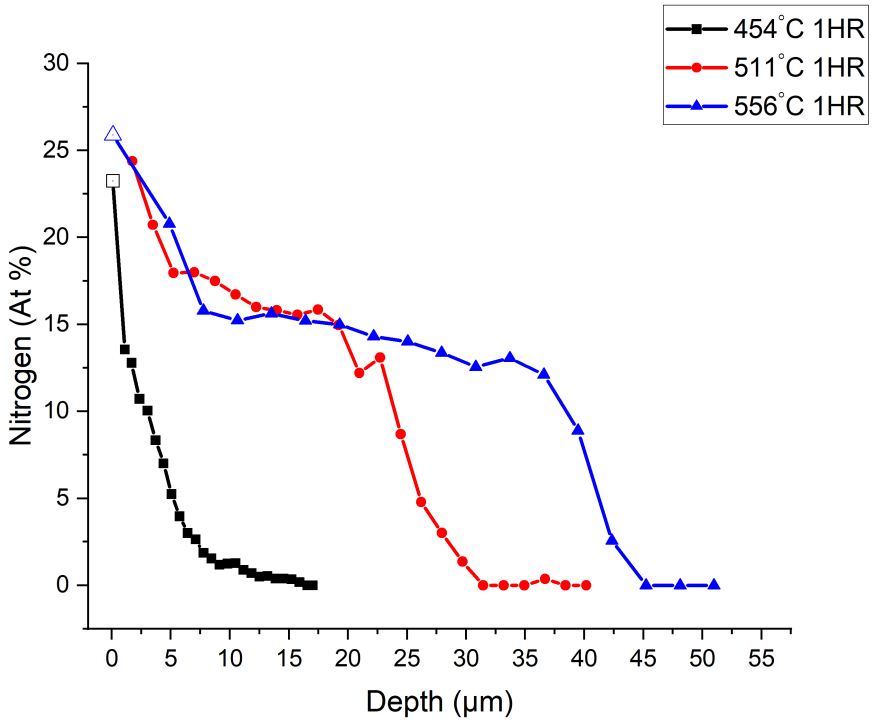

Figure 6.13: Plot of atomic nitrogen percent versus depth of nitrided HT-9 as measured by EDS.

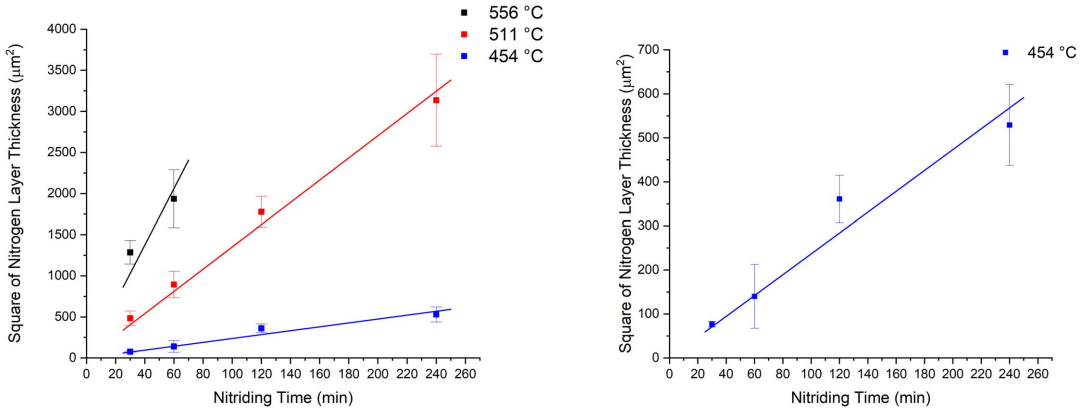

(a) (b)

Figure 6.14: Graphs of L^2 diffusion coefficient fittings for HT-9.

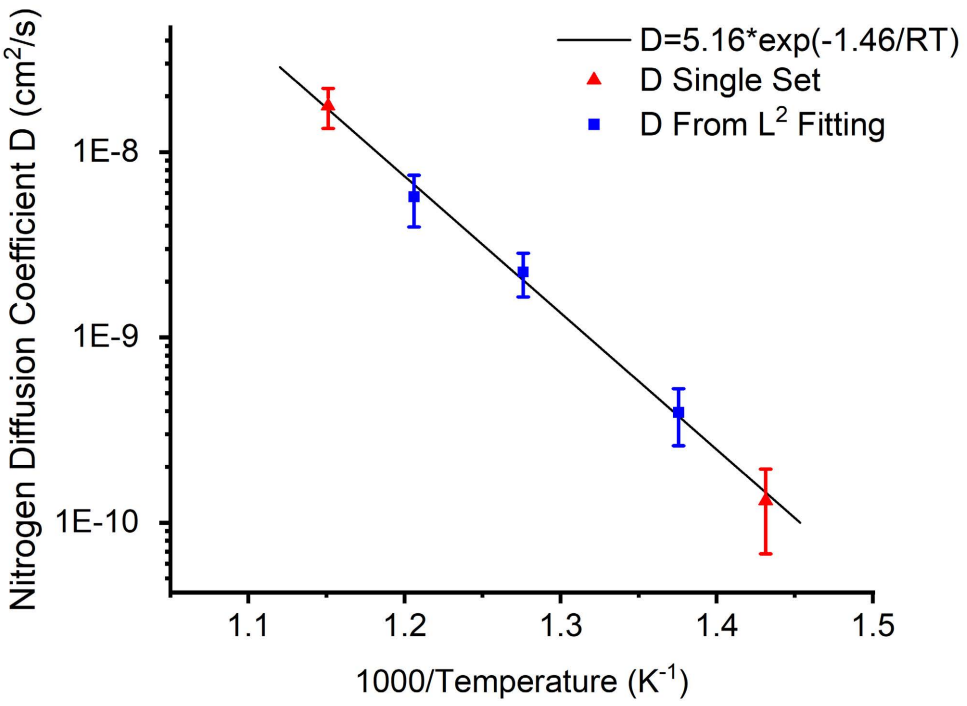

Figure 6.15: Arrhenius diffusion plot of nitrided HT-9.

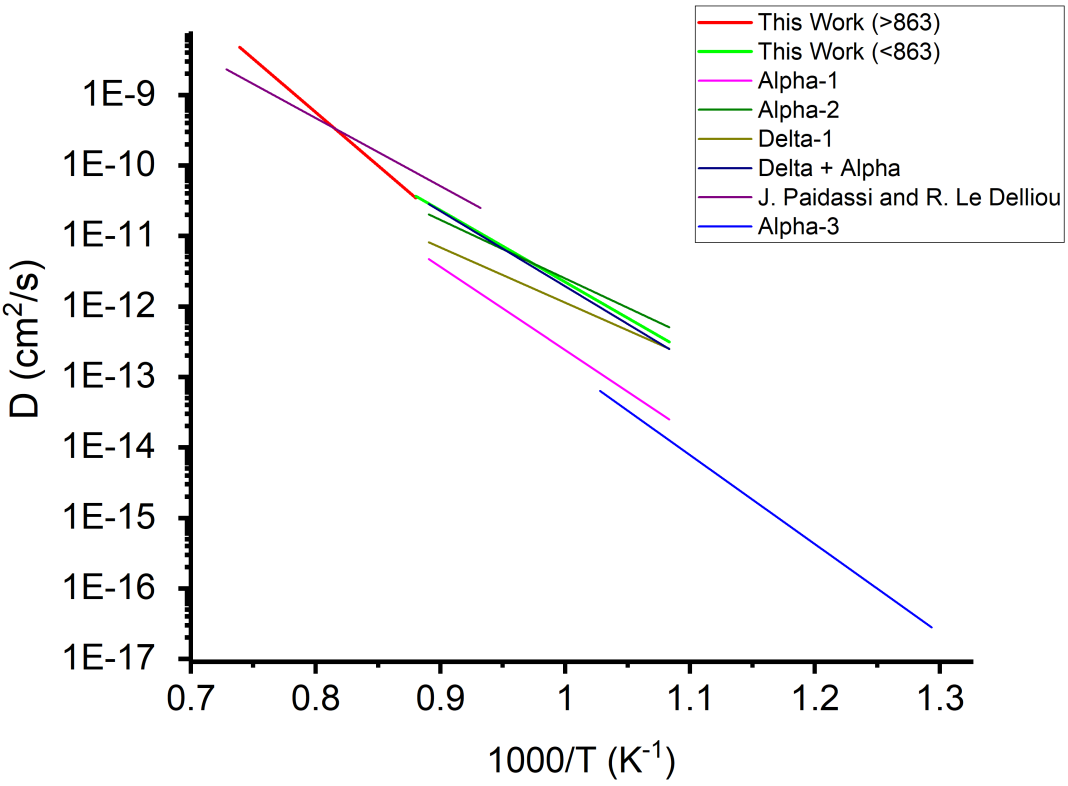

Figure 6.16: Compiled Arrhenius diffusion plot of nitrogen diffusion in zirconium from literature [60, 61, 62].

Little data has been found pertaining to nitrogen diffusion in Zircaloy-4 [15]. As Zircaloy-4 is primarily composed of zirconium, comparative nitrogen diffusion in zirconium information is shown in Fig. 6.16 [60, 61]. For most diffusion data pertaining to Zr-N systems, the diffusion rates are primarily for single phases, highly variable and covers a wide range of temperatures [60, 61, 62, 131]. Work performed

by J. Paidassi and R. Le Delliou, referenced by Desmaison and Smeltzer, is denoted in purple with temperatures from 800 to 1100 °C [60]. Alpha-1, Alpha-2 and Delta-1 in Fig. 6.16 are diffusion parameters for α-ZrN_x and δ-ZrN obtained from Rosa and Hagel's work on nitrogen diffusion in zirconium [61]. The "Delta + Alpha" diffusion fitting is based on Alpha-1 at 650 °C, Alpha-2 at 825 °C, and Delta-1. The combined diffusion parameter results in an effective diffusion rate with a D_0 and Q of 0.09 cm^2/sec and -2.12 eV/atom respectively. The choice of the α-ZrN_x diffusion data was based on the method of measurement used for Alpha-2 and its inferred associated error being minimum at 825 °C. Alpha-3 diffusion plot is from work performed by Anttila et al. for nitrogen implanted in zirconium [62].

6.4.1 Results

Cross-sectional images of nitrided Zircaloy-4 are shown in Fig. 6.17. Figures a-c were nitrided at floating potential and Figures d and e at cage potential. For nitrided Zircaloy-4, the nitrogen modified layer depth is highly visible with proper mechanical polishing techniques. The direction of lapping for the last step of mechanical grinding using 0.3 µm diamond lapping should be perpendicular to nitrided surface of interest. If the polishing direction is parallel to the nitrogen layer, the hardened nitrogen layer depth may become ambiguous using visual inspection of SEM images. An example of this can be seen by comparing Fig. 6.17b and Fig. 6.17c where the first was lapped perpendicular and the latter parallel.

The nitriding of Zircaloy-4 was unique compared to the steel samples as the casing formed on all surfaces. This is shown in Fig. 6.17e. In Fig. 6.18 the surface images of nitrided Zircaloy-4 are shown. Images a-f are surfaces of nitrided Zircaloy-4 that were directly exposed to the plasma (tops of the samples) at various nitriding temperatures and time with cage bias. Images g-i are the back or bottom surfaces

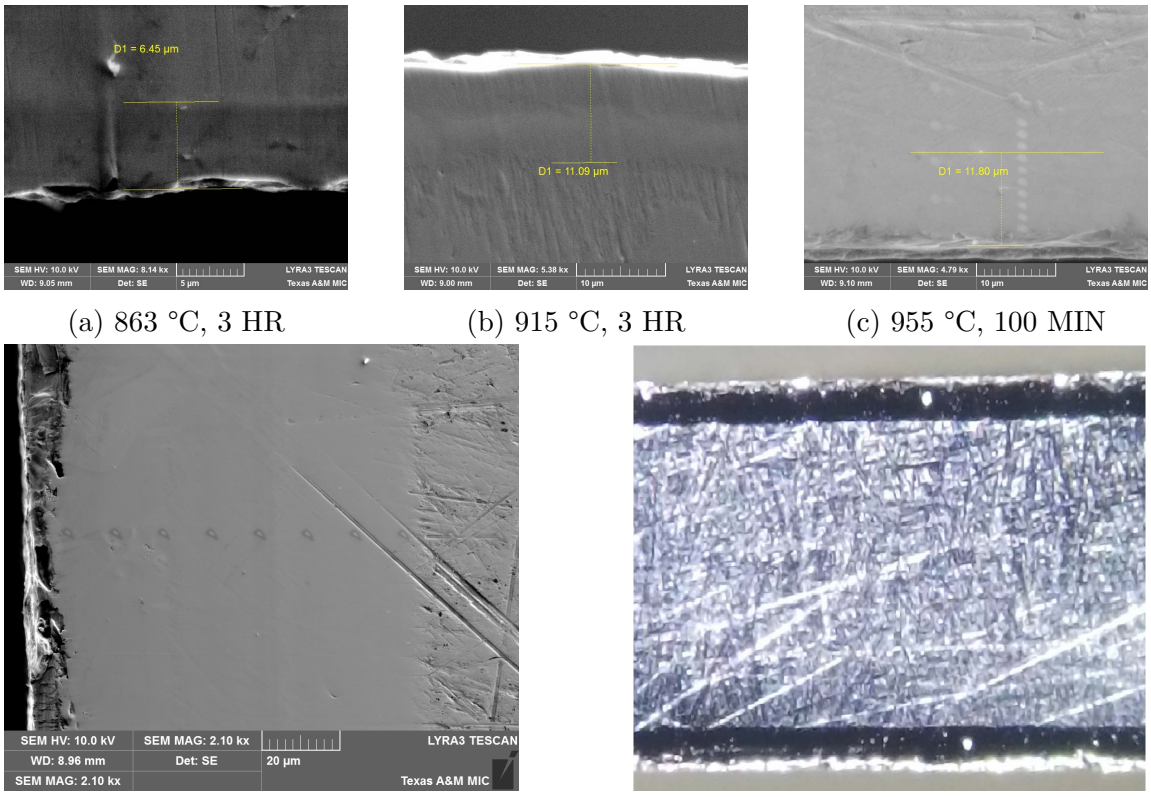

(a) 863 °C, 3 HR (b) 915 °C, 3 HR (c) 955 °C, 100 MIN

(d) 1010 °C, 24 HR (e) 1010 °C, 24 HR

Figure 6.17: Cross-sectional images of nitrided Zircaloy-4. SEM images a-c were nitrided at floating potential. Images d and e were nitrided at with cage potential bias. Image e shows the nitrogen layer on top and bottom surfaces of the sample.

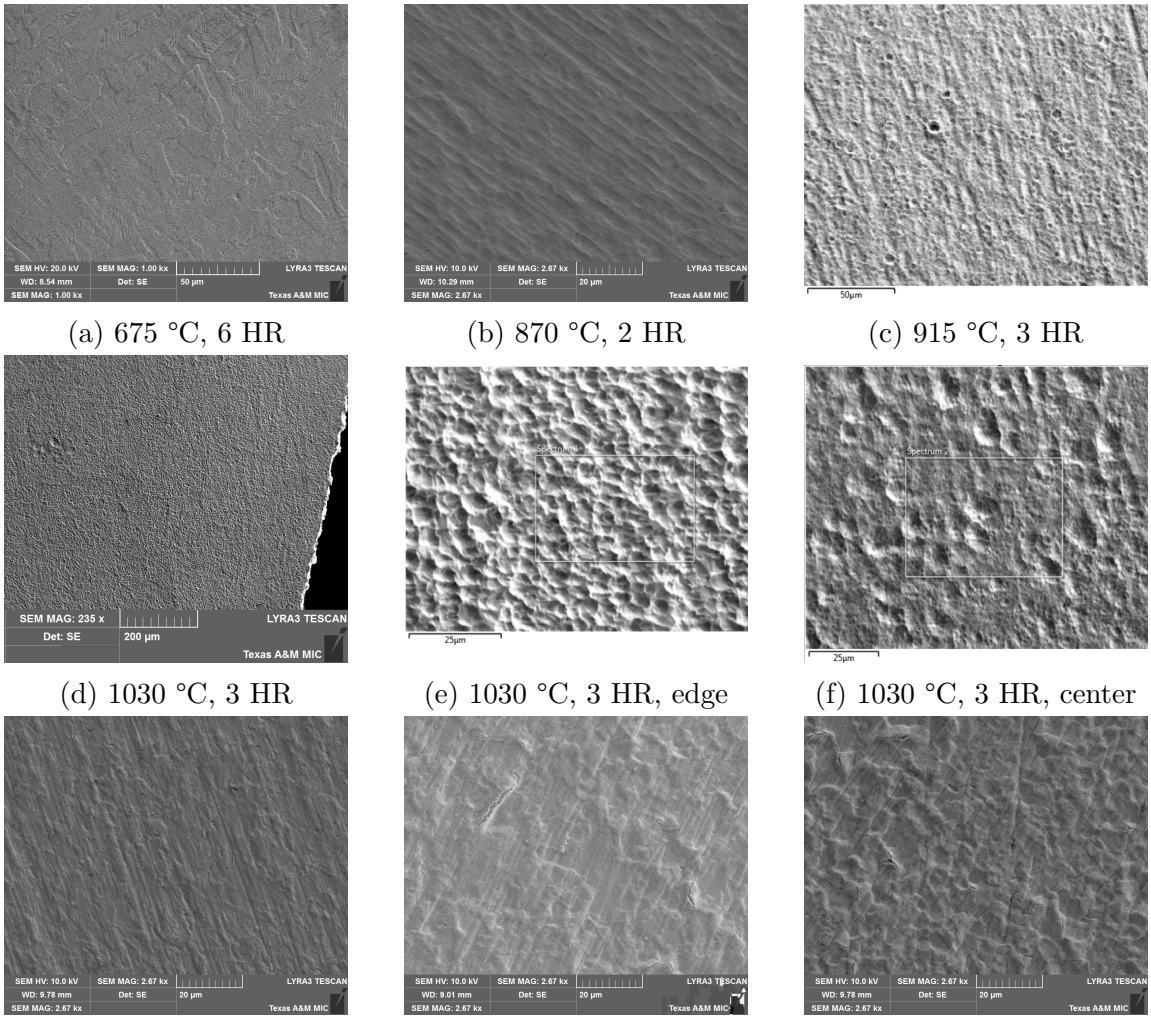

(a) 675 °C, 6 HR (b) 870 °C, 2 HR (c) 915 °C, 3 HR

(d) 1030 °C, 3 HR (e) 1030 °C, 3 HR, edge (f) 1030 °C, 3 HR, center

(g) 915 °C, 3 HR (h) 1030 °C, 3 HR (i) 1010 °C, 24 HR

Figure 6.18: SEM surface images of nitrided Zircaloy-4 with cage bias.

of nitrided Zircaloy-4 which were not directly exposed to the plasma. As can be seen, the top surfaces appear to have been etched by the energetic plasma ions. The surfaces of the bottom of the samples do not exhibit the etching effect though at temperatures above 1000 °C cracks in the nitrided surfaces were formed. There was no noticeable differences in the nitrogen layer depths formed on of the top, side and bottom of the nitrided Zircaloy-4 samples.

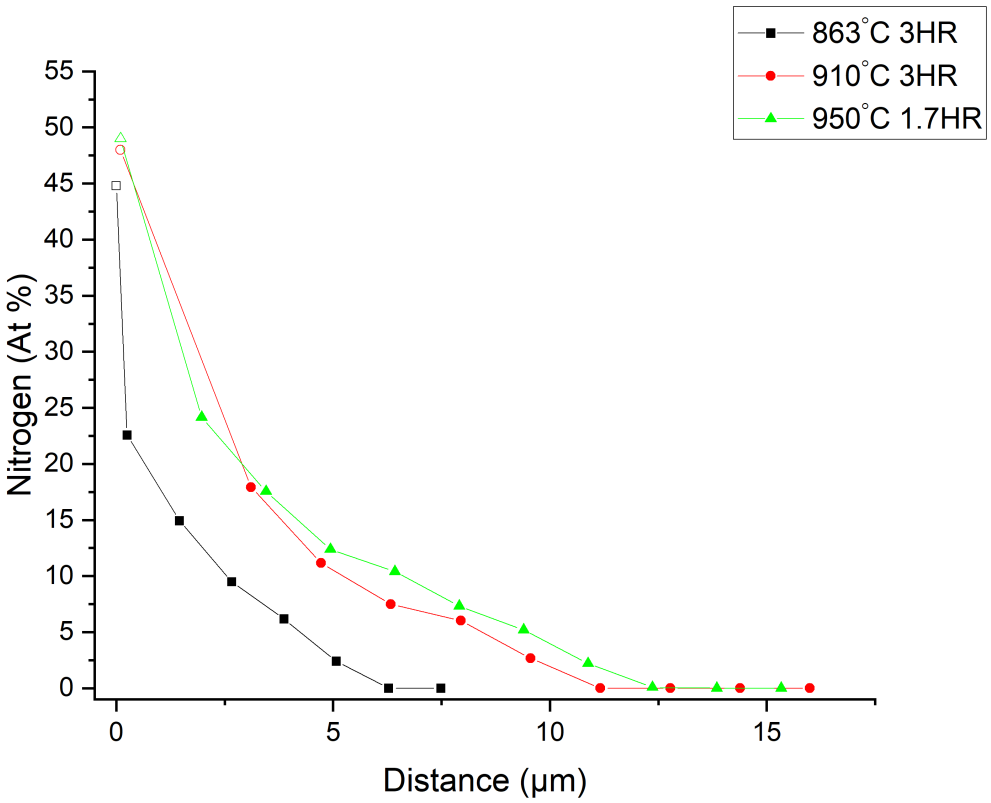

Figure 6.19: Plot of atomic nitrogen percent versus depth of Zircaloy-4 nitrided, at floating potential, as measured by EDS.

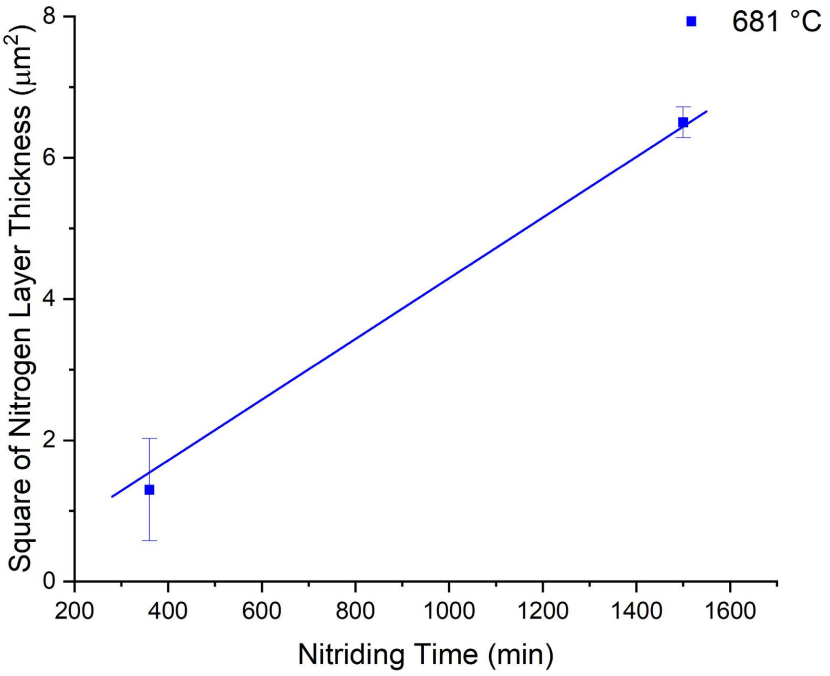

Figure 6.20: Graphs of L^2 diffusion coefficient fittings for Zircaloy-4 at 681 °C.

In Fig. 6.19 the atomic nitrogen concentration versus depth is plotted for Zircaloy-4 nitrided at 863, 910, and 950 °C. In Fig. 6.20 the time averaged nitrogen diffusion coefficient for Zircaloy-4 is plotted. As the nitriding of Zircaloy-4 was primarily performed under cage bias which resulted in inaccurate temperature measurement due to ion energy deposition due to the cage bias, the nitridation of Zircaloy-4 at floating potential was performed to measure diffusion coefficient primarily at single temperatures. This resulted in the diffusion data having been spread over a wide range of temperatures instead of single temperatures with multiple durations.

The effective nitrogen diffusion coefficients for nitriding Zircaloy-4 are plotted in Fig. 6.21. As the nitriding temperatures exceeded 863 °C at which β-ZrN_x is formed, two diffusion parameters have been calculated. At temperatures above 863 °C, the calculated D_0 and Q were 706 ± 693 cm^2/sec and -3.00 ± 0.09 eV/atom respectively. The calculated D_0 and Q for temperatures below 863 °C were 3.35E-2 ± 0.6E-2 cm^2/sec and -2.02 ± 0.02 eV/atom respectively. As can be seen in the plotting of the fitted diffusion parameters, the diffusion rate increases at temperatures above 863 °C. This is due to the increased nitrogen diffusivity of the β-ZrN_x phase which is formed above 863 °C. The fittings suggests that nitride layer thickness can be well controlled and are relatively in good agreement with data shown in Fig. 6.16.

Using the derived effective nitrogen diffusion in Fig. 6.21, the temperature of the Zircaloy-4 samples nitrided with bias at cage potential were calculated based on the nitrogen layer thickness and nitriding duration. The typical temperature difference between the diffusion derived temperatures and the measured temperatures of the biased samples was 30 to 50 °C. In Fig. 6.22 the cross-sectional atomic nitrogen concentration versus depth is plotted for Zircaloy-4 nitrided with cage bias. The surface nitrogen concentration for most samples was 45 to 50 at% with the exception of the sample nitrided at 870 °C for 2 hours. The 870 °sample surface nitrogen

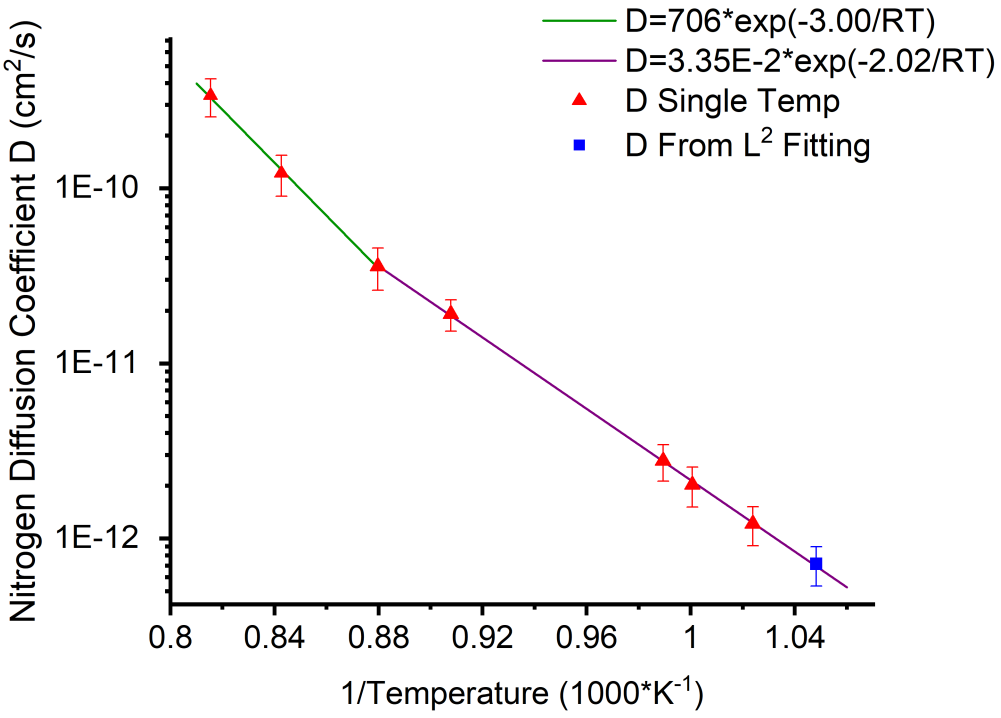

Figure 6.21: Arrhenius diffusion plot of nitrided Zircaloy-4.

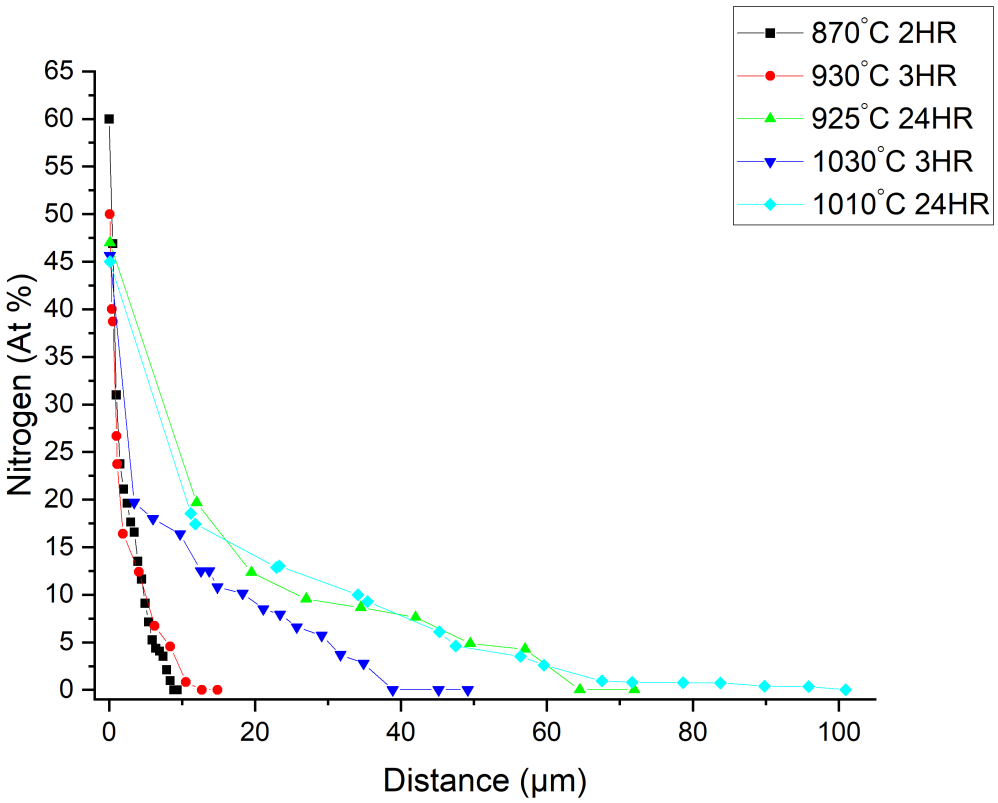

Figure 6.22: Plot of atomic nitrogen percent versus depth of Zircaloy-4 nitrided, at cage bias potential, as measured by EDS.

concentration was measured to be 60 at% and had a maroon and gold color as shown Fig. 7.13in the next chapter. This was unique compared to other samples which were gold colored indicative with the formation of δ-ZrN. This may indication that the metastable hyperstoichiometric ZrN was formed on the surface.

In contrast to Fe and Fe-based alloys, diffusivities of N in Zr and Zr-based alloys were much lower. Hence, higher nitridation temperatures and longer nitridation times were required. Furthermore, δ-phase formation in Zircaloy-4 was limited to near surface region, although N diffusion depth of α-phase ZrN was deeper. After cross-sectional polishing, the N rich layer was clearly visible.

6.5 Conclusion

Key parameters were identified to control the nitridation process. Systematic adjustments of bias, temperature, time, pressure, cage-to-sample distance, and position of samples within the cage showed that the most critical parameters were temperature and time. These two parameters can be further combined into one single parameter, the diffusion length of nitrogen atoms, which determines the thickness of the nitrided layers. The effective nitrogen diffusion coefficient, D_0 and activation energy, Q of 316L is 23.01±6.55 cm2/sec and -1.65±0.02 eV/atom, respectively. The calculated D_0 and Q for nitrogen in T91 are 9.91E-4 ± 1.97E-4 cm^2/sec and -0.82 ±0.02 eV/atom respectively. The calculated D_0 and Q for nitrogen in HT9 are 5.16 ± 3.52 cm^2/sec and -1.46 ± 0.04 eV/atom respectively. At temperatures above 863 °C, the calculated D_0 and Q were 706 ± 693 cm^2/sec and -3.00 ± 0.09 eV/atom respectively. The calculated D_0 and Q for temperatures below 863 °C were 3.35E-2 ± 0.6E-2 cm^2/sec and -2.02 ± 0.02 eV/atom respectively.

7. CORROSION TESTING IN NACL

The present study compared the corrosion resistance of nitrided samples in NaCl by using a potentiodynamic polarization technique as a fast way to evaluate the impact of the nitridation process [83, 84, 85, 86, 8, 6]. As many parameters significantly affect potentiodynamic polarization measurements, such as scan rate, de-aerated vs. aerated electrolyte, temperature, and electrolyte type and concentration, the results are difficult to compare to those found in literature. While the corrosion testing procedure utilized in this study was based on ASTM G3 and G5 standardized procedures, which is also similar to NACE's standardized procedure, use of potentiodynamic polarization techniques found in literature often use arbitrary parameters. This results in evaluation of the corrosion measurements in many studies to only be directly correlated to each individual set of measurements within each study. While the corrosion rates can not be directly compared due to variation in test parameters, general trends in measured current densities are still useful.

β_a (mV/dec)	β_c (mV/dec)	R_p $(kOhm/cm^2)$	E_{corr} (mV)	i_{corr} (nA/cm^2)
633 ±313	93 ±20	198 ±59	-214 ±34	179 ±37

Table 7.1: 316L reference potentiodynamic corrosion measurements in 3.5 wt% NaCl at 30 °C.

7.1 316 Results and Discussion

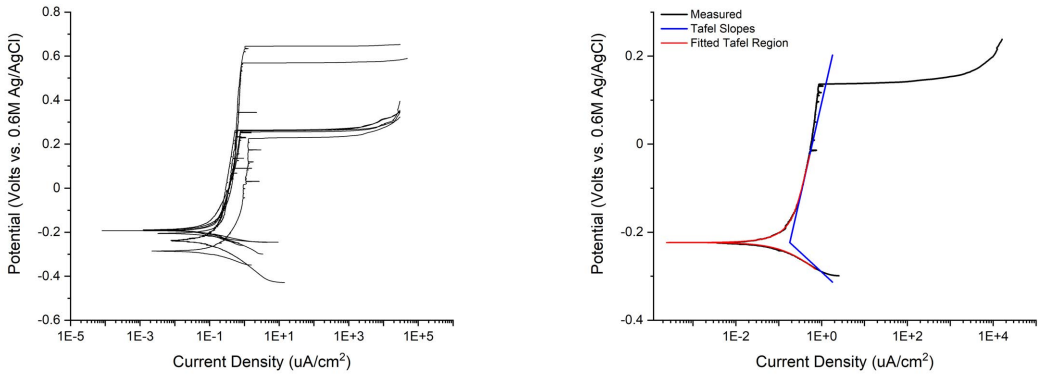

(a) (b)

Figure 7.1: 316L reference polarization curves.

Figure 7.1 shows the results of potentiodynamic polarization measurements of unnitrided 316L reference samples. Figure 7.1a contains all of the 316L corrosion measurements. Figure 7.1b shows calculated Tafel fitting of the typical reference 316L potentiodynamic polarization curve. The Tafel slopes and associated measurements are shown in Table 7.1.

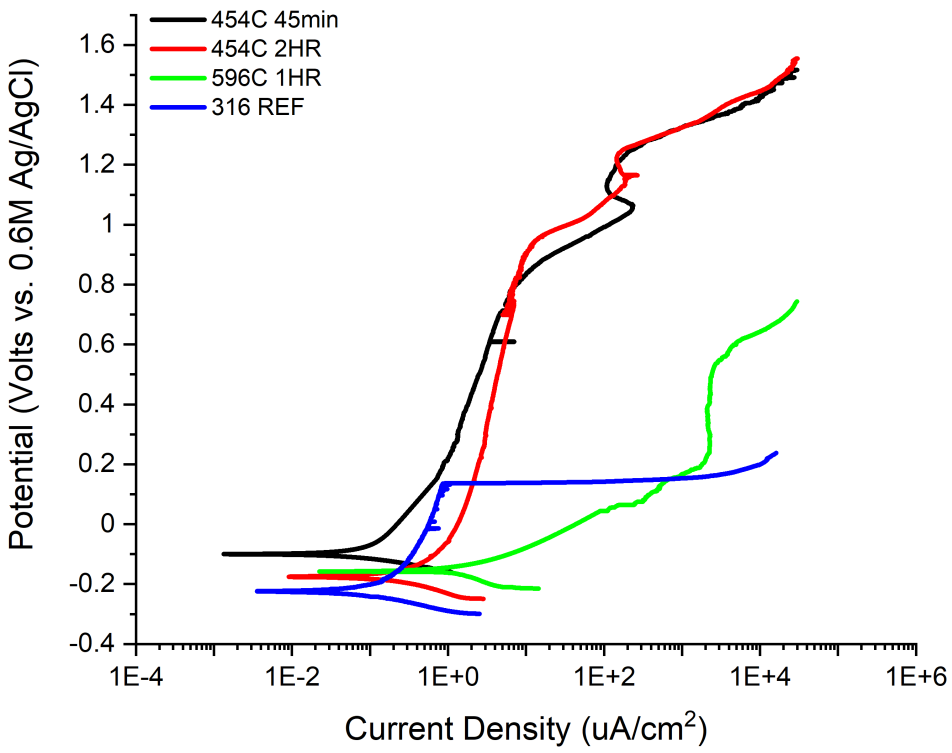

Figure 7.2: Potentiodynamic polarization curves of nitrided 316L with 3.5 wt% NaCl.

Figure 7.2 shows the polarization curves for 316L nitrided at 454 °C for 45 minutes, 454 °C for 2 hours and 596 °C for 1 hour. Compared to the unnitrided 316L, the E_{corr} increased in polarity for the nitrided samples. The calculated corrosion rates are shown in Fig. 7.3. The equivalent weights from EQN 2.7, EW, used for the calculation of corrosion rates were 25.91 and 23.79 for reference and nitrided samples, respectively. Two samples not shown in the polarization plot are included in the corrosion rate bar graph results. The samples nitrided at 425 °C for 2 hours and 511 °C for 1 hour polarization scans were stopped early and only measured the pre-Tafel region.

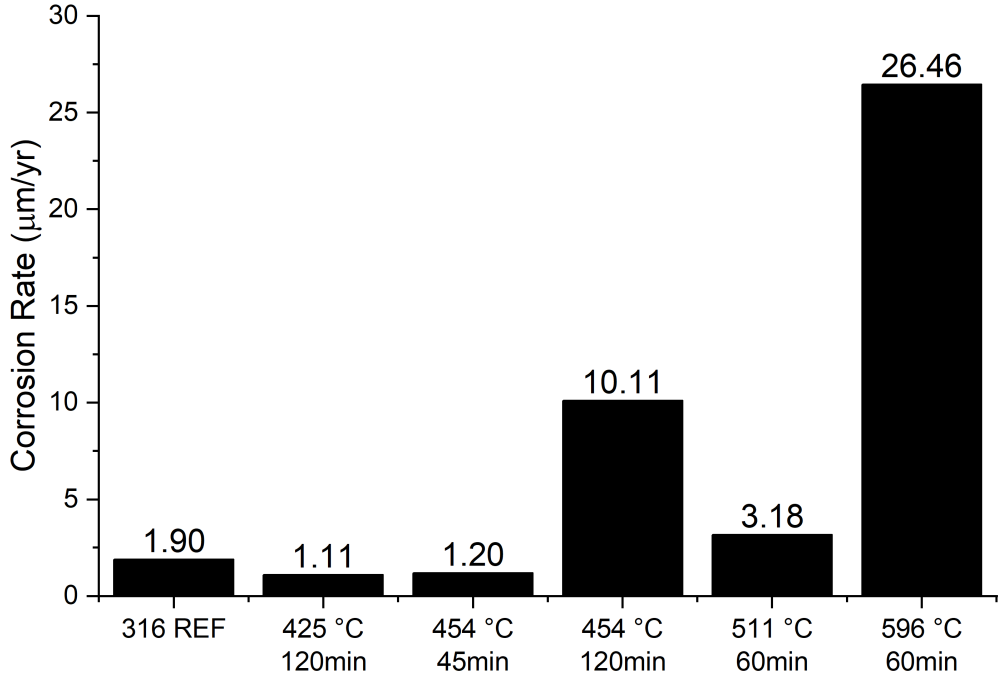

Figure 7.3: Graph of corrosion rates of nitrided 316L.

Nitridation improved the corrosion resistance for samples nitrided at 425 °C for 2 hours and 454 °C for 45 minutes. At the same temperature of 454 °C, increasing the nitridation time from 45 minutes to 2 hours reduced the corrosion resistance by a factor of 5. While the nitriding at 454 °C for 2 hours significantly increased the corrosion rate, nitriding at 511 °C for 1 hour only increased the corrosion rate by a factor of 1.5. As the improved corrosion resistance can mostly be contributed to the γ_N phase of 316, the temperature-time dependence of expanded austenite can be observed in the corrosion rates of nitrided 316L.

β_a (mV/dec)	β_c (mV/dec)	R_p $(kOhm/cm^2)$	E_{corr} (mV)	i_{corr} $(\mu A/cm^2)$
61.3 ±16.5	119 ±30	17.5 ±16.9	-631 ±17	1.56 ±1.02

Table 7.2: T91 reference potentiodynamic corrosion measurements in 3.5 wt% NaCl at 30 °C.

7.2 T91 Results and Discussion

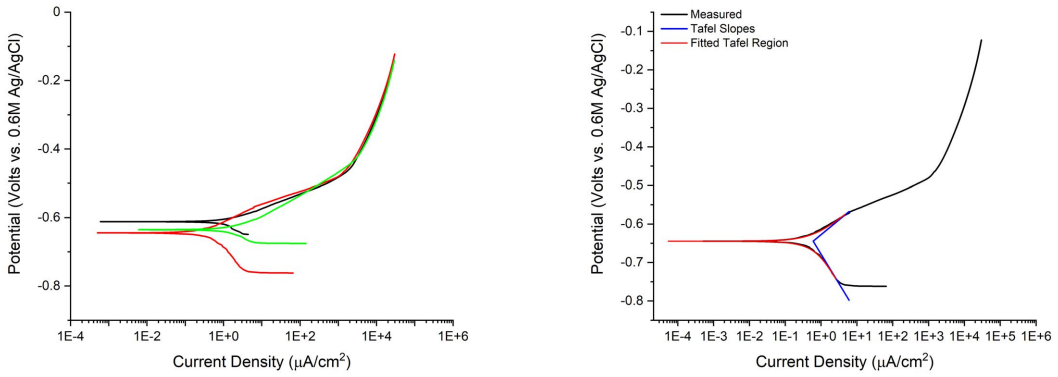

(a) (b)

Figure 7.4: T91 reference polarization curves.

Figure 7.4 shows the results of potentiodynamic polarization measurements of unnitrided T91 reference samples. Figure 7.4a contains all of the T91 corrosion measurements. Figure 7.4b shows calculated Tafel fitting and the associated Tafel slopes where the averaged measurements are shown in Table 7.2.

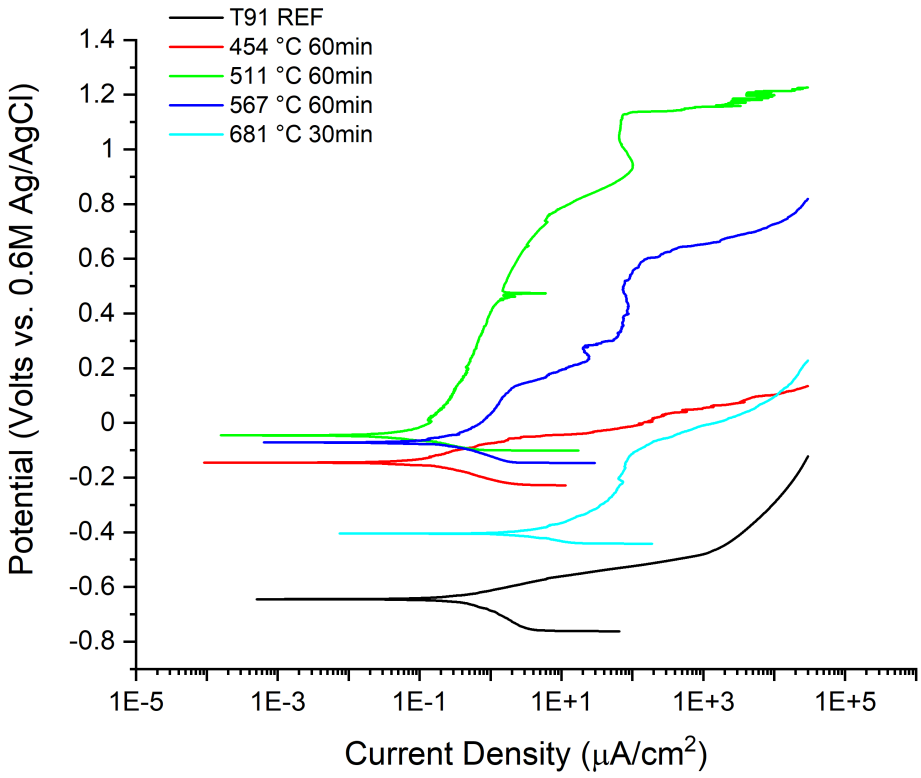

Figure 7.5: Potentiodynamic polarization curves of nitrided T91 with 3.5 wt% NaCl.

Figure 7.5 shows the polarization curves for T91 nitrided at 454, 511, and 567 and 681 °C for 30 minutes. Surface nitriding of T91 increased the E_{corr} potential for all samples. For T91 nitrided below 570 °C for 1 hour, the measured current density decreased compared to the reference samples. This decrease in current density can be seen in the calculated corrosion rates are shown in Fig. 7.6 where the corrosion rates suggest that nitriding T91 can significantly improve corrosion resistance at temperatures below 570 °C. The equivalent weight used for T91 calculation of corrosion rates was 24.64 for both reference and nitrided samples.

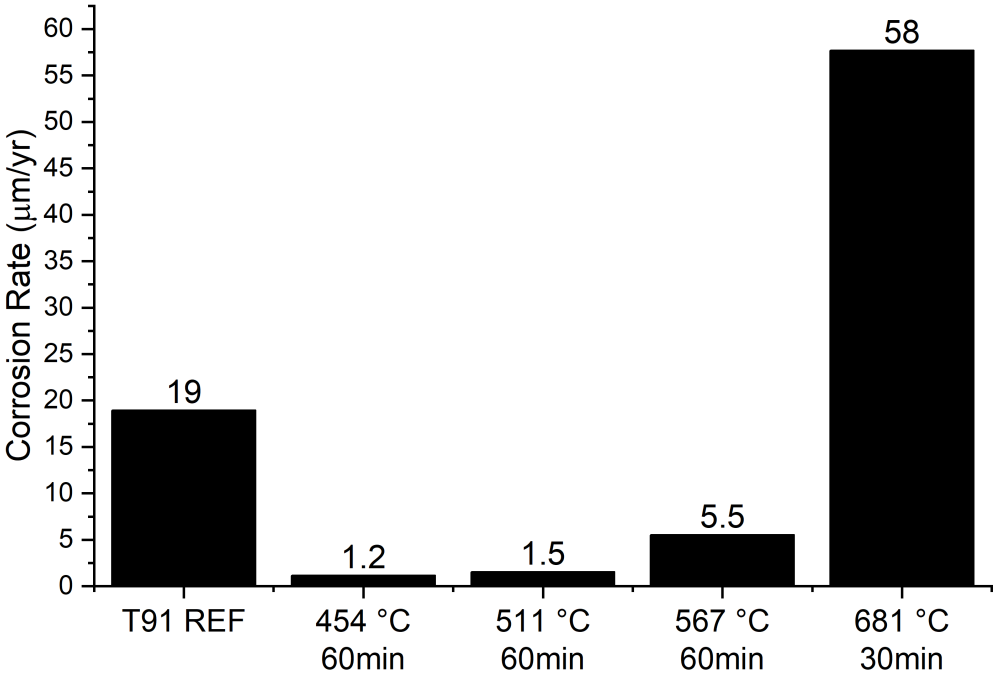

Figure 7.6: Graph of corrosion rates of nitrided T91.

β_a (mV/dec)	β_c (mV/dec)	R_p $(kOhm/cm^2)$	E_{corr} (mV)	i_{corr} $(\mu A/cm^2)$
113 ±14	221 ±25	9.1 ±0.6	-449 ±13	3.56 ±0.26

Table 7.3: HT-9 reference potentiodynamic corrosion measurements in 3.5 wt% NaCl at 30 °C.

7.3 HT9 Results and Discussion

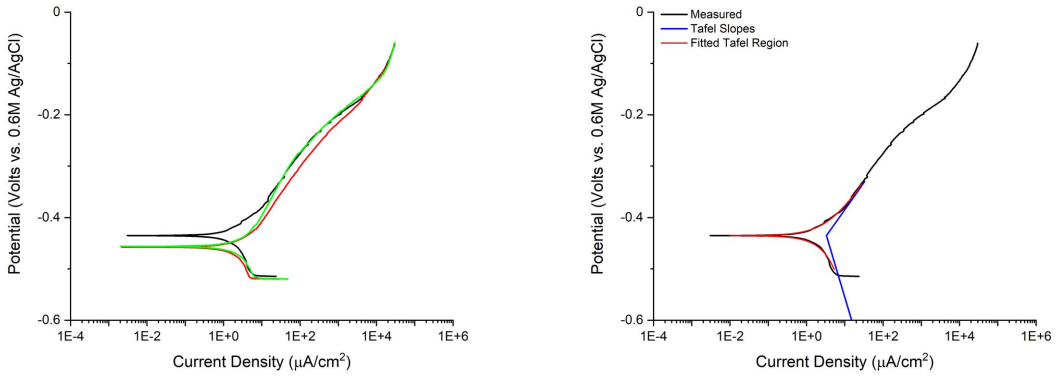

(a) (b)

Figure 7.7: HT9 reference polarization curves.

Figure 7.7 shows the results of potentiodynamic polarization measurements of unnitrided HT-9 reference samples. Figure 7.7a contains all of the HT-9 corrosion measurements. Figure 7.7b shows calculated Tafel fitting and the associated Tafel slopes where the averaged measurements are shown in Table 7.3.

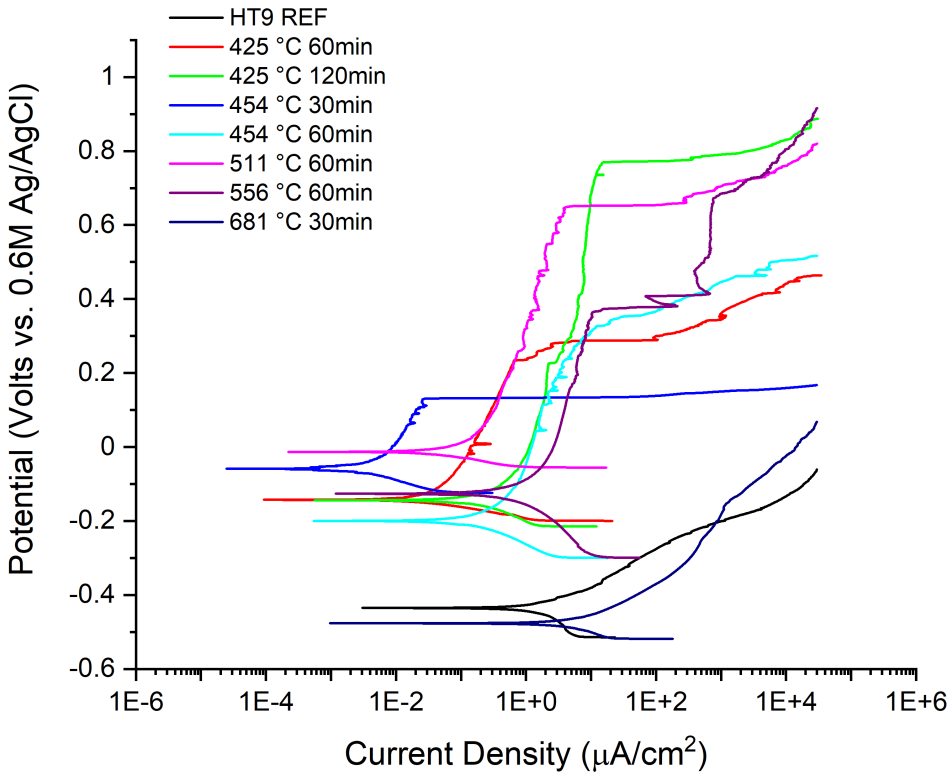

Figure 7.8: Potentiodynamic polarization curves of nitrided HT-9 with 3.5 wt% NaCl.

Figure 7.8 shows the polarization curves for HT9 nitrided at temperatures between 425 and 681 °C for 30 minutes to 2 hours. Surface nitriding of HT9 increased the E_{corr} potential for all samples except the 681 °C sample. As with T91, HT9 nitrided below 570 °C for 1 hour resulted in decreased current densities and correlated corrosion rates, shown in Fig. 7.9. The corrosion rates calculations for HT9 used an equivalent weight of 25.91 for both reference and nitrided samples.

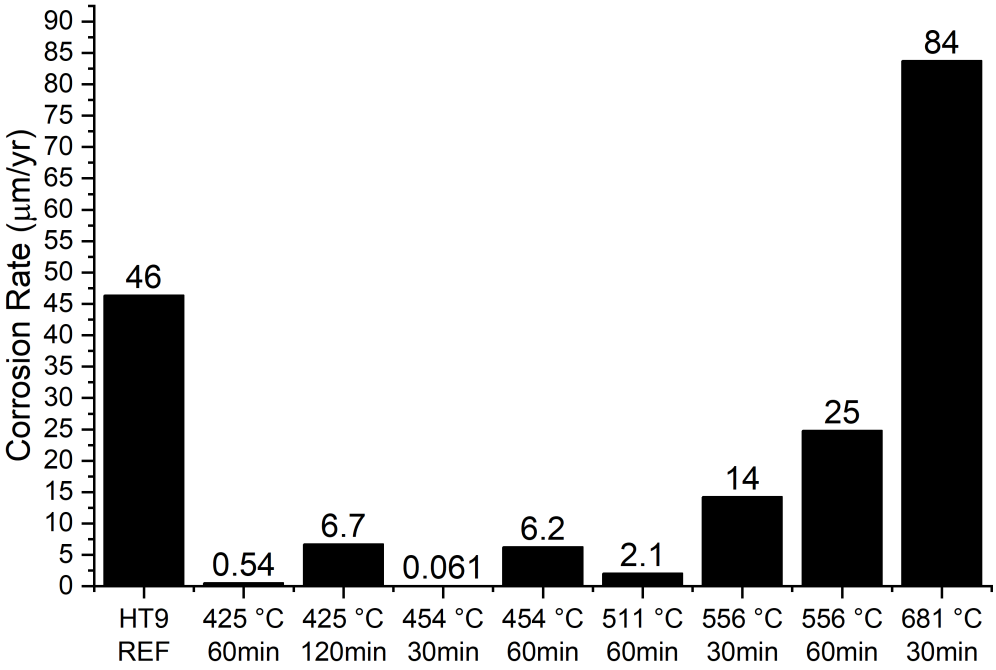

Figure 7.9: Graph of corrosion rates of nitrided HT-9.

β_a (mV/dec)	β_c (mV/dec)	R_p $(kOhm/cm^2)$	E_{corr} (mV)	i_{corr} (nA/cm^2)
451 ±16.5	187 ±22	250 ±14	-435 ±30	229 ±6

Table 7.4: Zircaloy-4 reference potentiodynamic corrosion measurements in 3.5 wt% NaCl at 30 °C.

7.4 Zircaloy-4 Results and Discussion

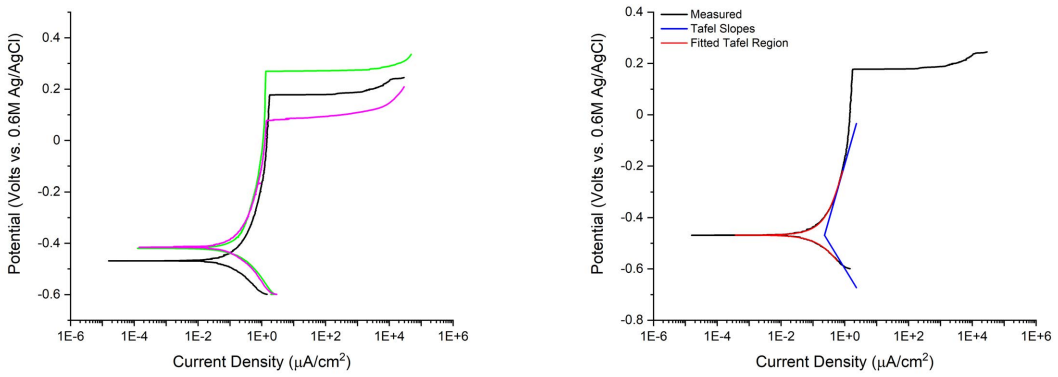

(a) (b)

Figure 7.10: Zircaloy-4 reference polarization curves.

Figure 7.10 shows the results of potentiodynamic polarization measurements of unnitrided Zircaloy-4 reference samples. Figure 7.10a contains all of the Zircaloy-4 corrosion measurements. Figure 7.10b shows calculated Tafel fitting and the associated Tafel slopes where the averaged measurements are shown in Table 7.4.

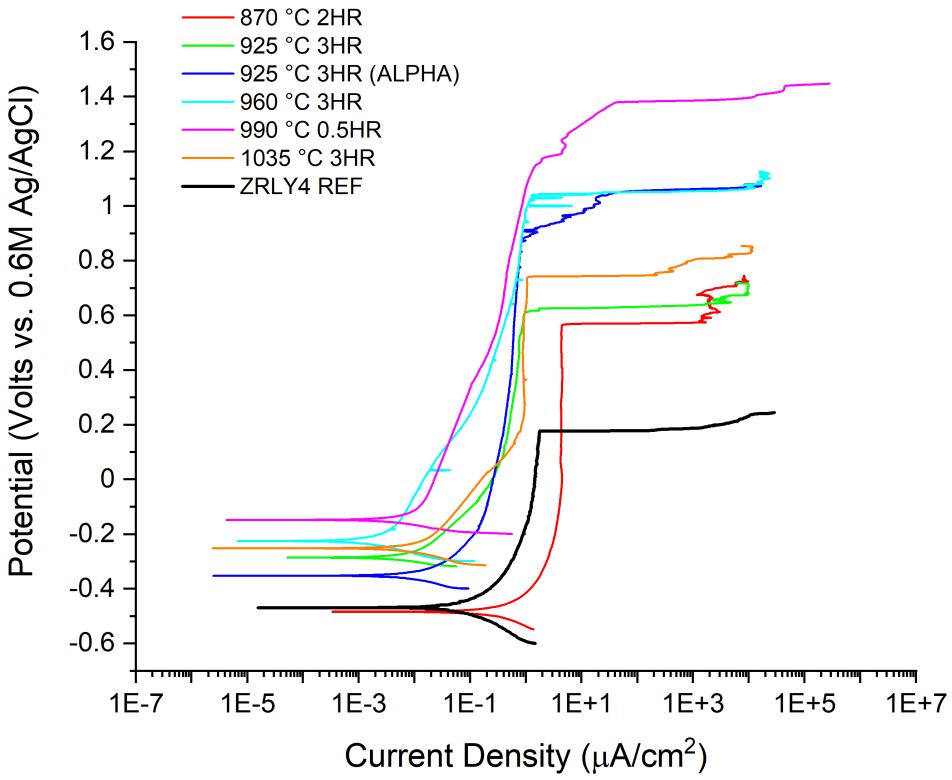

Figure 7.11: Potentiodynamic polarization curves of nitrided Zircaloy-4 with 3.5 wt% NaCl.

Figure 7.11 shows the polarization corrosion curves for nitrided Zircaloy-4. For all Zircaloy-4 samples except the 870 °C, the surface potential became more positive and the current densities decreased. The calculated corrosion rates, where the equivalent weight was 20.44, are shown in Fig. 7.12. The corrosion rate axis was plotted with break due to the high corrosion rate of the 870 °C sample which had a corrosion rate of 10.55 µm/yr. All other nitrided Zircaloy-4 samples corrosion rates were significantly reduced.

To investigate the corrosion properties of the α-$ZrN_{x<0.46}$ nitrogen modified layer,

a sample nitrided at 925 °C for 3 hours was polished to remove the thin δ-ZrN surface layer. As the bulk of the modified nitrogen layer consists of α-$ZrN_{x<0.46}$, it was of interest to measure the corrosion properties of the under lying layer. As can be seen in Fig. 7.12, the corrosion rate for the polished 925 °C samples with the α-$ZrN_{x<0.46}$ exposed had the highest corrosion rate of the samples nitrided above 870 °C. Though the corrosion resistance decreased after removing the δ-ZrN layer, it still increased by almost a factor of 10 compared to the unnitrided reference sample.

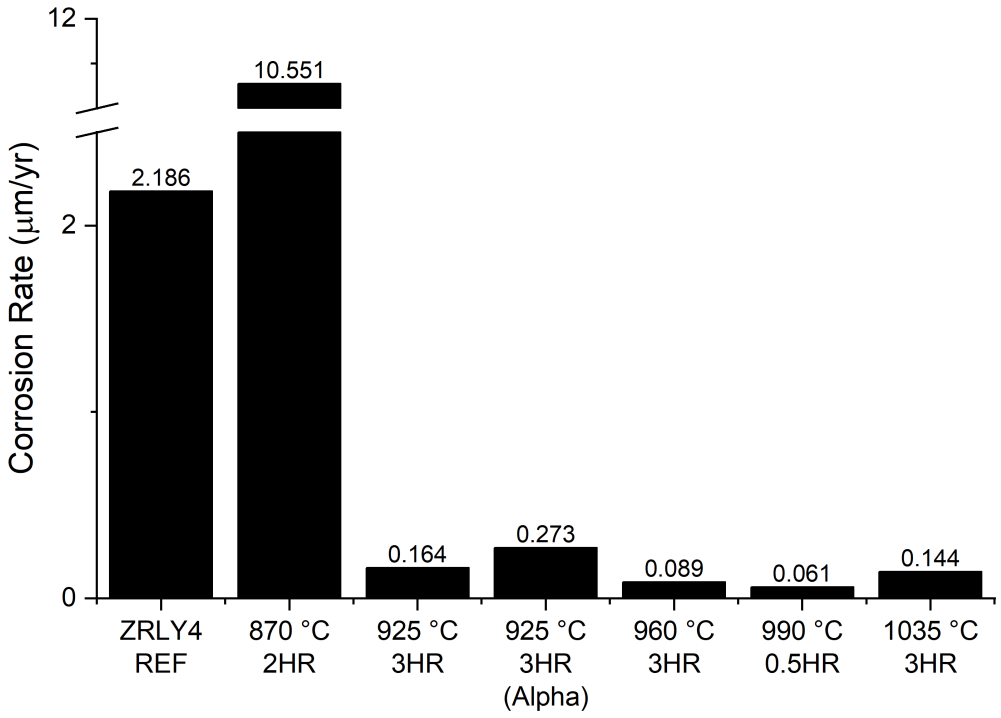

Figure 7.12: Graph of corrosion rates of nitrided Zircaloy-4.

The reduced corrosion resistance of the 870 °C may be caused by the formation

of Zr_3N_4 which has a blue color or ZrN_2 [118, 132, 133, 134]. The associated nitrided sample set shown in Fig. 7.13 appear to have a maroon color. As can be seen in the background of Fig. 7.13b, the zirconium base plate that was used multiple times had been nitrided to dark maroon. The red box in the lower right corner is an image centered on the nitrided base plate to zirconium cage contact area where the left side was inside the cathodic cage. The color of the nitrided base plate external to the cage appears to be a dark purple or blue color and measured to have a nitrogen concentration of approximately 66 at.%. Based on the surface EDS nitrogen concentration of approximately 60 at.% and the maroon color of the 870 °C sample, the poor corrosion resistance may be due to the formation of metastable hyperstoichiometric nitride on the sample's surface. It should be noted that the maroon color only occurred in this temperature range, as it was not observed at lower or high nitriding temperatures.

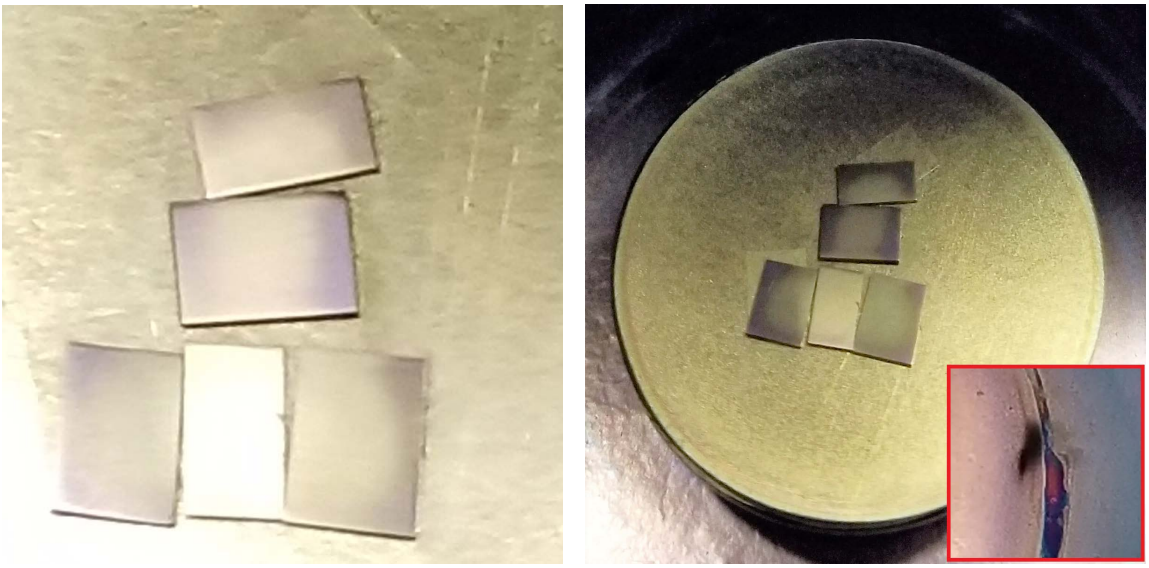

(a) (b)

Figure 7.13: Surface images of nitrided Zircaloy-4 at 870 °C for 2 hours.

7.5 Conclusion

The corrosion resistance in 3.5 wt% NaCl varied for all nitrided materials dependent on nitriding temperature and time. The corrosion rate of nitride 316L had the least improvement where the reference sample measurement was 1.9 µm/yr and nitrided sample at 454 °C for 45 minutes was 1.2 µm/yr. At higher temperatures and longer nitriding durations, the corrosion resistance was reduced. Nitriding of T91 and HT-9 significantly enhanced corrosion resistance for nitriding temperatures below 570 °C. The corrosion rate of nitrided Zircaloy-4 decreased by an order of magnitude for all samples above 920 °C.

For all these samples, we have the following general observations:

- The value of the corrosion potential (also called Open Circuit potential) is higher for the nitrided samples. This means that a higher potential is necessary to corrode Zircaloy-4 with surface nitration. This is a good thing since it shows that your material has a higher range of potential where it is noble

- The corrosion current densities around the OCP potential are a few orders of magnitude lower for your nitrided samples compared to the bare sample. This is also good as it means that the anodic current is reduced with the surface treatment, so the sample will corrode less quickly.

- The breakdown potential is also increased in the nitride samples which means that your surface modification is more adherent/resistant than the zirconium oxide.

These results are very typical of a protective coating or surface modification.

8. EFFECTS OF NITRIDATION ON MICROSTRUCTURE

A systematic nitridation on Zircaloy-4 and stainless steel 316L as a function of pressure, temperature, and nitridation time was carried out. Figure 8.1 shows an image of nitridation on Zircaloy-4 when the device was under operation. After the nitridation, scanning electron microscopy (SEM) and transmission electron microscopy (TEM) were used to characterize microstructures. Localized diffraction pattern analysis was performed to identify phases.

Figure 8.1: Image of the plasma nitridation device in operation.

8.1 316

The microstructural changes of 316L after the nitridation were systematically studied. Figure 8.2* shows Fe-N phase diagram [63]. The most frequently observed nitride phases include Fe_2N and Fe_4N. Figure 8.3 shows SEM images of a typical cross-section of nitrided 316L after fine polishing. Nitridation was performed at 596 °C for 2 hours with a pressure of 1.5 Torr. There was a visually distinctive layer on the surface, which is about 50 µm deep. Using the FIB technique, a TEM lamellea was extracted and its microstructure characterized, as shown in Fig. 8.3.

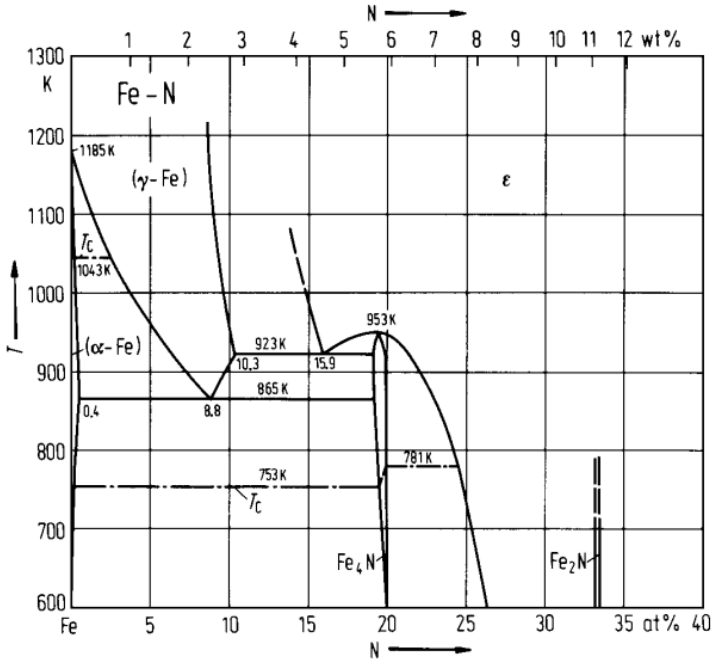

Figure 8.2: Fe-N phase diagram. Used with permission of Springer, from Fe-N (Iron-Nitrogen), Predel, B., 5, 1994; permission conveyed through Copyright Clearance Center, Inc. [63]*.

*[63] Used with permission of Springer, from Fe-N (Iron-Nitrogen), Predel, B., 5, 1994; permission conveyed through Copyright Clearance Center, Inc.

Used with permission of Springer, from Fe-N (Iron-Nitrogen), Predel, B., 5, 1994; permission conveyed through Copyright Clearance Center, Inc.

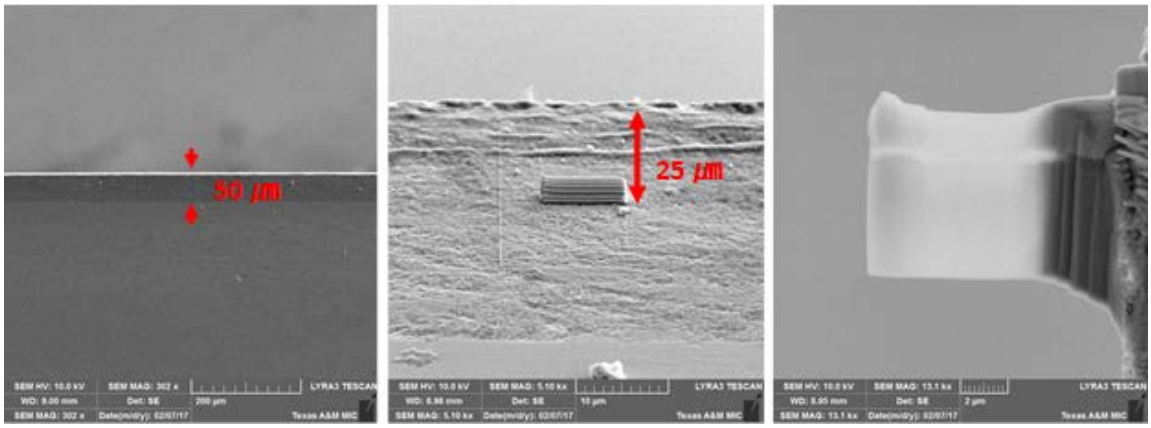

Figure 8.3: SEM FIB images of nitrided 316L for TEM analysis. Nitriding was performed at 596 °C for 2 hours with a pressure of 1.5 Torr. (left) the cross sectional view after fine polishing; (center) Pt deposition prior to FIB lift out and (right) the TEM specimen after FIB.

8.1.1 Results and Discussion

Figure 8.4 shows the cross-sectional TEM micrographs of nitrided 316L. There is a highly polycrystalline layer near the surface region, about 1 µm deep, which had a grain size less than 100 nm. High-resolution TEM shows that this layer is a highly distorted Fe_2N layer. Beneath this layer is a continuous layer of relatively larger grains. Image on the right side of Fig. 8.4 refers to enlarged microstructures of the red and yellow marked boxes, which corresponds to the near-surface highly polycrystalline layer and bottom coarse-grained layer.

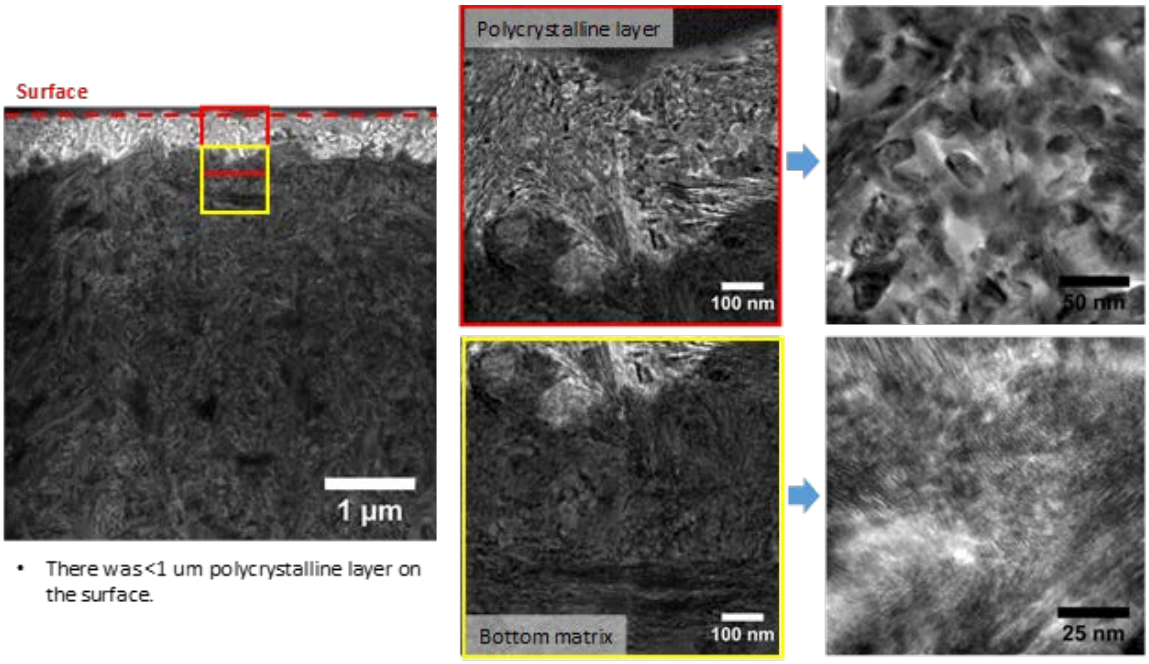

Figure 8.4: Cross-sectional TEM images of nitrided 316L, featured with a highly polycrystalline layer as marked by the red box, and a relatively coarse-grained layer as marked by the yellow box. The right side figures are localized images from the red and yellow marked regions.

Localized diffraction analysis of both near surface region and deep region shows both layers are Fe_2N. The left side of Fig. 8.5 is the measured reciprocal spacing, and the right side is the indexed d-spacing. The indexed d-spacing is slightly different from the measured value, due to possible lattice distortion, but all other unindexed peripheral do spacing match very well with expected Fe_2N spacing. On the other hand, the measured d-spacing does not match with CrN, Cr_2N, Fe_3N, and Fe_4N.

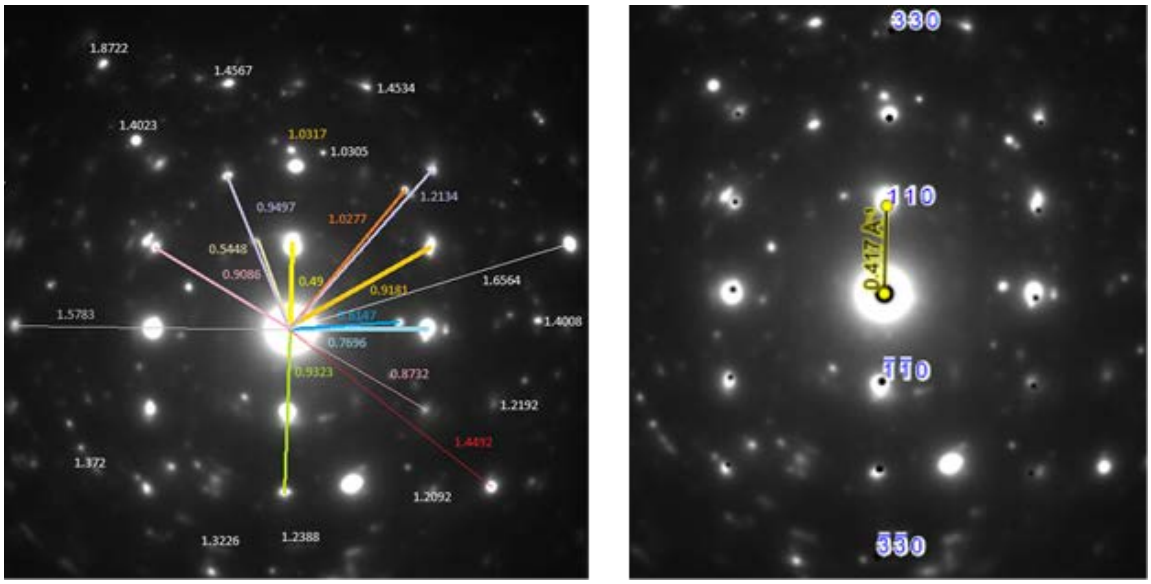

Figure 8.5: (Left) measured reciprocal spacing and (right) the indexed d-spacing from a diffraction pattern obtained from the near surface region.

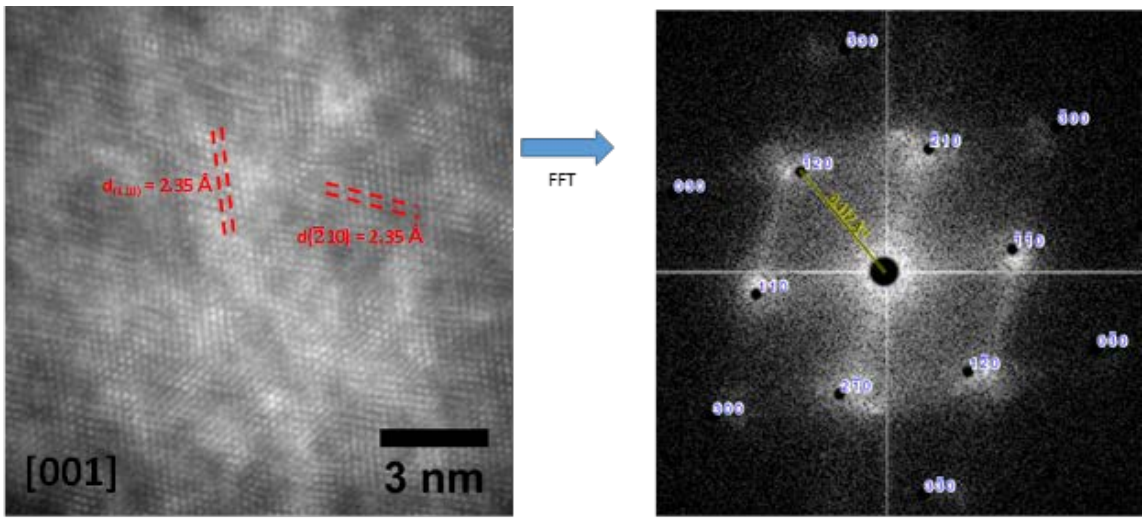

Figure 8.6: (Left) high-resolution TEM image and (right) corresponding FFT image, obtained from the near surface region.

Figure 8.6 shows high-resolution TEM image obtained from the near surface region. The lattice spacing, 0.235 nm along (110) and (210), agrees well with Fe_2N phase. The interplanar spacing from the FFT image further shows good agreements with Fe_2N phase.

8.2 Zircaloy-4

Zirconium nitride has a cubic structure with a lattice constant of 0.45675 nm. It has a melting point as high as about 3000 °C. Figure 8.7* shows Zr-N phase diagram [14]. At low N concentrations, a mixture of α-Zr and ZrN_x particles co-exist in the matrix. With increasing N concentrations, continuous ZrN_x film start to form. At higher N concentrations, additional N atoms are dissolved in the matrix. These supersaturated N atoms can diffuse either deeply into the matrix or away from the surface. In order to obtain nitride layers with good stability, annealing is required during the nitridation for sufficient thermal diffusion and bond reconfiguration.

*[14] Used with permission of Springer Nature BV, from The N-Zr (Nitrogen-Zirconium) System, L. Gribaudo, D. Arias, and J. Abriata, 15(4), 1991; permission conveyed through Copyright Clearance Center, Inc.

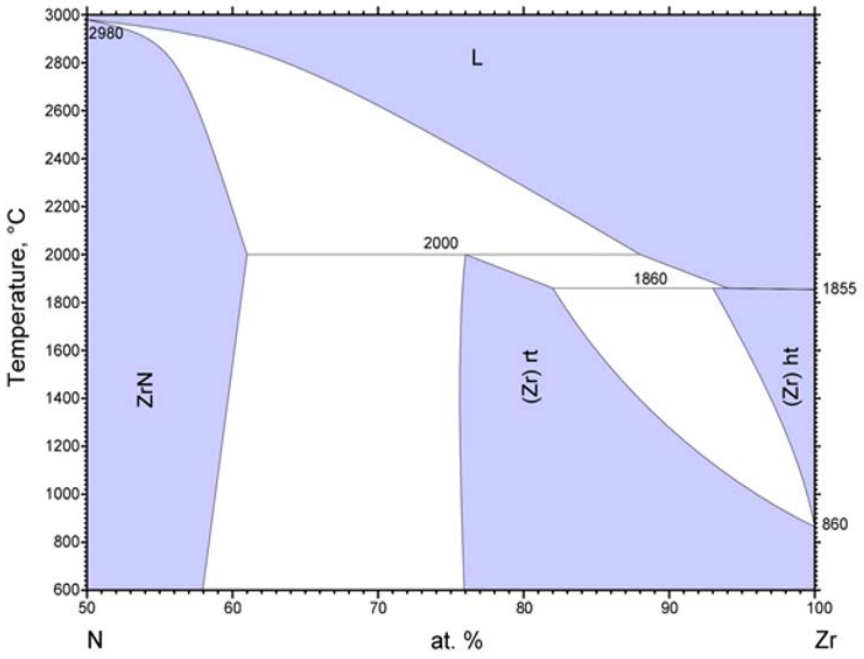

Figure 8.7: Phase diagram of Zr-N system. Used with permission of Springer Nature BV, from The N-Zr (Nitrogen-Zirconium) System, L. Gribaudo, D. Arias, and J. Abriata, 15(4), 1991; permission conveyed through Copyright Clearance Center, Inc. [14]*.

8.2.1 Results and Discussion

Figure 8.8 compares the SEM surface images of a control Zircaloy-4 sample (left) and a nitrided Zircaloy-4 sample at floating potential (right). The nitridation temperature, time, and pressure are 511 °C, 1 hour and 1500 mTorr, respectively. After plasma nitridation, the sample surface became relatively rough due to cage deposition on the surface. Figure 8.9 shows the surface morphology of a nitrided Zircaloy-4 sample at 700 °C and 1500 mTorr for24 hours. No contamination was observed, and the nitriding was uniform over the specimen surface.

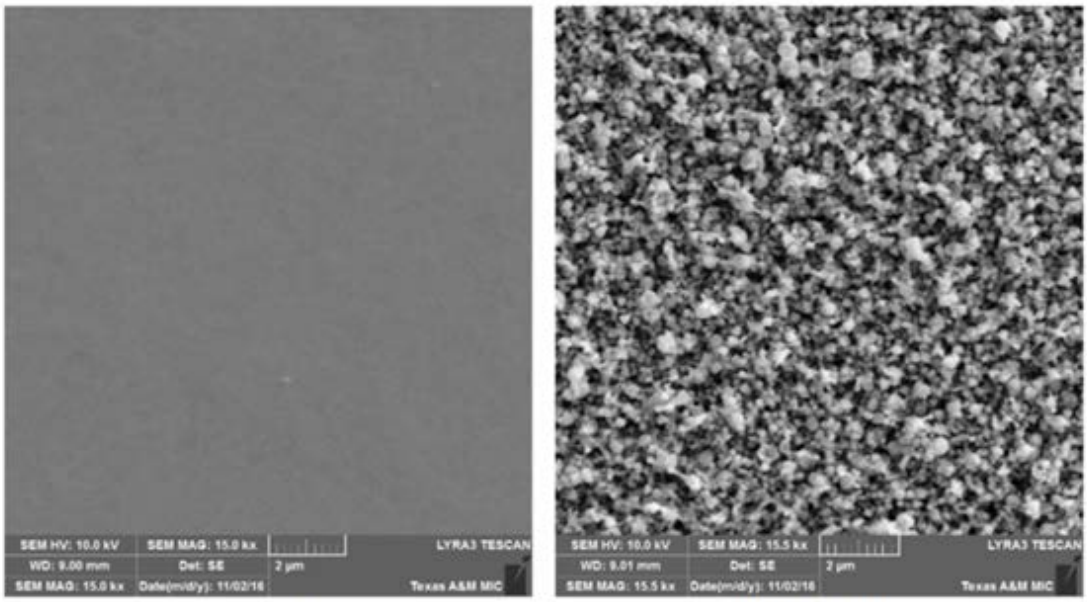

Figure 8.8: SEM surface images of control Zircaloy-4 (left) and nitrided Zircaloy-4 floated (right).

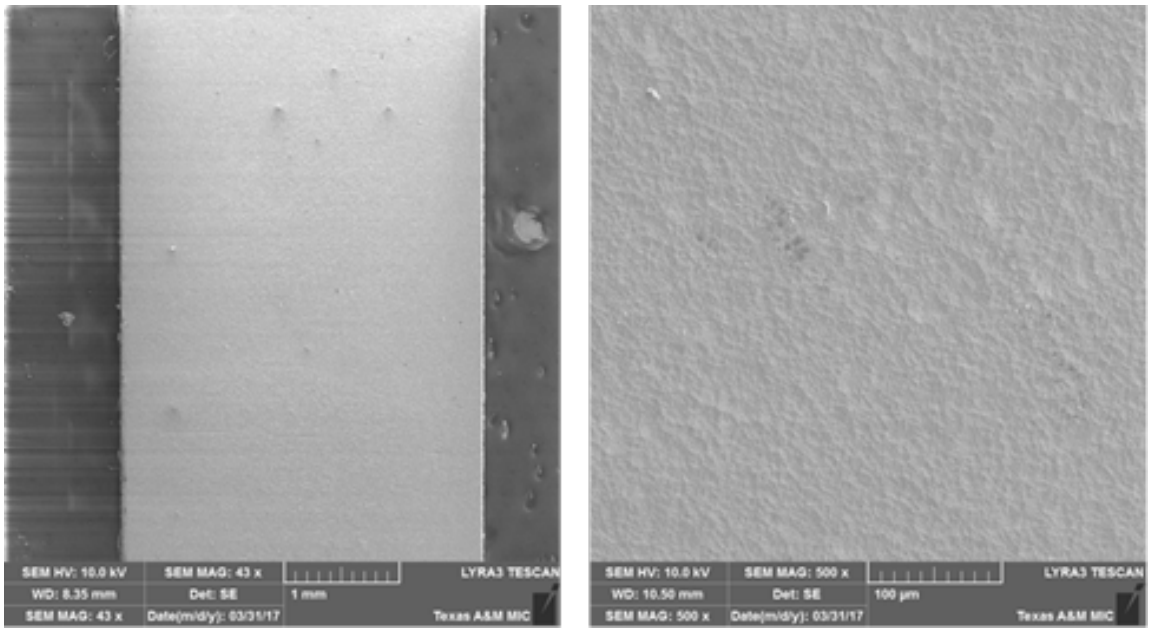

Figure 8.9: SEM suface images of Zircaloy-4 nitrided at 700 °C for 24 hours with bias.

Focused-ion-beam (FIB) technique was used to prepare TEM specimens by using 5-30 keV Ga beam. The 30 keV Ga beam was first used for cutting and lift-out, following by 5 keV Ga beam with a lower beam current for the final stage of specimen thinning to a thickness of 50 to 200 nm. Figure 8.10 shows SEM images of the nitrided surface and FIB-prepared trench for a lift out of a TEM specimen.

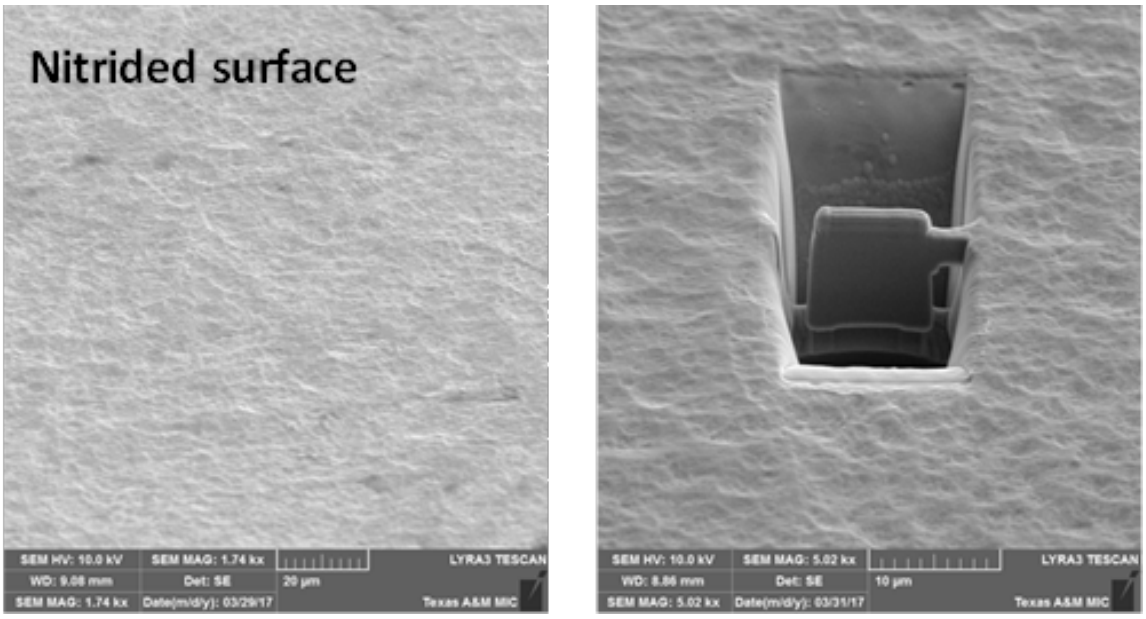

Figure 8.10: SEM images of the nitrided Zircaloy-4 surface before and after FIB trenching for TEM specimen preparation.

Figure 8.11* shows the cross-sectional TEM image of the nitride sample. In the near-surface region, about 0.5 µm deep, there is a continuous polycrystalline layer with lamellar like grains. Localized diffraction pattern shows lattice distance matches with [111], [220] and [131] of cubic ZrN phase. In the region beneath the surface polycrystalline layer, as shown in Fig. 8.12*, the localized diffraction pattern shows lattice spacing corresponding to a HCP Zr structure.

*[64] Reprinted with permission from "ZrN Phase Formation, Hardening and Nitrogen Diffusion Kinetics in Plasma Nitrided Zircaloy-4" by Robert Balerio, Hyosim Kim, Andres Morell-Pacheco, Laura Hawkins, Ching-Heng Shiau, and Lin Shao, 2021. Materials, 14(13), 3572, Copyright 2021 by MDPI.

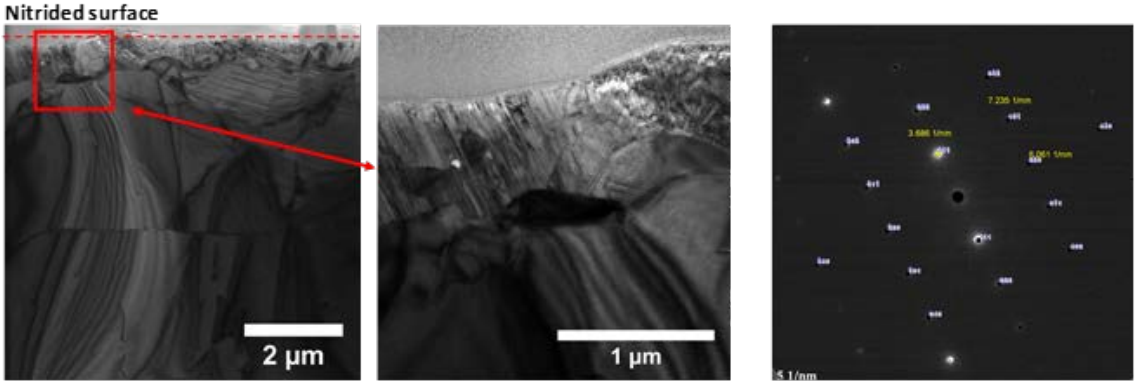

Figure 8.11: Cross sectional TEM micrographs of nitrided Zircaloy-4 and localized diffraction pattern obtained from the near surface region. Reprinted with permission from [64]*.

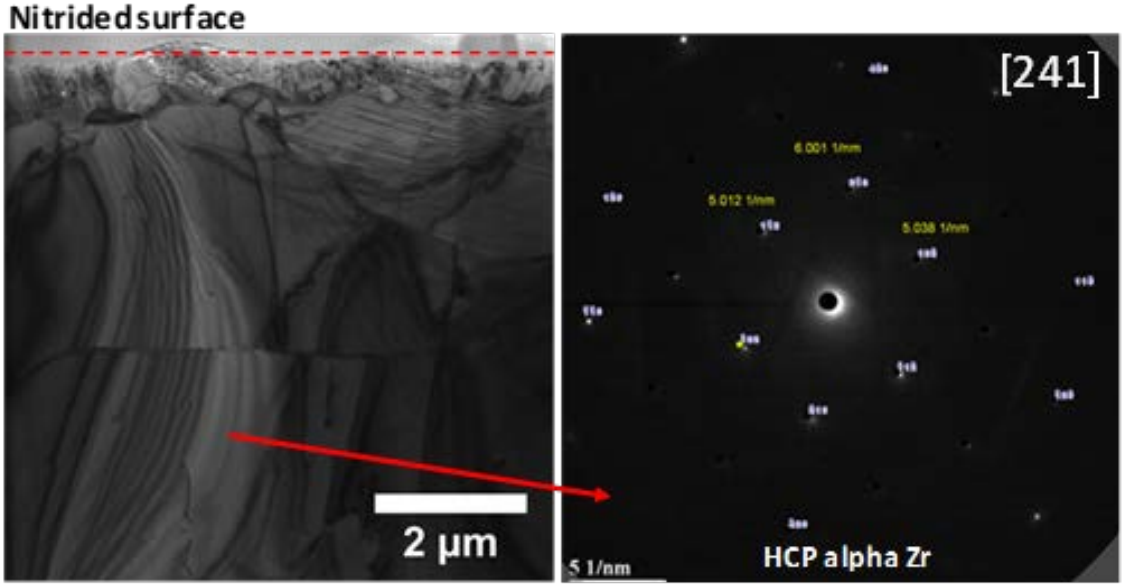

Figure 8.12: Cross sectional TEM micrographs of nitrided Zircaloy-4 and localized diffraction pattern obtained from a deep region away from the surface. Reprinted with permission from [64]*.

Figure 8.13 shows two additional high-resolution TEM images and their corresponding FFT images in the near surface region. Both interplanar spacing and FFT images do not match with Zr, ZrN or Zr_3N_4. They can be distorted ZrN phase in a highly defective zone.

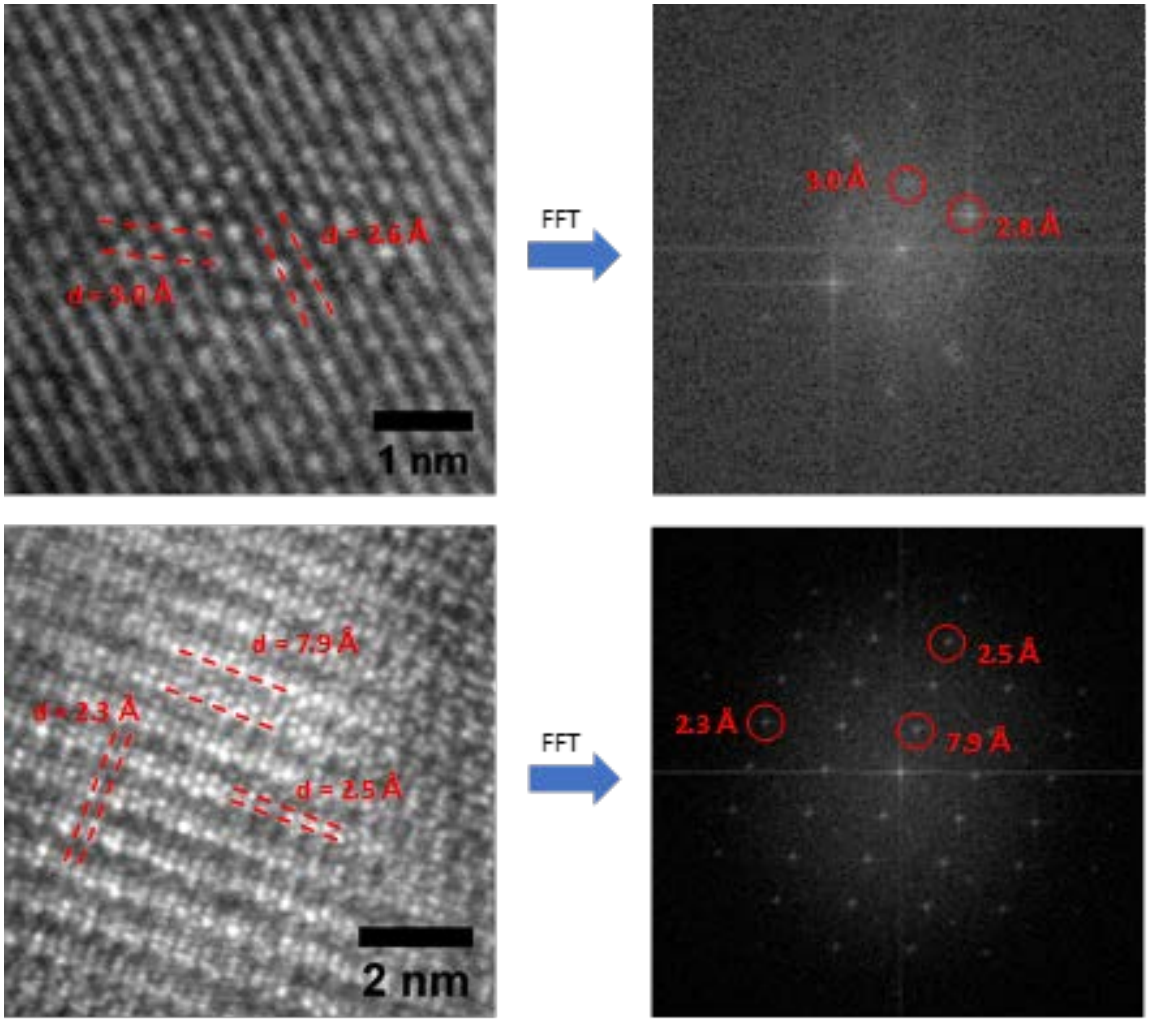

Figure 8.13: High-resolution TEM image of nitrided Zircaloy-4 in the near-surface region (left) and a localized diffraction pattern.

8.3 Conclusion

Through systematical nitridation and structural characterization, we have shown that nitridation can form continuous nitride layers. For 316L and Fe-based stainless steels, the hardening layers corresponded to the nitrided layers. For Zr and Zircaloy-4, the hardening layer was deeper than the nitride layer and is correlated to N enriched layer even when a δ-ZrN nitride phase is not developed.

9. ION IRRADIATION*

The irradiation response of nitrided stainless steels was studied. Considering the importance of 316 stainless steels in both LWR and fast reactor applications, 316L was selected for this study. The study consisted of three steps. Firstly, 316L was nitrided to form a surface nitride layer. Then the nitrided sample was cut and the nitrided cross-section was polished and irradiated using 3.5 MeV Fe ions to 50 peak dpa at 600 °C. Next, focused ion beam was used to prepare lamellae specimens from different locations of the cross section. Lastly, transmission electron microscopy was used to characterize void swelling. The study showed that surface nitrided layer had the highest swelling resistance, without observations of any voids. Beneath the surface nitride layer, there was a nitrogen rich layer, where only a few voids were observed. In contrast, for the deep region that corresponded to the bulk material without nitridation, high density voids appeared. The study suggests that nitridation can improve swelling resistance.

9.1 316L

As the first step, 316L was nitrided at 800 °C for 10 hours. The biased voltage between the grounding plate (positioned 7 cm above the top of the cage) and the nickel cathodic cage was 650 volts. The sample holder inside the cage was connected to the sample stage resulting in the sample and the cage being at the same potential.

*[65] Figures in this chapter are reprinted with permission from Journal of Nuclear Materials, 540, Andres Morell-Pacheco, Hyosim Kim,Tianyao Wang, Ching-HengShiau, Robert Balerio, Adam Gabriel, and Lin Shao, Ni coating on 316L stainless steel using cage plasma treatment: Feasibility and swelling studies, Pages 152385, Copyright (2020), with permission from Elsevier. Reprinted from The Lancet, Vol. 540, Andres Morell-Pacheco, Hyosim Kim, Tianyao Wang, Ching-HengShiau, Robert Balerio, Adam Gabriel, and Lin Shao, Ni coating on 316L stainless steel using cage plasma treatment: Feasibility and swelling studies, 152385, Copyright (2020), with permission from Elsevier.

The gas used was a mixture of 90 at. % nitrogen and 10 at.% hydrogen. The pressure during the nitridation is 1.5 Torr. After the plasma was ignited, both the pressure and voltage were slowly increased to the operation setup.

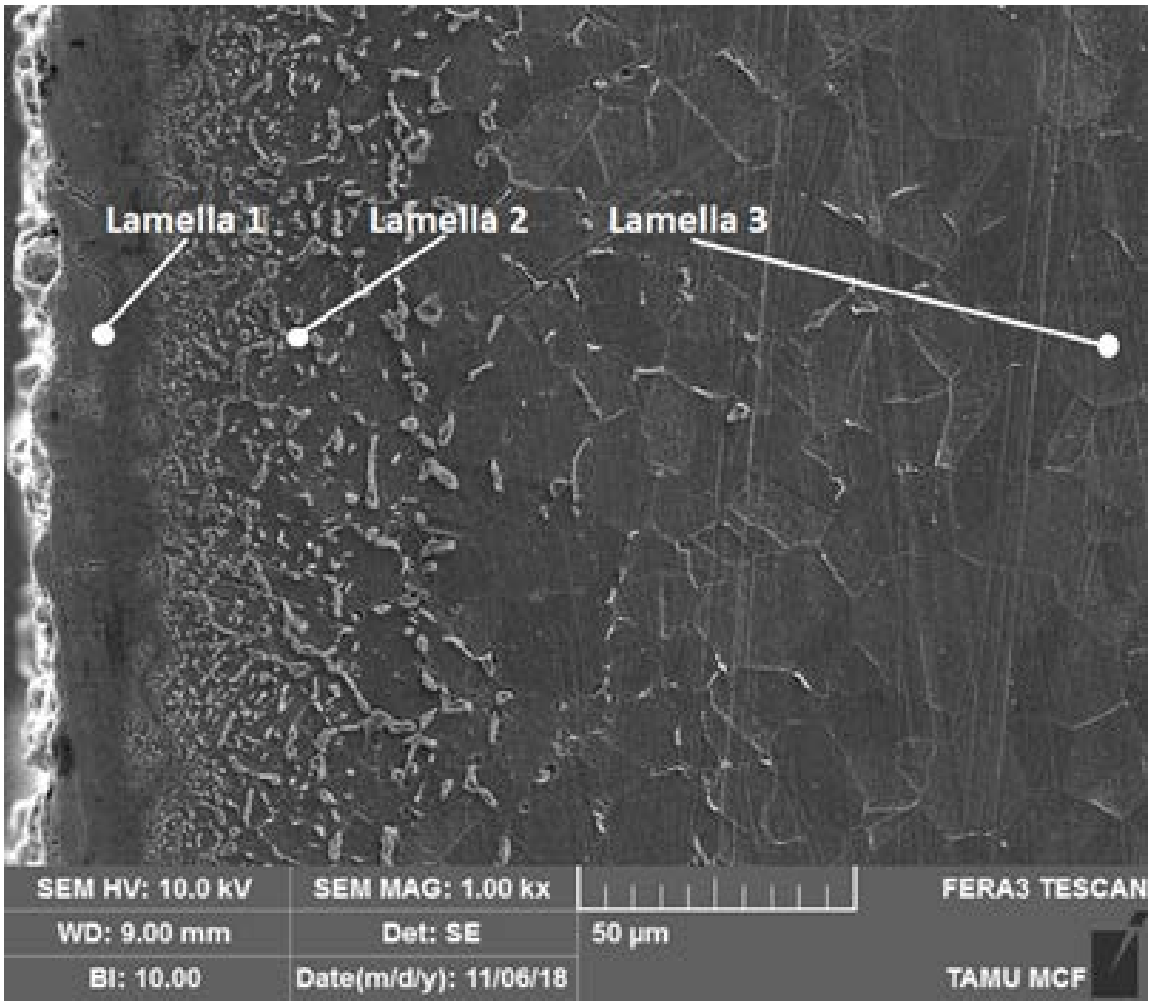

Figure 9.1: SEM image of ion irradiated cross section of the nitrided 316L. Three points marked correspond to the location of FIB lift outs for TEM specimen preparation after the irradiation. Modified with permission from [65]*.

The nitrided sample cross section was polished and etched using Marble's etchant. Figure 9.1* shows the SEM image of the cross section [65]. Three points are marked

as lamella 1, 2, and 3, which correspond to the FIB lift-out locations for the following TEM specimen preparation after ion irradiation. Position 1 corresponds to the nitride layer of about 25-30 µm. Position 2 corresponds to a nitrogen rich layer affected by surface nitrogen diffusion. This layer was about 70 µm thick. Both nitrided layer and nitrogen rich layers had enhanced hardness. Position 3 corresponds to bulk region, which was not affected by nitridation.

The cross section of the nitrided sample was uniformly irradiated by using 3.5 MeV Fe ions to 50 peak dpa at 600 °C. SRIM code utilizing the KP model was implemented for dpa calculation, with Fe displacement energy set to 40 eV. The ion irradiation was performed by using a defocused beam. The technique of multiple-beam-deflection was applied to avoid carbon contamination.

9.1.1 Results and Discussion

For the nitride layer region (as marked by the point in Fig. 9.2a)*, there are no voids observed [65]. Figure 9.2b* shows the TEM image [65]. The surface did not show any elongated grains, which suggest that the acid etch successfully removed the deformation zone from the cross sectional polishing. In other words, cold work and deformation did not play role in swelling behaviors. Figure 9.2c-f* show TEM images of different locations from the region in Fig. 9.2a* [65]. Figure 9.2c* shows a twin boundary [65]. Figure 9.2d* show a few small grains on the surface [65]. Figure 9.2e* and 9.2f* show two large grains [65]. The absence of voids in any of these regions suggests that the surface nitride layer has excellent swelling resistance.

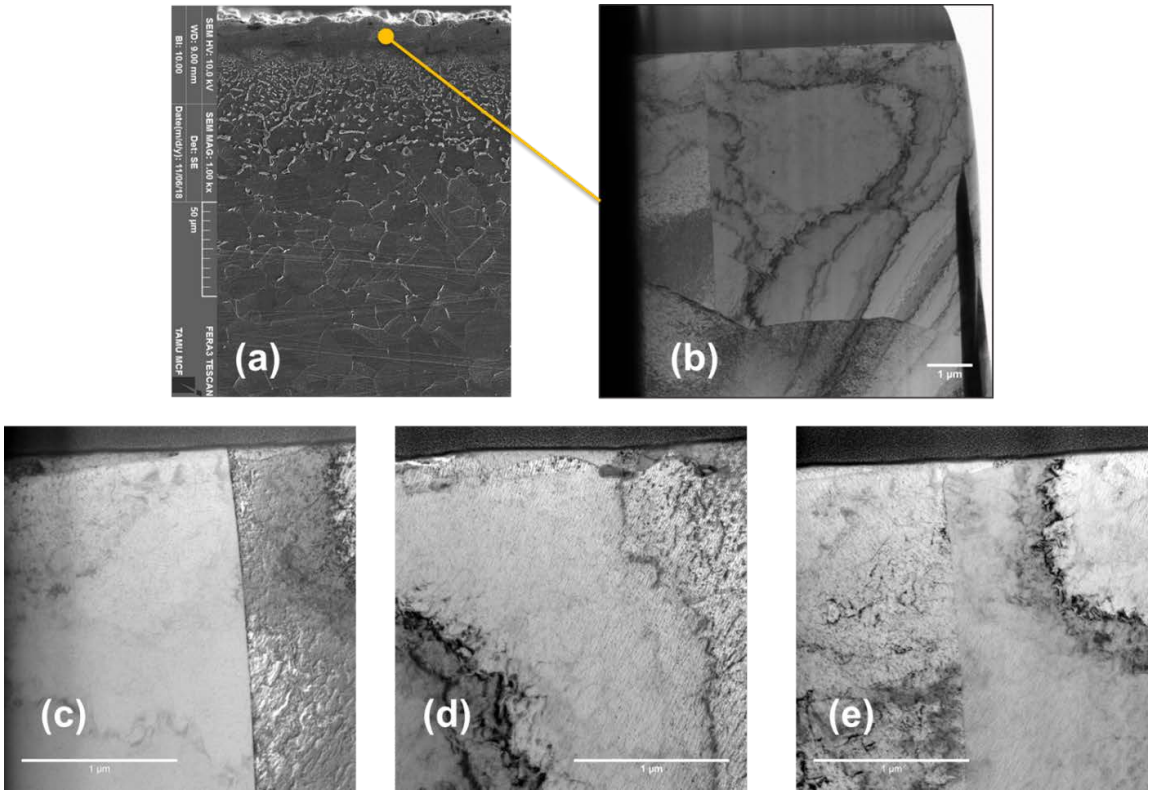

Figure 9.2: Images of TEM analysis of irradiated surface nitride layer. (a) SEM image of the cross sectional of nitrided 316L and position of the FIB lift out for TEM characterization, (b-e) cross sectional TEM images of the irradiated sample. Reprinted with permission from [65]*.

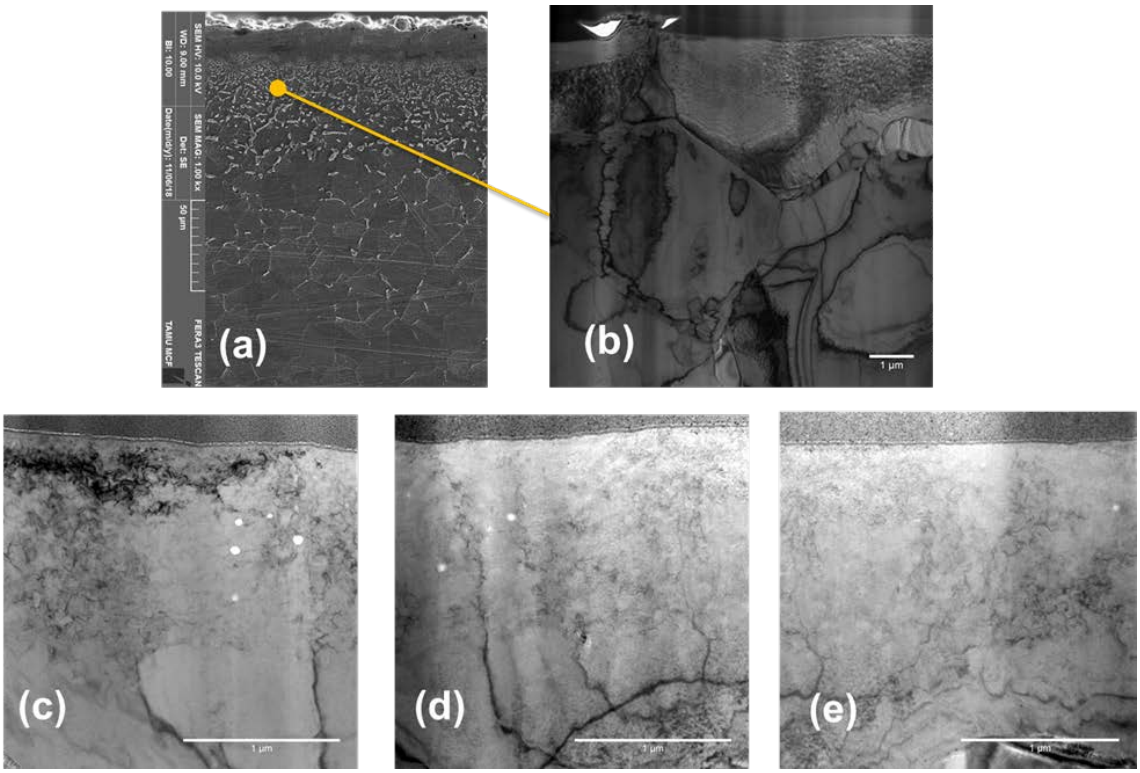

Figure 9.3: Images of TEM analysis of irradiated intermediate nitride layer. (a) SEM image of the cross sectional of nitrided 316L and position of the FIB lift out for TEM characterization, (b-e) cross sectional TEM images of the irradiated sample. Reprinted with permission from [65]*.

The nitrogen rich layer corresponding to the lamellae taken from position 2 in Fig. 9.1* is shown again in Fig. 9.3a* [65]. Figure 9.3b-e* shows the cross sectional TEM image of the irradiated sample [65]. Differing from the near surface nitride layer, few voids were observed. All the voids were located within 1 µm distance from the irradiated surface, in agreement with the SRIM calculation of Fe projected range (about 1 µm). For the bulk region, as marked in Fig. 9.4a*, high-density voids were observed, as shown in the cross sectional TEM images of Fig. 9.4b-e* [65]. The void sizes ranged from 20 nm to 90 nm. The high swelling agreed with the literature reported for untreated 316L.

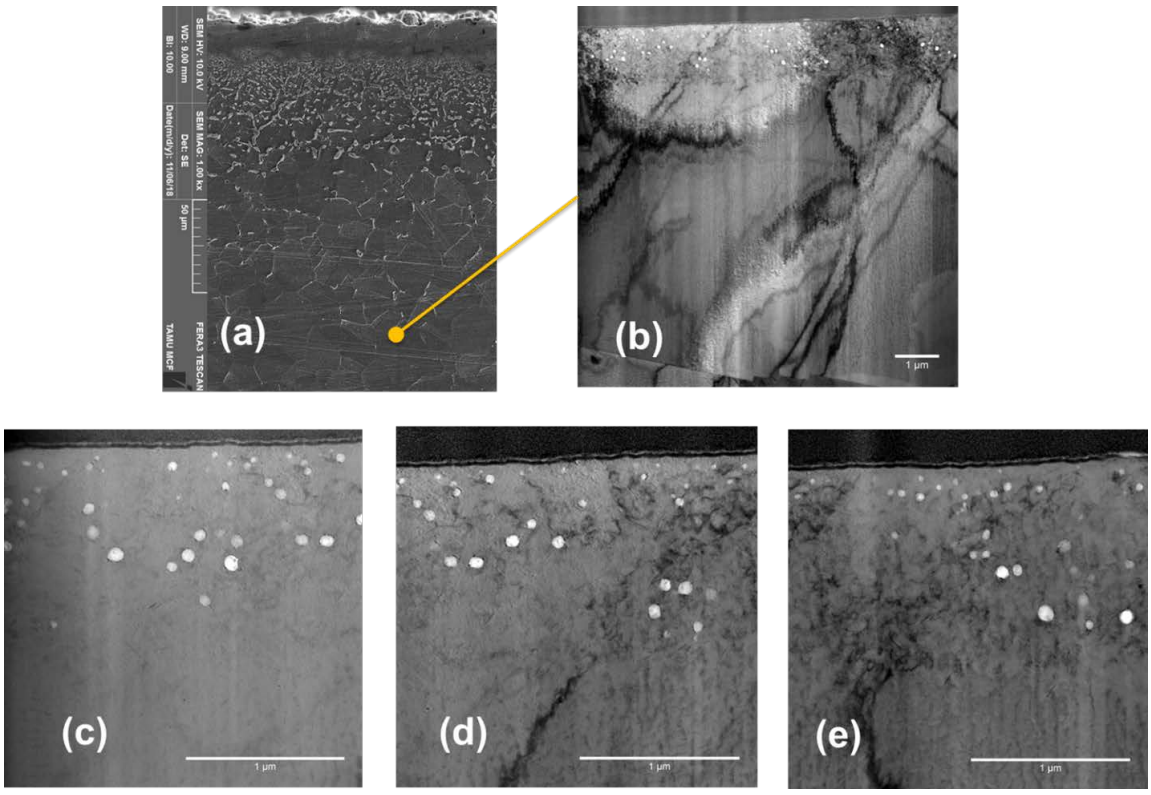

Figure 9.4: Images of TEM analysis of irradiated unnitride layer. (a) SEM image of the cross sectional of nitrided 316L and position of the FIB lift out for TEM characterization, (b-e) cross sectional TEM images of the irradiated sample. Reprinted with permission from [65]*.

The different swelling behaviors of the nitride layer, nitrogen-enriched layer, and bulk 316L can be attributed to difference in lattice structures, grain morphology and nitrogen impurity effects. As shown in Fig. 9.1*, the surface nitride appears as a dense layer [65]. At distances beyond 30 µm, the nitrogen rich layer appeared with small grains. The grain sizes gradually increased as a function of distance, from a mean size of a few microns at the depth of 30 µm to a mean size of about 20 µm at the depth beyond 70 µm. Since grain boundaries act as defect sinks, a high boundary-to-volume ratio in the near surface region helps to remove point defects

from the irradiation.

Another effect may come from nitrogen as impurities. There are no systematic studies on nitrogen effects on swelling. Different from helium atoms, which are fast diffusers that can easily interact with vacancies and stabilize void nucleation, the larger nitrogen atoms are not expected to diffuse as quickly. Hence their interactions with open volume defects are limited. It is likely that nitrogen atoms act as interstitial impurities to directly interact with vacancy defect and reduce their effective diffusivities, hence slowing down the defect clustering process towards large voids. Nitrogen impurities can also act as blockers for dislocation growth. Dislocation growth is one important mechanism for their biased trapping of Fe interstitials. If dislocations become immobilized without growth, Fe interstitials will have a higher probability of interacting with vacancies for enhanced defect recombination.

9.2 Conclusion

The study shows that the surface nitridation can enhance swelling resistance of 316L. After 50 dpa irradiation at 600 °C, the surface nitride layer does not form voids. For the nitrogen-rich layer which is beneath the surface nitride layer, very limited voids are observed. In a comparison, significant swelling is observed in the bulk region at deep depths.

10. URANIUM-ZIRCALOY-4 DIFFUSION COUPLE

The interface interactions between U and Zircaloy-4 was studied. For a comparison study, both nitrided and unnitrided Zircaloy-4 were bonded with U in order to study whether nitridation could inhibit U diffusion. This study is important since nuclear fuel can swell and mechanically interact fuel cladding, hence inducing interface interactions. The nitriding processing can be designed to treat the inner surface of Zircaloy-4 cladding tubes. With the presence of nitrided layers or nitrogen-rich layers, U diffusion may be retarded and interface reactions reduced. If so, the fuel-cladding system can have enhanced accident tolerance. In general, interface compounds are brittle in their natures and represent regions of weak mechanical properties.

For a diffusion couple formed by mechanically bonding two polished metals, thermal annealing with a sufficient thermal budget drives atomic diffusion cross the original interface to form interface compounds [123, 124]. For a bonded binary system at early stage of diffusion, the atomic penetration is governed by Fick's law. When the thermal budget is high enough, the concentration profile evolves into a step height distributions, with each step corresponding to an equilibrium phase predicted by the phase diagram. A diffusion couple can be formed at a pre-selected temperature and is quickly quenched to ambient temperature. Thus, the microstructures corresponding to a higher temperature in the phase diagram is preserved at a low temperature for characterization. In this way, temperature dependencies of phase diagrams can be systematically studied.

10.1 Procedure Details

Figure 10.1* shows the U-Zr phase diagram [66]. In order to avoid the complexity of forming γ, γ_1 and γ_2 phases, the diffusion couple annealing temperature of 600 °C was selected. At this temperature, the interface region was expected to form α, δ, and ϵ phases. According to Gibbs phase rule, the degrees of freedom $F = C - P + 2$ [135], where C is the number of components and P is the number of phases. In a U-Zr binary system and in the composition range corresponding to the phase diagram having co-existence of two phases, $C = 2$ and $P = 2$, thus $F = 2$. This means that under given pressure and temperature, there was no additional freedom for composition changes, thus leading to step height distributions. Based on Fig. 10.1, it was expected to observe a one-step height elemental distribution in the interface region which corresponded to the δ phase.

*[66] Used with permission of Springer Nature BV, from U-zr (uranium-zirconium), H, Okamoto, 13, 1991; permission conveyed through Copyright Clearance Center, Inc.

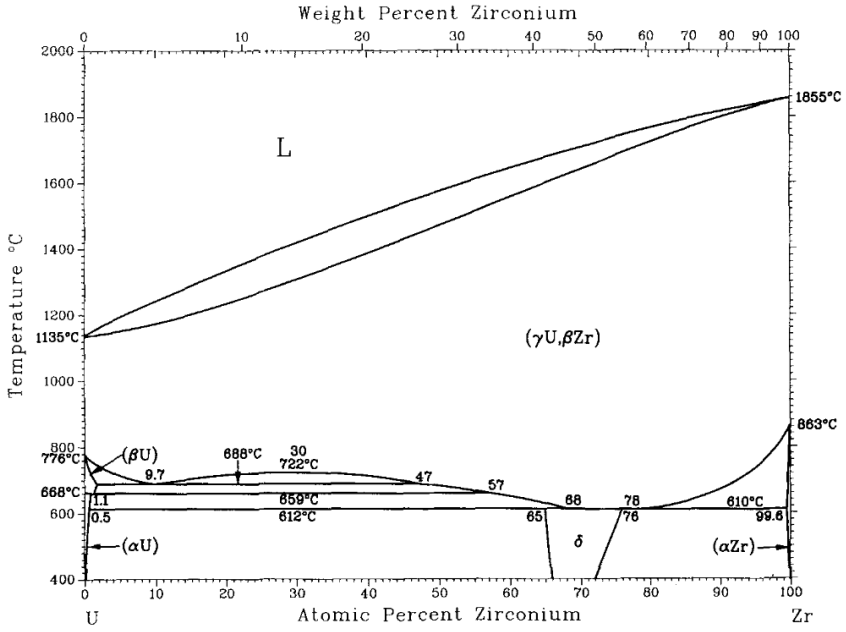

Figure 10.1: U-Zr phase diagram. Used with permission of Springer Nature BV, from U-zr (uranium-zirconium), H, Okamoto, 13, 1991; permission conveyed through Copyright Clearance Center, Inc. [66]*.

10.1.1 Nitridation

Nitridation was performed at 908 °C for 10 hours. The biased voltage between the grounding plate (from the top of the cage) and cage was 590 volts. The cage was 1.25 inches tall with a diameter of 2.5 inches. The holes on the cage were 0.25 inches in diameter. The space between neighboring holes was 1/16 of an inch. The sample inside the cage was connected to the sample stage. The sample stage and the cage were at the same potential. The gas used was a mixture of 90 at.% nitrogen and 10 at.% hydrogen. The pressure during nitridation was maintained at 1.5 torr. After the plasma was ignited, both the pressure and voltage were slowly increased to operational settings. The temperature of the system was monitored radiatively via

an electrically-insulated thermocouple inside the sample holder.

Figure 10.2 shows a SEM image of the cross section of the nitrided Zircaloy-4 using a low electron beam energy (5 keV) to improve the contrast. The cross section was polished using 0.1 µm diamond lapping paper. The relatively smooth layer of about 40 µm thickness is the nitridation-affected layer. The hardness of this layer was higher than the bulk. At depths deeper than 40 µm, surface scratching are more prevalent due to lower relative hardness.

Figure 10.2: The image of a diffusion couple after being cut by half.

10.1.2 Diffusion Couple

The diffusion couple, made by mechanically bonding U and Zircaloy-4 samples, was sealed inside a quartz tube using a plasma torch. Bonding was performed inside a glove box circulated with Ar gas to avoid oxidation. For U, the surface was cleaned with nitric acid. The Zircaloy-4 surface was cleaned with acetone. Each diffusion couple contained three layers: nitrided Zircaloy-4, U and un-nitrided Zircaloy-4 arranged in a sandwich-like configuration. This created two interfaces, one was U/nitrided Zircaloy-4 and the other was U/un-nitrided Zircaloy. A comparison thus could be made after the same annealing of the two diffusion interfaces. Screws were used to apply force against two Zricaloy-4 sides to maintain the integrity during the annealing.

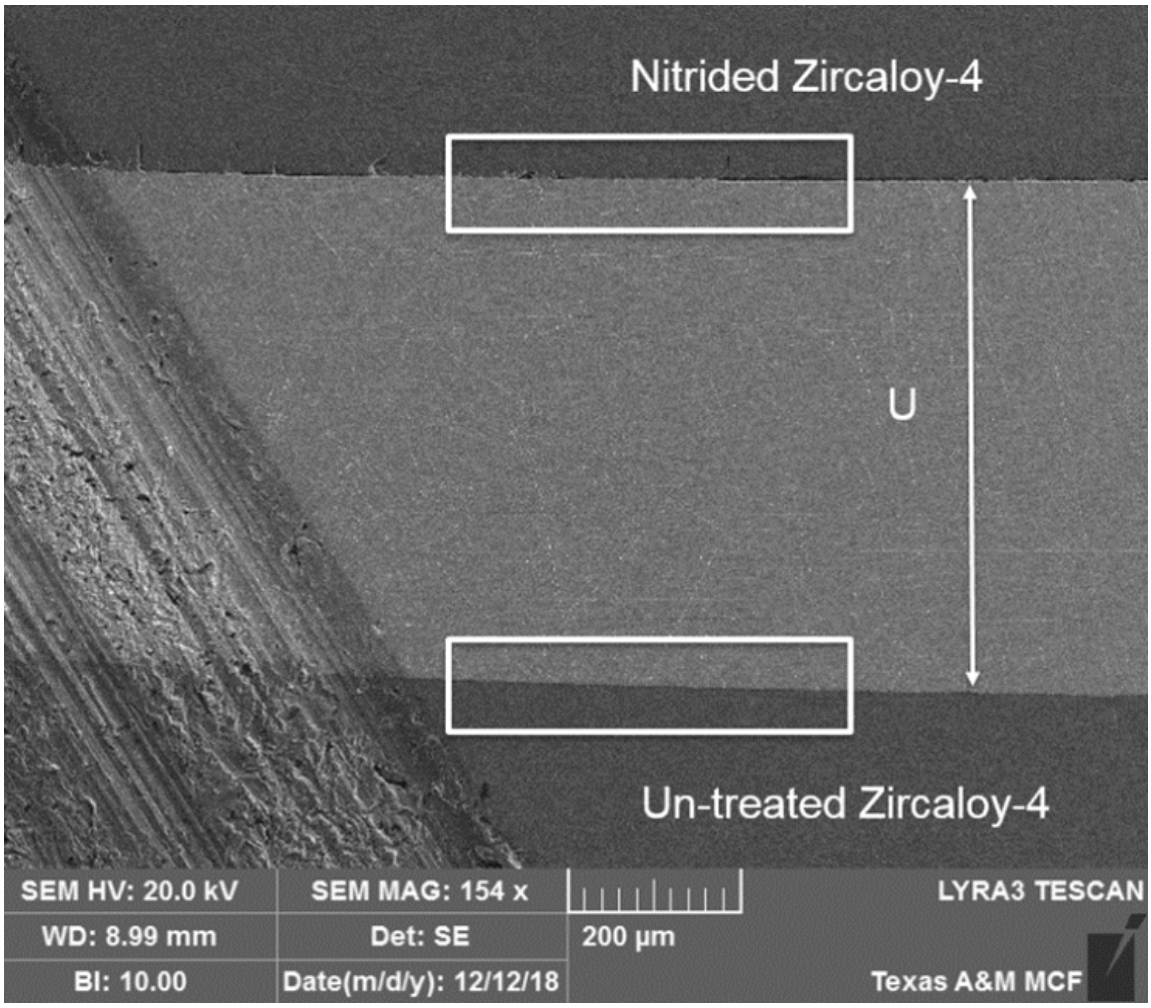

Figure 10.3: SEM image of the cross section of sandwich-like nitrided/U/untreated U diffusion couple after polishing.

Prior to sealing, the tube was pumped to a high vacuum of about 1E-6 Torr. After being sealed, the tubes were annealed in a furnace at 600 °C for 2 weeks. Once annealing was completed, the tubes were quenched in ice water. The diffusion couple was then encased in epoxy and the sample cut in half to create a new cross section, following by mechanical polishing using 0.1 µm diamond lapping paper. Figure 10.2 shows the photo image of the diffusion couple after being cut in half. Figure 10.3

shows the cross sectional SEM image of the newly polished surface. U was bonded between nitrided Zircaloy-4 and un-nitrided Zircaloy-4, with a clear visible contrast.

10.1.3 Characterization

A JEOL JSM-7500F scanning electron microscope (SEM) was used to characterize surface tomography and EDS composition analysis was performed using a 30 keV electron beam. A line-scan analysis was executed to profile the compositional change of the materials versus distance across the diffusion interface boundary. A total of 11 spots are characterized with points spacings of 250 nm. Each sample interface scan was repeated 3 times to produce error bars.

10.2 Results and Discussion

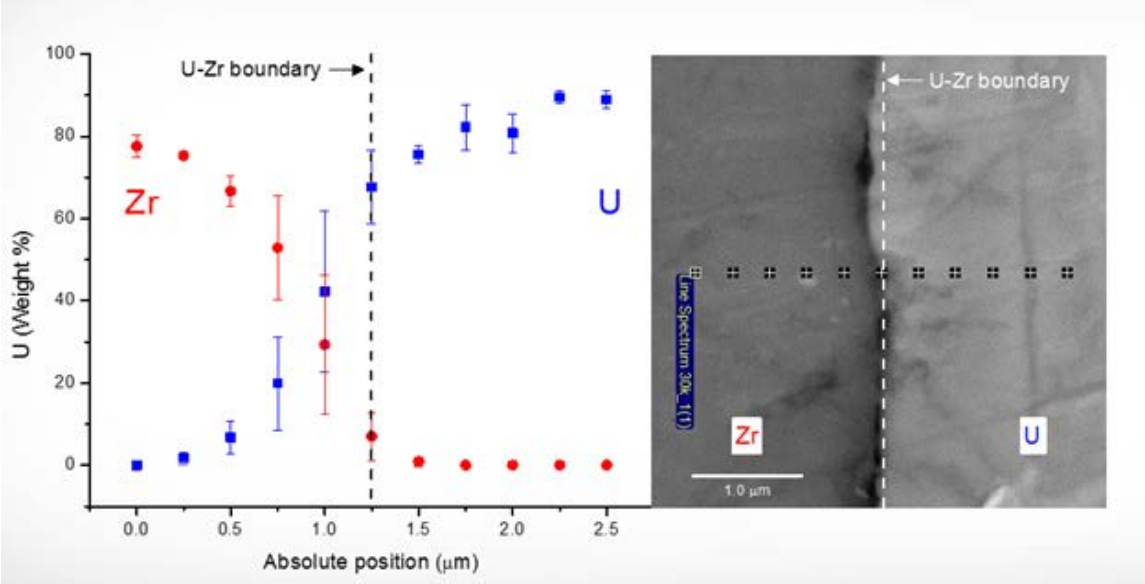

Figure 10.4: EDS mapping of U and Zr elementary distributions across the interface of U/un-treated Zr after annealing at 600 °C for two weeks and the corresponding SEM image showing the EDS characterization spot positions. The dash lines refer to the original interface visible from SEM imaging.

Figure 10.4 plots EDS mapping of Zr and U composition changes across the interface for the diffusion couple of U and un-treated Zircaloy-4. The right side is the corresponding SEM image. The vertical dash line refers to the original interface which is clearly visible under SEM. There is no obvious step height-like elemental distribution. There are two possibilities to explain this occurrence. One is that interface compound may have formed within a narrow region with thickness beyond the spatial resolution of EDS mapping. Another reason could be that the thermal budget was not high enough to reach equilibrium phases predicted by U-Zr phase diagram.

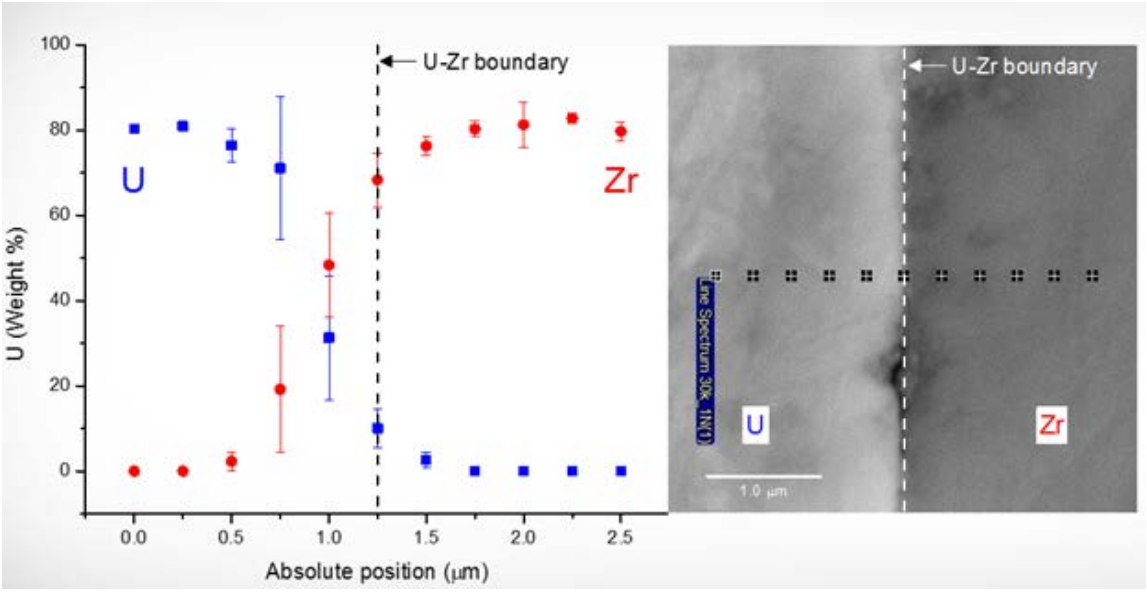

Figure 10.5: EDS mapping of U and Zr elementary distributions across the interface of U/nitrided Zr after annealing at 600 °C for two weeks and the corresponding SEM image showing the EDS characterization spot positions. The dash lines refer to the original interface visible from SEM imaging.

In comparison, Fig. 10.5 plots Zr and U composition changes of annealed U/nitrided

Zircaloy-4 sample. The dash line refers to the original interface. Judging by the U diffusion tail beyond the interface, we conclude that U diffusion is retarded by the nitrided surface of Zircaloy-4. On the other hand, Zr diffusion into U side appears enhanced.

10.3 Conclusion

The difference in U penetration into Zircaloy-4 (untreated vs. nitrided) suggests that nitridation is able to retard diffusion, hence minimizing interface reactions. Although the nitridation is mainly used to improve corrosion and hardness changes of the side of fuel cladding facing coolant, the present study that, optionally, nitridation can be applied to the inner side of the tube to reduce fuel-cladding interaction.

REFERENCES

[1] AAS Steinar. Mechanical interaction between fuel and cladding. *Nuclear Engineering and Design*, 21(2):237–253, January 1972.

[2] David Pye. *Practical Nitriding and Ferritic Nitrocarburizing. David Pye.* Materials Park, Ohio : ASM International, [2003], 2003.

[3] R. R. M. de Sousa, F. O. de Araújo, L. C. Gontijo, J. A. P. da Costa, and C. Alves. Cathodic cage plasma nitriding (CCPN) of austenitic stainless steel (AISI 316): Influence of the different ratios of the (N2/H2) on the nitrided layers properties. *Vacuum*, 86(12):2048–2053, 2012.

[4] Anthony C. Fischer-Cripps. *Nanoindentation. 3rd Ed. Anthony C. Fischer-Cripps.* Mechanical Engineering Series: 1. New York : Springer, [2011], 2011.

[5] Edward L. Tobolski and Andrew Fee. Macroindentation Hardness Testing. January 2000.

[6] G01 Committee. Reference Test Method for Making Potentiodynamic Anodic Polarization Measurements. Technical report, ASTM International.

[7] R. G. Kelly, editor. *Electrochemical Techniques in Corrosion Science and Engineering.* Number 18 in Corrosion Technology. Marcel Dekker, New York, 2003.

[8] G01 Committee. Practice for Conventions Applicable to Electrochemical Measurements in Corrosion Testing. Technical report, ASTM International.

[9] Florian Mansfeld. Electrochemical Methods of Corrosion Testing. January 2003.

[10] Stainless steel | Definition, Composition, Types, & Facts. https://www.britannica.com/technology/stainless-steel.

[11] A. Fossati, F. Borgioli, E. Galvanetto, and T. Bacci. Corrosion resistance properties of glow-discharge nitrided {AISI} 316L austenitic stainless steel in NaCl solutions. *Corrosion Science*, 48(6):1513–1527, 2006.

[12] Thomas Christiansen and Marcel A. J. Somers. Decomposition kinetics of expanded austenite with high nitrogen contents. *Zeitschrift für Metallkunde*, 97(1):79–88, 2006.

[13] R. L. Klueh. Elevated temperature ferritic and martensitic steels and their application to future nuclear reactors. *International Materials Reviews*, 50(5):287–310, October 2005.

[14] L Gribaudo, D Arias, and J Abriata. ASM Alloy Phase Diagrams Database. Nitrogen-Zirconium Binary Phase Diagram, P. Villars, Editor-in-Chief; H. Okamoto and K. Cenzual, Section Editors; Www.Asminternational.Org. ASM International, Materials Park, OH, 2016.

[15] S.J. Lee, H.S. Kwon, W. Kim, and B.H. Choi. Effects of compositional and structural change on the corrosion behaviour of nitrogen implanted Zircaloy-4. *Materials Science and Engineering: A*, 263(1):23–31, 1999.

[16] David Mercier. Models for thin films. *Models for thin films - NIMS toolbox 3.2.0 documentation*, 2014.

[17] C. Alves, F. O. de Araújo, K. J. B. Ribeiro, J. A. P. da Costa, R. R. M. Sousa, and R. S. de Sousa. Use of cathodic cage in plasma nitriding. *Surface and Coatings Technology*, 201(6):2450–2454, 2006.

[18] Akio Nishimoto, Atsushi Tokuda, and Katsuya Akamatsu. Effect of Through Cage on Active Screen Plasma Nitriding Properties. *MATERIALS TRANSACTIONS*, 50(5):1169–1173, 2009.

[19] X.Y. Li. Joint Second Prize Low Temperature Plasma Nitriding of 316 Stainless Steel – Nature of S Phase and Its Thermal Stability. *Surface Engineering*, 17(2):147–152, April 2001.

[20] C. X Li and T Bell. Sliding wear properties of active screen plasma nitrided 316 austenitic stainless steel. *Wear*, 256(11):1144–1152, June 2004.

[21] R. R. M. de Sousa, F. O. de Araújo, K. J. B. Ribeiro, J. A. P. da Costa, R. S. de Sousa, and C. Alves. Uniformity of temperature in cathodic cage technique in nitriding of austenitic stainless steel AISI 316. *Surface Engineering*, 24(4):313–318, July 2008.

[22] C. Zhao, L. Y. Wang, and L. Han. Active screen plasma nitriding of AISI 316L austenitic stainless steel at different potentials. *Surface Engineering*, 24(3):188–192, May 2008.

[23] G. Y. Li and M. K. Lei. Microstructure and Properties of Plasma Source Nitrided AISI 316 Austenitic Stainless Steel. *Journal of Materials Engineering and Performance*, 26(1):418–423, January 2017.

[24] Xingwei Wang, Zhongyu Liu, Yangyang Chen, Jinquan Sun, Qingkun He, Qiancheng Liu, Guozhi Liu, and Kun Xie. Abrasive resistance and corrosion properties of AISI 316 sieve via low-temperature gaseous nitriding. *Surface and Coatings Technology*, 361:349–356, March 2019.

[25] A. Triwiyanto, P. Hussain, A. Rahman, and M.C. Ismail. The Influence of Nitriding Time of AISI 316L Stainless Steel on Microstructure and Tribological

Properties. *Asian Journal of Scientific Research*, 6(2):323–330, March 2013.

[26] Nitriding of Stainless Steels. In Jon L. Dossett and George E. Totten, editors, *Heat Treating of Irons and Steels*, pages 418–438. ASM International, 2014.

[27] Thomas L. Christiansen and Marcel A. J. Somers. Low-temperature gaseous surface hardening of stainless steel: The current status. *International Journal of Materials Research*, 100(10):1361–1377, October 2009.

[28] Waldemar Alfredo Monteiro, Silvio Andre Lima Pereira, and Jan Vatavuk. Nitriding Process Characterization of Cold Worked AISI 304 and 316 Austenitic Stainless Steels. *Journal of Metallurgy*, 2017:e1052706, January 2017.

[29] Thomas L. Christiansen and Marcel A. J. Somers. Determination of the concentration dependent diffusion coefficient of nitrogen in expanded austenite. *International Journal of Materials Research*, 99(9):999–1005, September 2008.

[30] C. X. Li, J. Georges, and X. Y. Li. Active screen plasma nitriding of austenitic stainless steel. *Surface Engineering*, 18(6):453–457, December 2002.

[31] R. R. M. de Sousa, F. O. de Araújo, J. A. P. da Costa, T. Dumelow, R. S. de Oliveira, and C. Alves. Nitriding in cathodic cage of stainless steel AISI 316: Influence of sample position. *Vacuum*, 83(11):1402–1405, July 2009.

[32] M. Keddam, T. Thiriet, G. Marcos, and T. Czerwiec. Characterization of the expanded austenite developed on AISI 316 LM steel by plasma nitriding. *Journal of Mining and Metallurgy, Section B: Metallurgy*, 53(1):47–52, 2017.

[33] X. Y. Li and H. Dong. Effect of annealing on corrosion behaviour of nitrogen S phase in austenitic stainless steel. *Materials Science and Technology*, 19(10):1427–1434, October 2003.

[34] Y. Sun, X. Y. Li, and T. Bell. X-ray diffraction characterisation of low temperature plasma nitrided austenitic stainless steels. *Journal of Materials Science*, 34(19):4793–4802, October 1999.

[35] Francesca Borgioli, Emanuele Galvanetto, and Tiberio Bacci. Low temperature nitriding of AISI 300 and 200 series austenitic stainless steels. *Vacuum*, 127:51–60, May 2016.

[36] Thierry Czerwiec, Huan He, Grégory Marcos, Tony Thiriet, Sylvain Weber, and Henri Michel. Fundamental and Innovations in Plasma Assisted Diffusion of Nitrogen and Carbon in Austenitic Stainless Steels and Related Alloys. *Plasma Processes and Polymers*, 6(6-7):401–409, 2009.

[37] Linda Gil, Sonia Brühl, Lorena Jiménez, Ovidio León, Rafael Guevara, and Mariana Staia. Corrosion performance of the plasma nitrided 316L stainless steel. *Surface and Coatings Technology*, 201:4424–4429, December 2006.

[38] Mohd Khairul Munir Mohd Khairul Munir B Kamaruzaman. *Improvement on Wear Resistance of 316 Austenitic Stainless Steel by High Temperature Nitriding Technique*. PhD thesis, Universiti Teknologi Petronas, 2010.

[39] Teresa Moskalioviene and Arvaidas Galdikas. Stress induced and concentration dependent diffusion of nitrogen in plasma nitrided austenitic stainless steel. *Vacuum*, 86(10):1552–1557, April 2012.

[40] C. Templier, J. C. Stinville, P. Villechaise, P. O. Renault, G. Abrasonis, J. P. Rivière, A. Martinavičius, and M. Drouet. On lattice plane rotation and crystallographic structure of the expanded austenite in plasma nitrided AISI 316L steel. *Surface and Coatings Technology*, 204(16):2551–2558, May 2010.

[41] Nitin Kumar, G. P. Chaudhari, and Sai Ramudu Meka. Investigation of Low-Temperature Liquid Nitriding Conditions for 316 Stainless Steel for Improved Mechanical and Corrosion Response. *Transactions of the Indian Institute of Metals*, 73(1):235–242, January 2020.

[42] Elhadj Ghelloudj. Microstructure, Mechanical and Tribological Behaviour of Aisi 316l Stainless Steel During Salt Bath Nitriding. *Acta Metallurgica Slovaca*, 27(2):47–52, April 2021.

[43] Guandong Luo, Zhi Zheng, Likui Ning, Zheng Tan, Jian Tong, and Enze Liu. Failure analysis of AISI 316L ball valves by salt bath nitriding. *Engineering Failure Analysis*, 111:104455, April 2020.

[44] L Rajeev Reddy and Ram Subbiah. Salt bath nitriding on 316l austenitic stainless steels. *International Journal of Aerospace and Mechanical Engineering.*, 5:2393–8609, 2016.

[45] Takashi Watanabe, Masatoshi Kondo, and Akio Sagara. Nitriding of 316 stainless steel in molten fluoride salt by an electrochemical technique. *Electrochimica Acta*, 58:681–690, December 2011.

[46] P Corengia, G Ybarra, C Moina, A Cabo, and E Broitman. Microstructure and corrosion behaviour of DC-pulsed plasma nitrided AISI 410 martensitic stainless steel. *Surface and Coatings Technology*, 187(1):63–69, October 2004.

[47] C. X. Li and T. Bell. A comparative study of low temperature plasma nitriding, carburising and nitrocarburising of AISI 410 martensitic stainless steel. *Materials Science and Technology*, 23(3):355–361, March 2007.

[48] C. X. Li and T. Bell. Corrosion properties of plasma nitrided AISI 410 martensitic stainless steel in 3.5% NaCl and 1% HCl aqueous solutions. *Corrosion*

Science, 48(8):2036–2049, August 2006.

[49] C. K. Lee and H. C. Shih. The abrasive corrosion behavior of plasma-nitrided alloy steels in chloride environments. *Journal of Materials Science*, 35(9):2361–2369, May 2000.

[50] K. Marchev, C. V. Cooper, and B. C. Giessen. Observation of a compound layer with very low friction coefficient in ion-nitrided martensitic 410 stainless steel. *Surface and Coatings Technology*, 99(3):229–233, February 1998.

[51] Hongyu Shen and Liang Wang. Mechanism and properties of plasma nitriding AISI 420 stainless steel at low temperature and anodic (ground) potential. *Surface and Coatings Technology*, 403:126390, December 2020.

[52] L. A. Espitia, Hanshan Dong, Xiao-Ying Li, C. E. Pinedo, and A. P. Tschiptschin. Scratch test of active screen low temperature plasma nitrided AISI 410 martensitic stainless steel. *Wear*, 376–377:30–36, April 2017.

[53] R. R. M. de Sousa, F. O. de Araújo, K. J. B. Ribeiro, T. Dumelow, J. A. P. da Costa, and C. Alves. Ionic nitriding in cathodic cage of AISI 420 martensitic stainless steel. *Surface Engineering*, 24(1):52–56, January 2008.

[54] L. A. Espitia, L. Varela, C. E. Pinedo, and A. P. Tschiptschin. Cavitation erosion resistance of low temperature plasma nitrided martensitic stainless steel. *Wear*, 301(1):449–456, April 2013.

[55] E. Stagno, M. R. Pinasco, G. Palombarini, M. G. Ienco, and G. F. Bocchini. Behaviour of sintered 410 low carbon steels towards ion nitriding. *Journal of Alloys and Compounds*, 247(1):172–179, January 1997.

[56] T. Bacci, F. Borgioli, E. Galvanetto, and G. Pradelli. Glow-discharge nitriding of sintered stainless steels. *Surface and Coatings Technology*, 139(2):251–256,

May 2001.

[57] P. Corengia, F. Walther, G. Ybarra, S. Sommadossi, R. Corbari, and E. Broitman. Friction and rolling–sliding wear of DC-pulsed plasma nitrided AISI 410 martensitic stainless steel. *Wear*, 260(4):479–485, February 2006.

[58] Carlos E. Pinedo and Waldemar A. Monteiro. On the kinetics of plasma nitriding a martensitic stainless steel type AISI 420. *Surface and Coatings Technology*, 179(2):119–123, February 2004.

[59] S. K Kim, J. S Yoo, J. M Priest, and M. P Fewell. Characteristics of martensitic stainless steel nitrided in a low-pressure RF plasma. *Surface and Coatings Technology*, 163–164:380–385, January 2003.

[60] J. G. Desmaison and W. W. Smeltzer. Nitrogen Diffusion in Zirconium Nitride. *Journal of The Electrochemical Society*, 122(3):354–357, March 1975.

[61] C. J. Rosa and W. C. Hagel. A Film-Thickness Determination of Nitrogen Diffusion in Zirconium Nitride. *Journal of the Electrochemical Society*, 115(5):467, May 1968.

[62] A. Anttila, J. Räisänen, and J. Keinonen. Diffusion of nitrogen in α-Zr AND α-Hf. *Journal of the Less Common Metals*, 96:257–262, January 1984.

[63] B. Predel. Fe-N (Iron-Nitrogen). In O. Madelung, editor, *Dy-Er – Fr-Mo*, volume e, pages 1–5. Springer-Verlag, Berlin/Heidelberg, 1995.

[64] Robert Balerio, Hyosim Kim, Andres Morell-Pacheco, Laura Hawkins, Ching-Heng Shiau, and Lin Shao. ZrN Phase Formation, Hardening and Nitrogen Diffusion Kinetics in Plasma Nitrided Zircaloy-4. *Materials*, 14(13):3572, June 2021.

[65] Andres Morell-Pacheco, Hyosim Kim, Tianyao Wang, Ching-Heng Shiau, Robert Balerio, Adam Gabriel, and Lin Shao. Ni coating on 316L stainless steel using cage plasma treatment: Feasibility and swelling studies. *Journal of Nuclear Materials*, 540:152385, November 2020.

[66] H. Okamoto. U-zr (uranium-zirconium). *Journal of Phase Equilibria*, 13(1):109–110, February 1992.

[67] Kurt Edsinger. EPRI and the zero fuel failures program. *Nuclear News*, 53(13):40–45, December 2010.

[68] S. J. Zinkle and G. S. Was. Materials challenges in nuclear energy. *Acta Materialia*, 61(3):735–758, February 2013.

[69] J. Bakosi, M. A. Christon, R. B. Lowrie, L. A. Pritchett-Sheats, and R. R. Nourgaliev. Large-eddy simulations of turbulent flow for grid-to-rod fretting in nuclear reactors. *Nuclear Engineering and Design*, 262:544–561, September 2013.

[70] OECD Nuclear Energy Agency. *Very High Burn-Ups in Light Water Reactors*. Nuclear Science. Nuclear Energy Agency, Organisation for Economic Co-operation and Development, Issy-les-Moulineaux, France, 2006.

[71] Dmitry V. Paramonov. Pellet-Cladding Interaction Probability Assessment Model. *Journal of Pressure Vessel Technology*, 134(1), February 2012.

[72] Barry Gordon. Corrosion and Corrosion Control in LWRs. page 50, 2011.

[73] Understanding and Mitigating Ageing in Nuclear Power Plants | ScienceDirect. https://www.sciencedirect.com/book/9781845695118/understanding-and-mitigating-ageing-in-nuclear-power-plants.

[74] Gary S. Was. *Fundamentals of Radiation Materials Science : Metals and Alloys. Gary S. Was.* Springer, 2007.

[75] NRC: 10 CFR 50.46 Acceptance criteria for emergency core cooling systems for light-water nuclear power reactors. https://www.nrc.gov/reading-rm/doc-collections/cfr/part050/part050-0046.html.

[76] P. Hubbard, S. J. Dowey, E. D. Doyle, and D. G. McCulloch. Influence of bias and in situ cleaning on through cage (TC) or active screen plasma nitrided (ASPN) steels. *Surface Engineering*, 22(4):243–247, 2006.

[77] Jean Georges. Nitriding process and nitriding furnace therefor, November 1999.

[78] Gopal Revankar. Introduction to Hardness Testing. In *Mechanical Testing and Evaluation.* ASM International, January 2000.

[79] W.D. Callister. *Materials Science And Engineering: An Introduction.* John Wiley & Sons, 2007.

[80] Encyclopedia Britannica. Mohs hardness. 2015.

[81] George F. Vander Voort. Microindentation Hardness Testing. In *Mechanical Testing and Evaluation.* ASM International, January 2000.

[82] G01 Committee. Practice for Calculation of Corrosion Rates and Related Information from Electrochemical Measurements. Technical report, ASTM International.

[83] Carl Wagner and Wilhelm Traud. Concerning the Evaluation of Corrosion Reactions by Superposition of Electrochemical Partial Reactions and Concerning the Potential Formation on Mixed Electrodes. *Elektrochemie und angewandte physikalische Chemie*, 44(7):391–402, 1938.

[84] M. Stern and A. L. Geary. Electrochemical Polarization: I . A Theoretical Analysis of the Shape of Polarization Curves. *Journal of The Electrochemical Society*, 104(1):56, January 1957.

[85] Florian Mansfeld. The Polarization Resistance Technique for Measuring Corrosion Currents. In Mars G. Fontana and Roger W. Staehle, editors, *Advances in Corrosion Science and Technology*, pages 163–262. Springer US, Boston, MA, 1976.

[86] Florian Mansfeld. Tafel slopes and corrosion rates obtained in the pre-Tafel region of polarization curves. *Corrosion Science*, 47(12):3178–3186, December 2005.

[87] Gerald S. Frankel. Techniques for Corrosion Quantification. In *Characterization of Materials*, pages 1–14. American Cancer Society, 2012.

[88] George Krauss. 1.3 steels - definitions, 2015.

[89] Carelyn E. Campbell, Mark R. Stoudt, and Fan Zhang. Additive Manufacturing of Steels and Stainless Steels. In David L. Bourell, William Frazier, Howard Kuhn, and Mohsen Seifi, editors, *Additive Manufacturing Processes*, volume 24, page 0. ASM International, June 2020.

[90] What is Ferritic Stainless Steel? https://www.azom.com/article.aspx?ArticleID=19195, April 2020.

[91] Benoist Muzeau, Stéphane Perrin, Catherine Corbel, Dominique Simon, and Damien Feron. Electrochemical behaviour of stainless steel in {PWR} primary coolant conditions: Effects of radiolysis. *Journal of Nuclear Materials*, 419(1–3):241–247, 2011.

[92] Daniel de Souza Gomes, Alfredo Abe, e Silva Antonio Teixeira, Claudia Giovedi, and Ramos Martins Marcelo. Evaluation of corrosion on the fuel performance of stainless steel cladding. *EPJ Nuclear Sciences & Technologies, Vol 2, p 40 (2016)*, page 40, 2016.

[93] R. W. Cahn, P. Haasen, and E. J. Kramer. *Materials Science and Technology : A Comprehensive Treatment. Classic Softcover Ed. Edited by R.W. Cahn, P. Haasen, E.J. Kramer.* Weinheim : Wiley-VCH, [2005-], 2005.

[94] OK Chopra. *Degradation of LWR Core Internal Materials Due to Neutron Irradiation.* US Nuclear Regulatory Commission, Office of Nuclear Regulatory Research, 2010.

[95] CRF Azevedo. Selection of fuel cladding material for nuclear fission reactors. *Engineering Failure Analysis*, 18(8):1943–1962, 2011.

[96] Luiz Carlos Casteletti, Amadeu Lombardi Neto, and George E. Totten. Nitriding of Stainless Steels. In *Heat Treating of Irons and Steels.* ASM International, October 2014.

[97] Z. L. Zhang and T. Bell. Structure and Corrosion Resistance of Plasma Nitrided Stainless Steel. *Surface Engineering*, 1(2):131–136, January 1985.

[98] K Ichii. Structure of the ion-nitrided layer of 18-8 stainless steel. *Technol. Rep. Kansai Univ.*, 27:135, 1986.

[99] A. Leyland, D.B. Lewis, P.R. Stevensom, and A. Matthews. Low temperature plasma diffusion treatment of stainless steels for improved wear resistance. *Surface and Coatings Technology*, 62(1-3):608–617, December 1993.

[100] F Taherkhani and A Taherkhani. Surface characterization of through cage plasma nitriding on the surface properties of low alloy steel. *Scientia Iranica.*

Transaction B, Mechanical Engineering, 17(4):253, 2010.

[101] J.C. Stinville, C. Tromas, P. Villechaise, and C. Templier. Anisotropy changes in hardness and indentation modulus induced by plasma nitriding of 316L polycrystalline stainless steel. *Scripta Materialia*, 64(1):37–40, 2011.

[102] F. Yildiz and A. Alsaran. Multi-pass scratch test behavior of modified layer formed during plasma nitriding. *Tribology International*, 43(8):1472–1478, 2010.

[103] Y. Li, L. Wang, J. Xu, and D. Zhang. Plasma nitriding of AISI 316L austenitic stainless steels at anodic potential. *Surface and Coatings Technology*, 206(8):2430–2437, January 2012.

[104] H. Dong. S-phase surface engineering of Fe-Cr, Co-Cr and Ni-Cr alloys. *International Materials Reviews*, 55(2):65–98, March 2010.

[105] T. Czerwiec, A. Andrieux, G. Marcos, H. Michel, and Ph Bauer. Is "expanded austenite" really a solid solution? Mössbauer observation of an annealed AISI 316L nitrided sample. *Journal of Alloys and Compounds*, 811:151972, November 2019.

[106] Yang Li, Zhuo Wang, and Liang Wang. Surface properties of nitrided layer on AISI 316L austenitic stainless steel produced by high temperature plasma nitriding in short time. *Applied Surface Science*, 298:243–250, April 2014.

[107] André Paulo Tschiptschin, Arthur Seiji Nishikawa, Luis Bernardo Varela, and Carlos Eduardo Pinedo. Thermal stability of expanded austenite formed on a DC plasma nitrided 316L austenitic stainless steel. *Thin Solid Films*, 644:156–165, December 2017.

[108] Joseph Buhagiar. 25 years of S-phase. *Surface Engineering*, 26(4):229–232, May 2010.

[109] Florian Schebitz and Abdelhalim Mekmouche. *Design Basis of Core Components and Their Realization in the Frame of the EPR'ssup TM Core Component Development*. July 2008.

[110] R.L. Klueh, K. Ehrlich, and F. Abe. Ferritic/Martensitic steels: Promises and problems. *Journal of Nuclear Materials*, 191:116–124, 1992.

[111] M. Seitz, J. Hoffmann, M. Rieth, P. Margraf, R. Senn, M. Klimenkov, R. Lindau, S. Baumgärtner, U. Jäntsch, P. Franke, and A. Möslang. Assessment of industrial nitriding processes for fusion steel applications. *Nuclear Materials and Energy*, 13:90–98, December 2017.

[112] Masatoshi Kondo, Takashi Watanabe, Teruya Tanaka, Dongxun Zhang, and Akio Sagara. Nitriding Treatment of Reduced Activation Ferritic Steel as Functional Layer for Liquid Breeder Blanket. *Plasma and Fusion Research*, 6:2405117–2405117, 2011.

[113] Tatsuyuki Nezu, Koji Sekine, Yasuo Otoguro, Masao Inoue, and Kazuteru Ohishi. Nitriding characteristic and its effects on high temperature properties in a modified 9Cr-1Mo steel. *Journal of High Pressure Institute of Japan*, 40(6):333–339, 2002.

[114] L Gribaudo, D Arias, and J Abriata. The n-zr (nitrogen-zirconium) system. *Journal of Phase Equilibria*, 15(4), August 1994.

[115] Andreas Zerr, Gerhard Miehe, and Ralf Riedel. Synthesis of cubic zirconium and hafnium nitride having Th 3 P 4 structure. *Nature Materials*, 2(3):185–189, March 2003.

[116] Manish Chhowalla and H. Emrah Unalan. Thin films of hard cubic Zr 3 N 4 stabilized by stress. *Nature Materials*, 4(4):317–322, April 2005.

[117] I Khidirov, VT Em, I Karimov, and VE Loryan. The Ordered Phase in the Supersaturated Solution of Nitrogen in alpha-Zirconium. *Phys. Met. Metallogr.(USSR)*, 64(6):174–176, 1987.

[118] R. Juza, A. Gabel, H. Rabenau, and W. Klose. ON A BLUE ZIRCONIUM NITRIDE. *Z. Anorg. Allgem. Chem.*, Vol: 329, May 1964.

[119] L.C. Gontijo, R. Machado, E.J. Miola, L.C. Casteletti, and P.A.P. Nascente. Characterization of plasma-nitrided iron by XRD, SEM and XPS. *Surface and Coatings Technology*, 183(1):10–17, May 2004.

[120] P. Patsalas, N. Kalfagiannis, S. Kassavetis, G. Abadias, D.V. Bellas, Ch. Lekka, and E. Lidorikis. Conductive nitrides: Growth principles, optical and electronic properties, and their perspectives in photonics and plasmonics. *Materials Science and Engineering: R: Reports*, 123:1–55, January 2018.

[121] Hiroshi Naganuma, Ryoichi Nakatani, Yasushi Endo, Yoshio Kawamura, and M. Yamamoto. Magnetic and electrical properties of iron nitride films containing both amorphous matrices and nanocrystalline grains. *Science and Technology of Advanced Materials*, 5(1-2):101–106, January 2004.

[122] Tables of chemicals and etchants. In *Metallography and Microstructures*. ASM International, December 2004.

[123] W. E. Sweeney and A. P. Batt. Electron probe and X-ray diffraction measurements of intermediate phases in Zr diffused with Cr, Fe, Ni, Cu and Mo. *Journal of Nuclear Materials*, 13(1):87–91, January 1964.

[124] U. Gösele and K. N. Tu. "Critical thickness" of amorphous phase formation in binary diffusion couples. *Journal of Applied Physics*, 66(6):2619–2626, September 1989.

[125] A.C. Fischer-Cripps. Critical review of analysis and interpretation of nanoindentation test data. *Surface and Coatings Technology*, 200(14-15):4153–4165, April 2006.

[126] Neelima Khare, Praveen Kumar Limaye, Kulwant Singh, Dhananjay Tatyasaheb Jadhav, Arundhati Bute, and Navnath Kalel. Experimental and Theoretical Analysis of Zircaloy-4 and AISI 304 Stainless Steel Material Pair in Water Sliding Conditions. *Advances in Tribology*, 2018:e7575216, July 2018.

[127] M Ahmad, J. I Akhter, M. A Shaikh, M Akhtar, M Iqbal, and M. A Chaudhry. Hardness and microstructural studies of electron beam welded joints of Zircaloy-4 and stainless steel. *Journal of Nuclear Materials*, 301(2):118–121, March 2002.

[128] Yutaka S. Sato, Yoshito Nagahama, Sergey Mironov, Hiroyuki Kokawa, Seung Hwan C. Park, and Satoshi Hirano. Microstructural studies of friction stir welded Zircaloy-4. *Scripta Materialia*, 67(3):241–244, August 2012.

[129] Devasri Fuloria, Nikhil Kumar, Sunkulp Goel, R. Jayaganthan, S. Jha, and D. Srivastava. Tensile properties and microstructural evolution of Zircaloy-4 processed through rolling at different temperatures. *Materials & Design*, 103:40–51, August 2016.

[130] Devasri Fuloria, Nikhil Kumar, R. Jayaganthan, S. K. Jha, and D. Srivastava. An investigation of effect of annealing at different temperatures on microstructures and bulk textures development in deformed Zircaloy-4. *Materials Characterization*, 129:217–233, July 2017.

[131] M. W. Mallett, Jack Belle, and B. B. Cleland. The Reaction of Nitrogen with, and the Diffusion of Nitrogen in, Beta Zirconium. *Journal of The Electrochemical Society*, 101(1):1, January 1954.

[132] Properties of ZrNx films with x > 1 deposited by reactive radiofrequency magnetron sputtering. *Thin Solid Films*, 515(4):1307–1313, December 2006.

[133] Jianguo Zhang, Ruijiao Jiang, Yangyang Tuo, Taian Yao, and Dongyun Zhang. Elastic Properties and Elastic Anisotropy of ZrN 2 and HfN 2. *Acta Physica Polonica A*, 135:546–552, March 2019.

[134] M. Del Re, R. Gouttebaron, J. P. Dauchot, P. Leclère, G. Terwagne, and M. Hecq. Study of ZrN layers deposited by reactive magnetron sputtering. *Surface and Coatings Technology*, 174–175:240–245, September 2003.

[135] JW Gibbs. The scientific papers of j. Willard gibbs, 1 dover publications. *Inc., New York*, 1961.